Extreme Temperature Regimes during the Cool Season: Their Trends, Variability, Triggers and Physical Connections to Low Frequency Modes

A Dissertation
Presented to
The Academic Faculty

By

Rebecca M. Westby

In Partial Fulfillment
Of the Requirements for the Degree
Doctor of Philosophy in Atmospheric Science

Georgia Institute of Technology

May 2015

Extreme Temperature Regimes during the Cool Season: Their Trends, Variability, Triggers and Physical Connections to Low Frequency Modes

Approved by:

Dr. Robert X. Black, Advisor
School of Earth and Atmospheric Sciences
Georgia Institute of Technology

Dr. James Belanger
School of Earth and Atmospheric Sciences
Georgia Institute of Technology

Dr. Yi Deng
School of Earth and Atmospheric Sciences
Georgia Institute of Technology

Dr. Katherine J. Evans
Oak Ridge National Laboratory

Dr. Emanuele Di Lorenzo
School of Earth and Atmospheric Sciences
Georgia Institute of Technology

Date Approved: Spring 2015

Acknowledgements

I would like to acknowledge and extend my heartfelt gratitude to the following people whose unwavering support has made the completion of this dissertation possible. First of all, I would like to thank my advisor, Dr. Robert Black, for giving me the opportunity to work on this project and for his patient guidance and support throughout the research process. I would also like to thank Dr. Yi Deng for providing valuable commentary and suggestions for various parts of this research. I would also like to thank my committee members Dr. Emanuele Di Lorenzo, Dr. Katherine Evans and Dr. James Belanger for providing insightful and constructive comments on my dissertation.

In addition, many thanks to the members of the Black and Deng research groups, especially my officemates Brad Hegyi, Jia He and Yi Lu for all the great discussions and ever-helpful assistance along the way. I would also like to extend a thank you to all my friends in the EAS department and Atlanta for their camaraderie and encouragement in the pursuit of my degree.

And finally, thank you to my family for all their love, support and encouragement in the pursuit of my education. Most of all, I must thank my husband, Toby Xu, for providing endless encouragement through both the struggles and successes of this process and for taking this journey with me.

TABLE OF CONTENTS

LIST OF TABLES

LIST OF FIGURES

LIST OF ABBREVIATIONS

AO	Arctic Oscillation
CAO	Cold-air Outbreak
DJF	December, January, and February
ENSO	El-Nino Southern Oscillation
ERA	European Centre for Medium-Range Weather Forecasts Reanalysis
ETR	Extreme Temperature Regime
LTPV	Lower-tropospheric potential vorticity
MTPV	Mid-tropospheric potential vorticity
NAM	Northern Annular Mode
NAO	North Atlantic Oscillation
NCEP/NCAR	National Centers for Environmental Prediction/National Center for Atmospheric Research
PBL	Planetary boundary layer
PDO	Pacific Decadal Oscillation
PNA	Pacific-North American pattern
PV	Potential Vorticity
SAT	Surface air temperature
UTPV	Upper-tropospheric potential vorticity
WW	Warm Wave

SUMMARY

During the boreal cool season (December – February) extreme temperature regimes (ETRs), including cold air outbreaks (CAOs) and warm waves (WWs), affect regional economies and human safety via their significant impacts on energy consumption, local agriculture and human health. This work aims to improve our understanding of the trends and variability in ETRs, their physical connections to low frequency modes, and the dynamical mechanisms leading to ETR onset. Earlier studies on ETR trends and variability do not consider the last decade. Further, little is known about the physical and dynamical nature of ETR onset. These unknowns motivate this dissertation and are particularly important for WWs, which have rarely been studied.

This study begins with an updated analysis of the long-term trends and interannual variability in ETRs. Even with the inclusion of the last decade, no significant trends in either WW or CAO occurrence are identified over the continental United States between 1949-2011. The accompanying correlation analysis reveals that on interannual time scales, ETRs in specific regions of the U.S. tend to be modulated by certain low frequency modes. This analysis highlights an important regional asymmetry in the low frequency mode modulation of ETRs, and also indicates that the influence of ENSO upon ATRs is mainly limited to a modest modulation of WWs over the southeast US. Further, a multiple linear regression analysis reveals that the regional collective influence of low-frequency modes accounts for as much as 50% of interannual ETR variability.

A synoptic-dynamic characterization of ETR onset over the southeast US is then performed using composite time-evolution analyses of events occurring between 1949-2011 to provide a qualitative indication of the role of low frequency modes. During CAO

(WW) onset, negative (positive) geopotential height anomalies are observed in the upper troposphere over the Southeast with oppositely-signed anomalies in the lower troposphere over the central US. In most cases, there is a surface east-west height anomaly dipole, with anomalous northerly (CAO) or southerly (WW) flow into the Southeast leading to cold or warm surface air temperature anomalies, respectively. Companion potential vorticity anomaly analyses reveal prominent features in the mid- to upper-troposphere consistent with the geopotential height anomaly patterns. The composite analyses reveal significant roles for both synoptic and large-scale disturbances in ETR development. Synoptic-scale disturbances serve as dynamic triggers for ETR events, while low-frequency modes can provide a favorable environment for ETR onset.

A suite of diagnostic analyses is conducted next and aims to identify the primary thermodynamic processes and dynamical mechanisms responsible for ETR development over the Southeast US. Heat budget analyses implicate linear temperature advection as the primary contributor to ETR development, while nonlinear advection plays a smaller role. Both the linear and the nonlinear terms contribute positively to the temperature tendencies of interest, while the adiabatic and diabatic terms offset some of the advection contributions. Piecewise PV inversion analyses are then conducted to assess which dynamical features directly contribute to the local temperature changes that occur in association with ETRs. A novel result is the discovery of the potential pathway through which the low frequency mode modulation of ETRs takes place. An upper-tropospheric PV feature first induces near-surface temperature advection, which then creates a near-surface temperature anomaly and a corresponding circulation that further enhances the initial temperature advection and ultimately leads to the ETR event.

CHAPTER 1

INTRODUCTION

1.1 General Characteristics of CAOs and WWs

During the boreal cool season, extreme temperature regimes (ETRs), including cold air outbreaks (CAOs) and warm waves (WWs), affect regional economies and human safety over large portions of the United States via their significant impacts on energy consumption, local agriculture, and human health. While ETRs are a type of weather phenomenon most common over eastern North America (Konrad and Colucci 1989) and East Asia (Park et al. 2011), ETRs also occur in other areas of the world including Southern Australia (Ashcroft et al. 2009), the high-latitude South Pacific (Papritz et al. 2015), Mexico and Central America (Schultz et al. 1997, Schultz et al. 1998). Interestingly, this type of phenomena can actually originate outside of the region of impact. For instance, northwestern Canada is a primary genesis location for cold air mass formation (Turner & Gyakum 2011, Zishka and Smith 1980), which can subsequently move into the US, causing a CAO event and providing marked impacts on the United States (Peterson et al. 2013). ETRs are generally defined as events where temperatures are significantly above (WWs) or below (CAOs) average on a synoptic timescale (2-7 days). The extremely cold temperatures associated with CAOs put humans at a higher risk of frostbite and hypothermia, resulting in approximately 30 deaths per year, while economic losses in the agriculture and transportation industries can reach billions of dollars owing to crop damage, livestock death, and transportation delays (Cellitti et al. 2006; Rogers and Rohli 1991). These impacts can be experienced in any

region. However, they are especially pronounced along the East and Gulf Coasts, where the majority of the population is less accustomed to extreme cold temperatures (Cellitti et al. 2006). Historically, cool season WWs have received much less attention than CAOs, but they can have equally significant impacts. Abnormally warm temperatures associated with WWs can cause rapidly melting snow and ice, leading to the ice damming and flooding of rivers, as well as significant monetary losses in the winter sports industry. WWs also pose an increased threat of frost damage to agriculture (Gu et al. 2008) and forest vegetation by inducing premature plant development. However, the resulting changes in forest vegetation also likely have significant biological and ecological impacts (Mori et al. 2014), including changes in soil dynamics, the carbon and nitrogen cycles, wildlife food sources and habitats (Mori et al. 2014, Makoto et al. 2014, Walther et al. 2002, Campell et al. 2005). In response to anthropogenic influences on regional climate, temperature extremes are expected to change in severity, frequency, and duration in the future (Loikith and Broccoli 2012). Because human activities and the environment are greatly vulnerable to and affected by climate and weather extremes (Kharin et al. 2007), there is a strong interest for scientists and society alike to be able to forecast these events.

1.2 Metrics to Measure CAOs and WWs

Heat and cold waves are typically defined as events exceeding a specified *surface* temperature threshold over some minimum number of days (often a synoptic timescale of 2-7 days), and may be statistical (i.e. relative, such as standard deviation) or absolute (Peterson et al. 2013). The use of temperature or temperature anomalies to define events is a common metric of ETR events, and is used in the majority of previous studies on

ETRs. In this study, temperature anomalies are used to calculate a new metric that is an integrative measure of the seasonal impact of ETR events that uniquely combines information regarding both event frequency and amplitude. This is in contrast to the traditional metrics which only measure either event frequency or amplitude. Further, most of the commonly-used metrics are surface-based metrics. However, non-surface based metrics have also been used to identify ETR events, including (stratospheric) mass circulation indices (Yu et al. 2015) and stratospheric circulation anomalies (Kolstad et al. 2010). Although we do not directly assess the role of stratospheric circulations in this analysis, they are implicitly included via our consideration of the NAO and its role in ETRs (specificially CAOs). A more in-depth analysis of the role of stratospheric features is considered beyond the scope of the current study.

1.3 Trends and Variability in ETRs

Even against the general backdrop of globally warming temperatures, past studies find that mid-latitude CAO events can be expected to at least persist (and in some cases increase) in intensity and duration throughout the 21st century based on inferences from historical observed trends (Walsh et al. 2001, Portis et al. 2006, Westby et al. 2013) coupled with modeling studies (Scherer and Diffenbaugh 2014, Kodra et al. 2011, Park et al. 2011). While some studies find that CAO frequency will likely decrease in the future (Kodra et al. 2011), other studies predict that CAOs may even increase in frequency in some regions (Vavrus et al. 2006). These opposing predictions can be linked to regional climate change associated with a forced response in the large-scale circulation or extreme synoptic events (Vavrus et al. 2006, Francis and Vavrus 2012, Loikith and Broccoli

2014). Another perspective is that the mean and variability are distinct statistical moments (Park et al. 2011) that may vary differently in relation to climate change. For example, regional temperature *variability* in a future warmer climate may be similar to that in the present colder climate and hence the behavior of *anomalous* temperature events may not vary appreciably. This also has important potential implications for agriculture in early spring. During early spring, the impacts of CAO events depend more on the variability in temperature than the overall temperature trends. For instance, if plant budding has already occurred in association with the springtime increase in climatological temperatures, or if a WW event induces premature plant development, a subsequent occurrence of freezing temperatures (especially those associated with CAOs) can increase the risk of plant damage. This is especially true in regions where recent climate change includes warmer late winter/early spring air temperatures and advanced plant blooming, which may make the plants more vulnerable if CAOs occur during these developmental stages (Augspurger 2013).

On the other hand, WWs are generally expected to increase in frequency and severity in the future (Scherer and Diffenbaugh 2014). This trend is attributed to an increase in the odds of warm years and seasons due to anthropogenic influences (Christidis and Stott 2014) and globally warming temperatures. But unlike for CAOs, studies of boreal winter WWs are scarce in the literature. Nonetheless, these events can also have important implications for agriculture. Many plants use warming episodes as cues to begin the process of budding, leafing and flowering (Peterson and Abatzoglou 2014), and WWs can pose a threat of increased freeze damage by inducing premature plant development (Gu et al. 2008), followed by a return to normal winter conditions.

Freeze damage can also occur if a late winter WW event is followed by a prominent CAO. Such sequences have been responsible for as much as $0.5-2 billion in damages to the agriculture industry (Peterson and Abatzoglou 2014).

1.4 ETR Connections to Low Frequency Modes

Prior research has shown that ETRs, namely CAOs, are statistically modulated by the large-scale low frequency modes of variability, such as the positive phase of the Pacific-North American (PNA) pattern (Downton and Miller 1993, Vavrus et al. 2006, Cellitti et al. 2006, Rogers and Rohli 1991) and the negative phase of the North Atlantic Oscillation (NAO) (Walsh et al. 2001, Cellitti et al. 2006). In addition, a recent study by Lim and Schubert (2011) found that daily temperature extremes are strongly impacted by the Arctic Oscillation (AO), and this impact is comparable to or stronger than that of the El Nino-Southern Oscillation (ENSO). Unlike CAOs, little is currently known about the nature and low frequency mode modulation of WWs during the boreal cool season. Further, another recent study shows that greenhouse warming leads to a significant increase in the frequency of extreme ENSO (specifically La Nina) events (Cai et al. 2015). Given ENSO's projection onto other low frequency modes such as the PNA, this may have important implications for some categories of extreme weather events in certain regions of the US, which are linked (as will also be shown in this study) to the opposing phases of the PNA.

However, the current understanding of the physical mechanisms behind the observed statistical relationship between ETRs and low frequency modes remains limited (Dole 2008). Previous research on ETR variability and low frequency modes has left

significant gaps in understanding these concepts since the methods used to identify these relationships are purely statistical in nature and hence cannot easily establish the physical connections. Further, several recent studies have suggested that the North American climate has an asymmetric climate response pattern during the opposite phases of ENSO (Wu et al. 2005) and the AO (Wu et al. 2006). However, these studies did not assess how this asymmetry is physically manifested.

Most low frequency modes are quasi-stationary and contribute substantially to low frequency variability over a broad region, frequently producing prolonged anomalies in local and regional weather conditions (Dole 2008). The physical connection between ETRs and low frequency modes is most likely located in the upper troposphere, where there are strong PV gradients near the tropopause that often act as Rossby wave guides (Hoskins et al. 1985). Additionally, Rossby wave propagation is an important source of teleconnectivity in winter (Schubert et al. 2011). Because ETR events often occur at large distances away from the primary centers of low frequency modes, there must be some form of horizontal and vertical communication through the atmosphere. Thus, the responsible dynamical mechanism associated with the low frequency mode could induce an upper level circulation that extends outward in all directions (like the winds associated with a potential vorticity anomaly do) and subsequently form a surface circulation that enacts an ETR event. In fact, the importance of the upper-tropospheric circulation as a precursor to ETRs, particularly CAOs, has recently been emphasized in a study by Park et al. (2008). Additionally, it is likely that other processes work in tandem with low frequency mode processes to produce an ETR since low frequency modes only explain a

portion of the variability in ETRs (Westby et al. 2013). Therefore, low frequency modes may provide a necessary, but insufficient, condition to trigger ETR events.

1.5 ETR Mechanisms

Several studies have examined the cold air outbreak process synoptically via a thermodynamic perspective (e.g. Konrad and Colucci 1989), however, the mechanisms that trigger the outbreak itself by facilitating the latitudinal transport of air masses have not been extensively studied in the literature. There are also very few parallel studies on boreal cool season WWs that exist. As a result, the physical and dynamical mechanisms leading to ETRs remain an important, yet little understood topic.

Several potential mechanisms have been proposed by earlier studies that can produce persistent flow anomalies (Dole 2008, Black and Dole 1993, Evans and Black 2003), which may also contribute to low frequency modes and ETRs: (1) Rossby waves forced by localized diabatic or topographic sources, (2) large-scale flow instabilities, (3) quasi-equilibrium states representing a nonlinear balance between the mean flow and forcing terms, and (4) forcing by anomalous synoptic-scale eddy fluxes. It may be possible that at least one of these mechanisms is responsible for triggering ETRs. In the case of multiple responsible mechanisms, the implicated mechanisms may be important at different stages in the lifecycle of the ETR event. This was found to be the case for several prior studies on other types of persistent flow anomalies (Black and Dole 1993, Evans and Black 2003).

Further, the above mechanisms can be formed either locally or remotely and manifested in two ways. Local mechanisms include nearby development of synoptic-

scale transient features and in situ low frequency anomalies, while remote mechanisms involve energy propagation via Rossby wave trains or propagation of a synoptic-scale transient feature. However, whether the responsible mechanism(s) is local or remote, synoptic-scale WWs that occur must be a result of warm air being advected into an area by the responsible mechanism(s) because it is unlikely that a substantially warm air mass could form over the continent during winter on a synoptic timescale (~2-7 days). On the other hand, the mechanism(s) responsible for CAOs could create the event by either a) moving cold air into a region, or b) by producing the cold air locally.

1.6 Motivation and Research Goals

This dissertation aims to improve our understanding of the trends and variability in ETRs, their physical connections to low frequency modes, as well as the dynamical mechanisms leading to ETR onset. Many of the earlier studies on ETR trends and variability do not consider the last decade, which is known to be a period of rapid warming globally. Further, there is relatively little known about the physical nature of ETR events, including how they are modulated by low frequency modes and what dynamical mechanisms are responsible for ETR development. These unknowns, as well as the significant impacts that ETR events can have on society and the economy, provide the motivation for the following statistical and diagnostic study. This suite of analyses contained within is of particular importance for WWs, as these events have rarely been studied.

Given these motivating factors, the following are the primary goals of the work presented in this dissertation:

1. Provide an updated assessment of the trends and variability in ETRs by including information on the previous decade (2001-2011).
2. Identify the synoptic and dynamic features associated with ETR onset, while emphasizing their link to low frequency modes.
3. Reveal the underlying mechanism(s) that lead to ETRs, while establishing the role of low frequency modes in ETR development.

1.7 Implications of this Research

The results of this dissertation will provide many benefits, both to science as well as society. Each of the objectives (see Section 1.6) will contribute to advancing the scientific knowledge of ETRs. Specifically, the second and third objectives will help explain the physical connection behind the observed statistical relationship between LF modes and ETRs, which currently remains limited. In addition, understanding the relationships between low frequency variability, the mechanisms leading to ETR onset, and how they relate to ETR evolution is fundamental to the problem of advancing extended-range weather predictions (Dole 2008). However, the types of trigger mechanisms will have important implications for ETR predictability and the potential benefits to society. If the mechanisms are linear, then ETRs may be identified prior to large-scale growth and persistence. However, if the mechanisms are non-linear or are small-scale features, then improvements in forecasting might be limited (Dole 2008). However, even small improvements in forecasts would help reduce the negative impacts associated with ETR events. These improved forecasts would be especially helpful for the agricultural and transportation sectors, and will help protect the health and safety of

the public through advanced warnings of these events. Overall, a more complete physical understanding of ETRs is essential for assessing the likely future variability of ETRs in association with climate change. Understanding changes in ETR probability in a future climate is vital for risk management and assessing the agricultural, economic, and ecosystem consequences (Ruff and Neelin 2012). Finally, this research will contribute to an over-arching atmospheric science goal to achieve a more complete understanding of our physical climate system and will add to the on-going conversation among atmospheric scientists about the weather-climate interaction.

1.8 Outline of the Dissertation

This dissertation presents analyses and results that collectively address the three goals outlined in Section 7 of the current chapter. Chapter 2 presents an overview of the datasets used, details how the temperature anomalies used throughout the analysis are calculated, and describes the general statistical methods that are common throughout the dissertation. Chapter 3 then presents the updated investigation on the trends and variability in ETRs, and details some new results on the asymmetric influence of low frequency modes on ETRs. The primary synoptic and dynamic features associated with ETR onset over the Southeast US are detailed in Chapter 4 with particular emphasis on the link to prominent low frequency modes. In Chapter 5, extensive diagnostic analyses are conducted to determine specifically the thermodynamic and dynamic processes and mechanisms influencing the onset of ETRs, which provide confirmation of the role of low frequency modes in ETR development. Chapter 6 then presents a summary of the dissertation, including overall conclusions and ideas for future work.

CHAPTER 2

DATA AND GENERAL METHODOLOGY

This chapter details the datasets used and describes the general statistical methods and calculations that are common throughout the dissertation. More specific details of each individual analysis are included in the data and methods subsections of the subsequent results chapters (Chapters 3-5). Lastly, an introduction to the potential vorticity framework is provided.

2.1 Datasets

The dataset used for the identification of observed ETRs is the reanalysis data from the National Centers for Environmental Prediction–National Center for Atmospheric Research (hereafter NNR) (Kalnay et al. 1996). In Chapter 3, the variable used for ETR identification is the *daily* mean surface air temperature T at the σ=0.995 level, the closest available level to the surface. Meanwhile, in Chapters 4 and 5, the *four-times daily* surface air temperature (SAT) is used. The usage of the four-times daily instantaneous data (versus daily means) in these chapters helps facilitate a better understanding of the detailed synoptic conditions leading to ETRs as smaller-scale features, such as fronts, become more readily apparent. These data have a grid resolution of 2.5° latitude x 2.5° longitude. The NNR data is one of the longest reanalysis datasets currently available, and is advantageous because its length allows for a relatively large sample of events. The subset of data used for this analysis spans from January 1948 to February 2011. Even though this time period (which includes 64 winters) investigated in

our study is only a small subset of the Earth's long history, this period is in fact long enough to investigate recent trends and other characteristics of ETRs. Other NNR fields used in our analysis are: 925 hPa air temperature, 925 hPa vertical velocity (ω), 1000 and 925 hPa zonal and meridional winds, sea level pressure (SLP), the 1000-500 hPa thickness field, and geopotential heights from 1000 to 10 hPa. The vertical levels contained within NNR data are: 1000, 925, 850, 700, 600, 500, 400, 300, 250, 200, 150, 100, 75, 50, 30, 20, and 10 hPa, for a total of 17 vertical levels.

Besides characterizing the synoptic behavior of ETR development, it is of interest to identify significant dynamical features, which can be succinctly described using potential vorticity (PV). Although PV is not readily available on pressure surfaces from NNR, it is easily obtained from the European Centre for Medium-Range Weather Forecasts (ECMWF) Reanalyses (hereafter ERA) (ERA data used in this study have been obtained from the ECMWF data server http://data-portal.ecmwf.int/). Because the calculation for PV involves fine-scale spatial derivatives, we chose to use the ERA data to take advantage of its finer resolution (Dee et al. 2011; Uppala et al. 2005; Kalnay et al. 1996). Therefore, the ERA data likely provides more detailed information on the PV structure even when interpolated to the NNR grid. The ERA dataset is composed of ERA-40 (which spans 1957 to 2001) and ERA-Interim (extending from 1979-present), which have different horizontal spatial resolutions (2.5° latitude x 2.5° longitude and 1.5° latitude x 1.5° longitude, respectively).

To make use of the ERA data for the same time span as NNR, we tested whether it was possible to "merge" these two datasets to create a longer dataset, via spatial interpolation of the ERA-Interim data (Dee et al. 2011) to be comparable with ERA-40

(Uppala et al. 2005). We first verified that the ERA-40 and ERA-Interim datasets similarly represent large-scale variability in the field variables (e.g., SAT and 500 hPa geopotential height) in the region of interest. To achieve this, we conducted spatial correlation analyses between the two datasets for the period of overlap (1980-2002) over a domain encompassing North America (30°N to 70°N, 230°E to 300°E) including the air mass source regions for CAOs and WWs. The ERA-Interim data was interpolated to the ERA-40 grid using bilinear interpolation. The spatial correlation values for SAT and 500 hPa geopotential heights, performed at daily, monthly and yearly time scales, were all at or above 0.999, suggesting excellent quantitative correspondence. Therefore, we ascertain that the ERA-40 and ERA-Interim datasets ***can*** be usefully merged into one dataset (denoted ERA) to provide a supplementary long-term dataset to NNR. We then create a PV dataset that extends from September 1957 to February 2011 with a grid resolution of 2.5° latitude x 2.5° longitude. We analyzed PV at 12 levels ranging from 925 hPa up to 100 hPa.

The low-frequency modes of interest are the North Atlantic Oscillation (NAO), Pacific-North American pattern (PNA), the Pacific decadal oscillation (PDO), and the El Nino – Southern Oscillation (ENSO) (defined in terms of the Nino 3.4 sea surface temperatures), which have inherent time scales of a month or longer and are known or suspected to be associated with ETRs. The winter (DJF) mean low-frequency mode indices used in our investigation are from the National Oceanic and Atmospheric Administration (NOAA) Climate Prediction Center (CPC) (http://www.esrl.noaa.gov/psd/data/climateindices/). An active debate in the literature remains as to whether the AO or NAO is more appropriate for such analyses (e.g. Hurrell

et al. 2003, Deser 2000, Wallace 2000, and Ambaum et al. 2001). However, the surface circulations of each mode are nearly identical over the region of interest, and our separate analysis of both modes produced quantitatively similar results. Thus, for brevity we choose to represent only the results for the NAO in Chapter 3. Further, in Chapters 4 and 5, the emphasis shifts to the North Atlantic Oscillation (NAO) and the Pacific-North American (PNA) teleconnection patterns, which are recognized as leading factors in SE ETR modulation (e.g. Westby et al. 2013, among others).

2.2 Temperature Anomaly Calculations

There are two primary methods typically used to define temperature events: 1) temperature anomalies or 2) absolute temperatures. We choose to define events in terms of temperature anomalies since we are most interested in examining events that are deviations from normal (seasonal) conditions (and ultimately represent intraseasonal temperature variations). The temperature anomalies are calculated relative to the daily mean seasonal temperature cycle. As such, this method implicitly assumes that the background seasonal temperature cycle is stationary (i.e. not changing over periods of decades). However, this may or may not be true, and can have significant impacts on our results and their interpretation if not considered carefully. If the dataset considered includes a long-term basic state temperature trend, such as the warming hole observed over the eastern US (e.g. Meehl et al. 2012), the results may indicate a trend in ETR frequency and amplitude even if there was no concomitant long-term trend in intraseasonal temperature variability.

To determine the degree of statistical stationarity, further testing is required. Statistical stationarity in the dataset is assessed in terms of long-term trends in the annual winter-mean [December–February (DJF)] temperature. Since statistically significant trends in the long-term annual winter-mean temperatures are identified (Chapter 3), the dataset is therefore not statistically stationary, and the temperature records are first detrended by explicitly removing the long-term trend in annual winter mean temperature for each grid point considered. The dataset detrending ensures that any observed trends in ETRs are not artificial due to changes in the background mean temperature. The detrended dataset is used in all subsequent calculations. Thus, the decision to detrend the data is intrinsically linked to the desired intention of characterizing anomalous behavior of ETRs and the negative implications of *not* detrending on the results. Further, since a major focus of this study is the examination of the association between atmospheric circulation patterns and ETRs, it is appropriate to consider detrended data.

Many previous cold air outbreak studies apply a local temperature criterion to identify events, and for consistency, a similar approach is applied in this study. Extreme temperature regimes are identified in Chapter 3 for the continental United States *at each grid point* in terms of the daily mean surface air temperature anomalies (T'). For each grid point, the daily mean T climatology is first calculated and then the annual cycle of the daily climatology is smoothed (to remove residual high-frequency variability) by retaining the first six Fourier harmonics of the annual cycle (Figure 2.1). An analogous procedure is performed to obtain a smoothed annual climatological cycle of daily mean standard deviation σ (Figure 2.2). Daily temperature anomalies are then obtained by subtracting the smoothed daily mean T climatology value from the daily mean T at each

grid point. Finally, the anomalies are normalized by the smoothed daily mean standard deviation. The normalized temperature anomaly calculation is mathematically represented by:

$$T' = \frac{(T - \bar{T})}{\sigma} \qquad (2.1)$$

where $\bar{T}$ (σ) is the Fourier-smoothed daily winter-mean temperature (standard deviation).

In Chapters 4 and 5, to identify ETR events during winter (December-February), we first calculate *detrended* surface air temperature anomalies from NNR following the approach described above. However, in that suite of analyses this method is applied to four-times daily SAT averaged over a specific region instead of at individual grid points. The region of interest for this study is the Southeast (SE) US, as defined in Fig. 6 in Chapter 3, since ETRs in this region exhibit the strongest connection to low frequency modes.

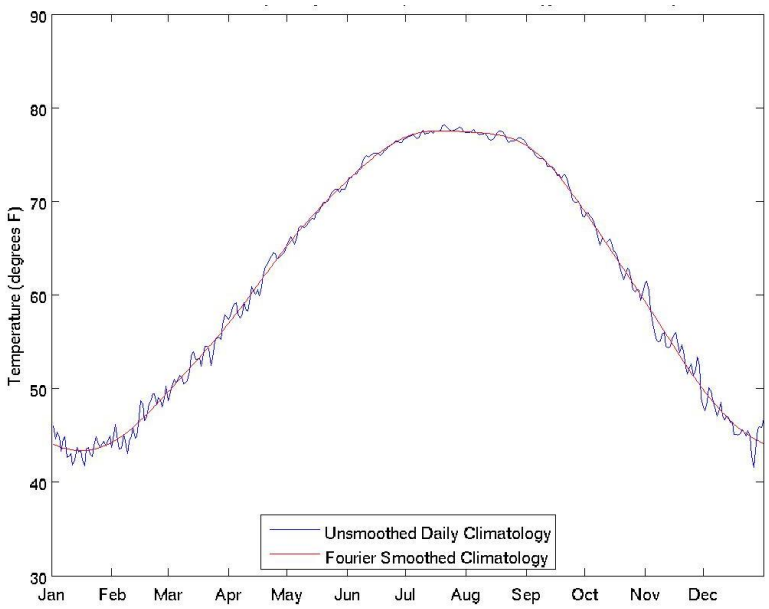

Figure 2.1: Comparison between the unsmoothed (blue) and Fourier smoothed (red) NNR climatology of the average daily mean temperatures for a grid point in the Southeast U.S.

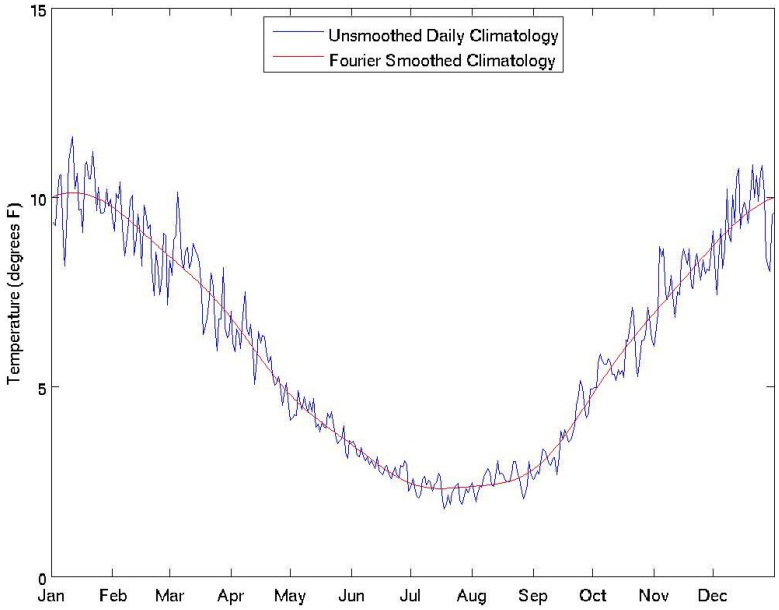

Figure 2.2: Comparison between the unsmoothed (blue) and Fourier smoothed (red) NNR climatology of the average daily mean temperature standard deviation for a grid point in the Southeast U.S.

2.3 Statistical Methods

2.3.1. Statistical Significance

Several of the accompanying analyses contain an assessment of statistical significance. In Chapter 3, all trends and correlations are accompanied with a p-value for occurrence by chance, which is calculated using a two-tailed Student's-t test. Trends are considered significant when the p-value is less than 0.05. The effect of autocorrelation in the time series, which could induce artificially high statistical significance due to memory in the atmosphere, was accounted for by computing the effective degrees of freedom using the procedure of Wilks (2006). Estimating the effective degrees of freedom (or sample size) is easily done when the underlying data follows a first-order autoregressive process. Daily meteorological values (such as daily temperature as is used in the Chapter 3 analyses) can generally be thought of as first-order autoregressive processes (Wilks

2006). The persistence in a first-order autoregressive process can be characterized by the lag-1 autocorrelation coefficient of the data series. The effective sample size is then calculated using equation (2.2):

$$n' \cong n\frac{(1-\rho_1)}{(1+\rho_1)} \qquad (2.2)$$

where n' is the effective sample size, n is the total number of samples, and ρ_1 is the lag-1 autocorrelation coefficient. If the autocorrelation is 0 at lag-1, then n'= n. As the autocorrelation increases, the effective degrees of freedom decrease. Therefore, by adjusting the degrees of freedom to the effective degrees of freedom, the statistical significance is more accurately assessed.

Statistical significance is also assessed in the composite analyses provided in Chapter 4. However, it is not necessary to apply the Wilks method because the data that comprises those composites can be considered independent discrete events. When the data is independent, the autocorrelation is 0 at lag-1 and n'= n.

2.3.2. Composite Analyses

Compositing, or superposed epoch analysis, is an analysis technique that consists of sorting data into categories and then averaging the data. Given a sufficient amount of data, the common underlying signal should emerge in the average (composite) field while the noise cancels out. As such, composite analysis is a relatively simple and effective method for identifying the specific synoptic-scale circulation patterns that are associated with extreme weather events (Chen and Zhai 2014) and have been used in several prior studies on a variety of extreme weather events (Chen and Zhai 2014, Sisson and Gyakum 2004, Grotjahn and Faure 2008, Milrad et al. 2009). Local maxima and minima in the

composite anomaly fields indicate either (1) the presence of a stronger feature in many of the events or (2) that a given feature is more consistently located in a given location (Konrad 1996). Thus, composite analyses help to identify features that are *common* among individual events, which can ultimately be used as an analog for forecasting such events. Composite analyses are used extensively in Chapters 4 and 5. In Chapter 4, composite fields of several atmospheric variables including winds, geopotential height and potential vorticity are created to help identify the synoptic and dynamic circulation features associated with ETR development. In Chapter 5, composite fields of 925 hPa air temperature and winds (horizontal and vertical) are calculated over the ETR onset period and used in the heat budget calculations to quantify the thermodynamic processes that occur during ETR onset. In addition, composite geopotential height anomalies over the ETR onset period are used as inputs to the piecewise PV inversions to help identify which dynamical features are responsible for the observed near-surface circulation during ETR onset.

2.4 The Potential Vorticity Framework

Potential vorticity (PV) is a dynamical quantity that derives its name from the fact that there is potential to create vorticity by changing either latitude or the thermal stratification. It is a very powerful yet succinct way to view the dynamics of the atmosphere (Hoskins et al. 1985) and can be used to diagnose the importance of various physical processes in the atmosphere. The PV framework will be adopted here because PV conservation and the invertibility principle enable a complete description of the flow evolution based solely on the 3-D PV distribution (Black and Dole, 1993).

Local anomalies of PV are features of interest because they are associated with identifiable and discrete circulations. They can occur at a variety of levels, including at the surface. The circulation around a positive (negative) PV anomaly is cyclonic (anticyclonic) flow. Further, PV anomalies are characterized by vorticity and static stability anomalies of the same sign.

One particularly useful type of PV is quasi-geostrophic potential vorticity (QGPV). The quasi-geostrophic potential vorticity is defined by:

$$q = \left[\frac{1}{f_0}\nabla^2\Phi + f + \frac{\partial}{\partial p}\left(\frac{f_0}{\sigma}\frac{\partial\Phi}{\partial p}\right)\right] \qquad (2.3)$$

where $f = f_o + \beta\Delta y$ is the Coriolis parameter on a β plane, σ is the static stability parameter, and Φ is the geopotential. The individual terms in q are (from left to right) are the geostrophic relative vorticity, the planetary vorticity, and the stretching vorticity. Although the equation (2.3) above is scaled for a β plane for simplicity of discussion, the results in this dissertation were compiled using q expressed in spherical coordinates. However, the coordinate system does not fundamentally change the equation nor its invertibility. The quantity q is approximately conserved following adiabatic and inviscid geostrophic motion. Thus:

$$\frac{dq}{dt_g} = 0 \qquad (2.4)$$

A particular benefit of QGPV is that it is linear (unlike Ertel's PV) and is valid for large-scale atmospheric motions (both of which are discussed further in Chapter 5). In addition, since Φ is related to q by a second-order differential operator, the geopotential disturbance associated with a localized anomaly in q will extend horizontally and vertically beyond the region of anomalous q. This implies that upper level disturbances

may induce a circulation in the lower troposphere. The vertical extent of the circulatory influence of a PV anomaly is known as the penetration depth, and is given by:

$$H = \frac{fL}{N} \qquad (2.5)$$

where L is the length scale of the anomaly, f is the Coriolis parameter, and N is the Brunt-Vaisala frequency. Thus, the penetration depth of a given PV anomaly varies as the scale (i.e. magnitude) of the anomaly and inversely to the static stability (represented by N). The magnitude of the anomaly is maximized at the level of the anomaly.

Potential vorticity is a very useful and powerful tool for understanding atmospheric dynamics, stemming from its conservative properties and the invertibility principle. The invertibility principle states that if the global distribution of PV is known, and the proper balance condition and boundary conditions are assumed, it is possible to invert the PV field to determine the corresponding values of geopotential height and subsequently the winds, temperature and static stability within the domain. (Hoskins et al. 1985). Thus, one of the primary utilities of QGPV is that it can be inverted to deduce the associated flow field. This process of recovering the flow field from the potential vorticity field is referred to as PV inversion.

If a reference state is defined such that $q' = q - q_{ref}$ and a vertically averaged static stability is assumed, then (2.3) can be rewritten as:

$$\mathcal{L}(\Phi') = q' \qquad (2.6a)$$

or equivalently,

$$\Phi' = \mathcal{L}^{-1}(q') \quad (2.6b)$$

where

$$\mathcal{L} = \frac{1}{f_0}\nabla^2 + \frac{\partial}{\partial p}\left(\frac{f_0}{\sigma}\frac{\partial}{\partial p}\right) \qquad (2.7)$$

and is a linear operator linking the q and Φ fields. The inversion of this operator is accomplished through an iterative process. Because of the linear nature of this operator, when the entire PV field is inverted the resulting geopotential field will almost exactly match the observed geopotential field.

If instead q is written in the form

$$q' = \sum_{i=1}^{n} q_i' \quad (2.8)$$

then it can be seen that the PV field can be subdivided into as many "pieces" (layers, regions, individual anomalies, etc) as desired. Then, equations (2.6a) and (2.6b) can instead be written as:

$$\mathcal{L}(\Phi_i') = q_i' \quad (2.9a)$$

or equivalently,

$$\Phi_i' = \mathcal{L}^{-1}(q_i') \quad (2.9b)$$

According to (2.9a,b), the circulation field associated with a specific "piece" of the PV field can be isolated and inverted separately from the other features in the PV field and its unique contribution to the circulation field can be identified. Hence, this invertibility, along with the linearity of q, allows for portions of the PV field to be inverted with the appropriate boundary conditions. This process is known as *piecewise PV inversion* (Davis 1992). In this dissertation, the piecewise PV inversion process is basically a two step process in which geopotential height anomalies are used to calculate the PV anomalies, after which the PV anomalies of interest are isolated and inverted to obtain the circulation induced solely by the isolated PV anomalies. Piecewise PV inversions are used

extensively in Chapter 5 as a diagnostic tool to identify whether and how much key PV anomaly features play a role in enacting ETR events.

However, in order to apply the invertibility principle fully by considering the "true" PV field, near-surface potential temperature anomalies must also be considered as part of the near-surface PV field (Hoskins et al. 1985). Bretherton (1966) was the first to identify that surface potential temperature anomalies are functionally equivalent to potential vorticity anomalies. As further proof of this concept, Hoskins et al. (1985) demonstrates that in an idealized model situation where surface potential temperature (theta) anomalies are present, the magnitudes of the induced wind and pressure fields are very significant. Specifically, they found that a warm (cold) surface potential temperature anomaly induces a cyclonic (anticyclonic) circulation at the surface. Thus, it is clear that a fundamental part of the PV anomaly distribution is the distribution of potential temperature anomalies (i.e., "surface theta") at the lower boundary, which act as *effective* PV anomalies. Thus, warm (cold) surface theta anomalies correspond to an effective positive (negative) PV anomaly. In the real atmosphere, surface theta can be interpreted as either theta or temperature (T) on some isobaric level near the surface (Hoskins et al. 1985). For the purposes of this dissertation, the surface is taken to be 962.5 hPa (halfway between the lowermost two levels of the atmosphere). Therefore, in the subsequent analyses, the surface theta anomaly field is considered as part of the PV anomaly field.

CHAPTER 3

TRENDS AND VARIABILITY

The work presented in this chapter is published in the Journal of Climate (Westby et al. 2013).

3.1 Background & Motivation

Previous research on CAO variability found no evidence of a trend toward fewer extreme cold events in the United States (Walsh et al. 2001; Portis et al. 2006). However, these studies do not include information encompassing the last decade. Therefore, extending these studies to examine recent trends in CAO variability is one of the goals of this study. Furthermore, this analysis also includes a new additional focus on the trends in WWs during the boreal cool season, which have rarely been considered in previous studies. Interestingly, a recent study by Hankes and Walsh (2011) found warming trends within high-latitude cold air mass formation regions. However, considered alongside a lack of change in CAO frequency, this local warming trend presents an intriguing paradox. Two recent winters provide prime examples of this paradox, as both winters were exceptionally cold within particular regions (Cohen et al. 2010, Guirguis et al. 2011, Wang et al. 2010) despite a background consisting of anomalously warm hemispheric-average winter temperatures (Cohen et al. 2010). This suggests, then, that there must be some mechanism or process in the atmosphere with a stronger impact on the interannual variability and trends in CAOs other than a simple consideration of the mean background temperature. One such mechanism could be related to interannual variations in the large-scale circulation pattern.

Prior research has shown that ETRs—namely, CAOs—are sometimes related to the large-scale low-frequency modes of variability, such as the positive phase of the Pacific–North American (PNA) pattern (Downton and Miller 1993; Vavrus et al. 2006; Cellitti et al. 2006; Rogers and Rohli 1991) and the negative phase of the North Atlantic Oscillation (NAO) (Walsh et al. 2001; Cellitti et al. 2006). In addition, a recent study by Lim and Schubert (2011) found that daily temperature extremes are strongly linked to the Arctic Oscillation (AO), and this impact is comparable to or stronger than that of the El Niño–Southern Oscillation (ENSO). Unlike CAOs, little is currently known about the nature and low-frequency mode modulation of WWs during the boreal cool season, and this topic is therefore another focus of this study. In addition, this study will quantify the respective roles of these modes of low-frequency variability in accounting for seasonal ETR behavior, which has also not been fully explored previously.

.

3.2 Data & Methods

To characterize the behavior of ETRs, an impact factor metric is devised that quantifies the cumulative effect of all warm or cold days per winter season. Each winter season is December–February and is denoted by the year in which January and February fall, and the impact factor metric is calculated by summing the absolute values of the normalized T' values for all days during the winter season that exceed a threshold of +n (a WW event) or −n(a CAO event). For our study, n is chosen to be 1 and represents events that are at least one standard deviation above/below average. The equation for the impact factor can be written as:

$$Impact\ Factor = \sum_{i=1}^{N} \left| \frac{(T - \bar{T})_i}{\sigma_i} \right| \quad (3.1)$$

where $(T - \bar{T})$ is the local temperature anomaly, σ is the local standard deviation in temperature and N is the number of days each winter above (or below) the selected threshold. Thus, the impact factor represents an integrative measure of the seasonal impact of ETR events and combines information regarding both event frequency and intensity. The choice of n=1 relates to this study's overarching philosophy to study extreme events that provide a substantial integrated impact on local society. By selecting a one sigma threshold, we are able to sample a range of extreme events, including events at the lower end of the anomaly spectrum (±1σ) as well as those at the higher end of the spectrum (±2σ). This allows for the inclusion of both lower amplitude events that can have strong cumulative impacts, especially if they are long-lived, as well as short-lived, high amplitude events. Further, one standard deviation during the winter months, particularly over the eastern half of the US, is typically at least 6 degrees C, so including events at a threshold level of ±1σ includes events of substantial anomaly amplitude. A second, more practical reason for choosing this threshold is related to statistical samplings for the purposes of identifying trends and connections to low frequency modes. By employing a slightly more modest threshold, we are able to obtain a large enough statistical sample to perform meaningful statistical significance tests. Nonetheless, we suggest that the results obtained using the lower threshold provide at least a qualitative indication of the behavior of higher amplitude events. To support this conjecture, in Figure 3.1 we plot parallel analyses of interannual variability for both one sigma and 1.5 sigma anomaly thresholds at one grid point near Atlanta, GA. We suggest that this figure indicates that interannual variability in ETR behavior is not appreciably

impacted by threshold level. In keeping with our philosophical motivation and to ensure statistically reliable results, here we choose to retain our one sigma threshold criterion.

The long-term trends in ETRs are studied by correlating the time series of each ETR metric with time from 1949 to 2011. All trends are considered using a p value for occurrence by chance, which is calculated using a two-tailed Student's t test. Trends are considered significant when p is less than 0.05. The effect of autocorrelation in the time series is accounted for by computing the effective degrees of freedom using the procedure of Wilks (2011).

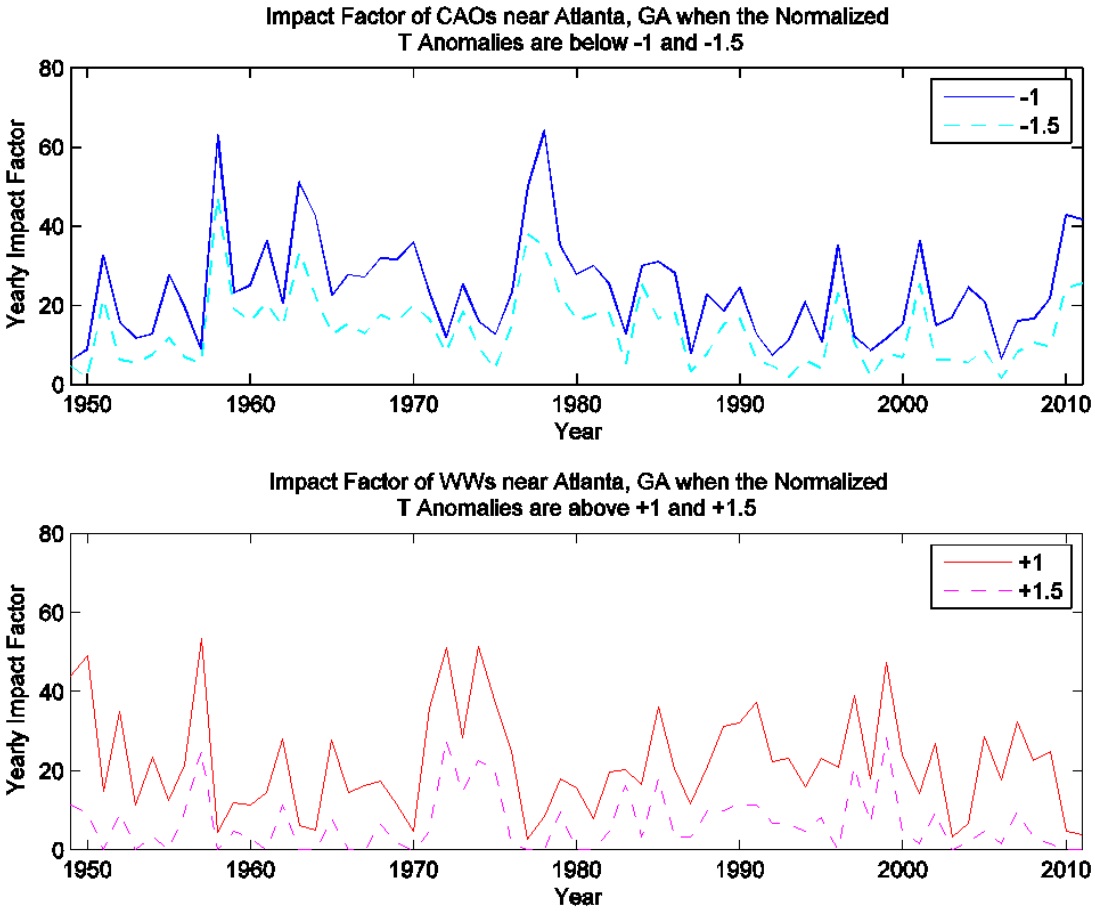

Figure 3.1: The Impact Factor of CAOs (WWs) at a Grid Point near Atlanta, GA when the Normalized T Anomalies are below (above) -1σ (+1σ) and -1.5σ (+1.5σ), Detrended Data, 1949-2011.

The modulation of ETRs by low-frequency modes is explored via correlation analysis between the seasonal mean ETR metric and the seasonal-mean indices of the low-frequency modes of interest. This analysis is performed for 1950–2011, due to the restricted availability of the observed low-frequency mode indices. The statistical significance of these correlations is tested using the method described above.

A multiple linear regression analysis is then performed using the indices of the significant low frequency modes as predictor variables to quantify the simultaneous influences of multiple low-frequency modes on ETR variability. In performing these regressions, there are two essential characteristics that need to be considered: (i) potential multicollinearities among predictors and (ii) autocorrelation in the residual term. Multicollinearities are situations in which two predictor variables in a multiple linear regression analysis are highly correlated with one another. Testing for multicollinearity is important because it is not always known a priori whether one predictor contains redundant information in relation to another predictor. Multicollinearities among predictors are explicitly detected using the Belsley–Kuh–Welsch (BKW) variance decomposition method (Belsley et al. 1980). In the case that multicollinearities were detected, only one of the implicated predictors was used in the regression. For example, if both the PNA and PDO had statistically significant correlations with an ETR metric and were found to be multicollinear, then only one of them (either the PDO or the PNA) was used as a predictor in the MLR analysis for that particular metric. Testing for autocorrelation in the residuals is equally important because this characteristic acts to degrade the regression and its associated statistics. Autocorrelation in the residuals of the regressions is tested via the Durbin–Watson (DW) statistic (Wilks 2011). In cases where

a positive result is obtained, the multiple linear regressions were reperformed using the Cochrane–Orcutt (CO) method (Cochrane and Orcutt 1949). Finally, the net variance explained by the multiple linear regression is assessed, representing that part of the interannual ETR variability accounted for by the given set of predictor variables.

After the ETR metrics are assessed at each grid point in the domain considered, they are also areally averaged over three regions in the eastern United States and then analyzed in the same manner as described above. We discuss how these regions were chosen in a later section.

3.3 Results & Discussion

3.3.1. Long-term variability

Before examining the interannual variability and trends of extreme temperature regimes, it is insightful to begin by addressing the question of statistical stationarity in the temperature dataset itself. Figure 3.2 shows the long-term trend in winter-mean temperature from 1949 to 2011. There are cooling trends across the Southeast, central United States and the West Coast, while there are warming trends over the upper Midwest and over the Rocky Mountains. Over much of the United States, the observed trends in winter mean temperature are small, and are statistically significant in only a few areas: along the Gulf Coast, over the upper Midwest, and over the Rocky Mountains. Thus, there is a regional structure of the trends in the DJF-mean winter temperatures. In addition, these statistically significant trends reach maximum values near $\pm 0.04 K yr^{-1}$. This finding is qualitatively similar to several previous studies (Lu et al. 2005; Cohen et al. 2012a,b; Wang et al. 2009). The regional minimum in temperature trends across the

central United States and Southeast seems counterintuitive in the context of an overall warming global climate, but several studies have attributed this local cooling to feedbacks in the hydrological cycle (Wang et al. 2009; Pan et al. 2004; Portmann et al. 2009). To ensure that such trends in background winter-mean temperature do not influence our analysis of ETR trends, the background trends are explicitly removed from the temperature dataset prior to performing the remaining calculations.

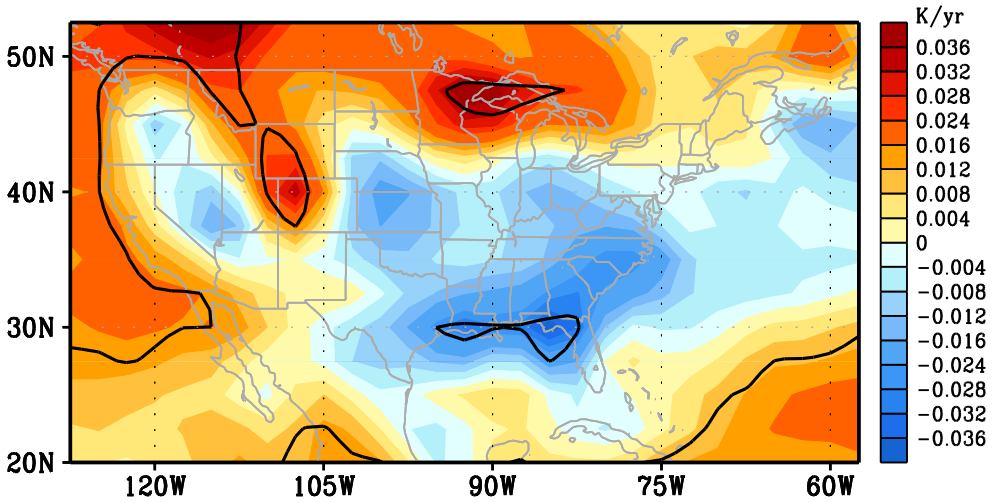

Figure 3.2: DJF seasonal-mean temperature trend values (shaded, K/year), 1949-2011. The black closed contours indicate statistical significance at the 95% confidence level.

It is also useful to examine the long-term seasonal average impact factor for cold air outbreaks and warm waves over the United States to provide a sense of where ETRs are most prevalent and to identify the spatial coherence of ETR behavior. Figure 3.3 shows the long term seasonal average impact factor for CAOs and WWs. It is evident that CAOs tend to have the greatest impact between the Rocky Mountains and the Midwest and along the Gulf Coast, while WWs tend to strongly impact the upper Midwest and Southeast. WWs also appear to less severely impact the Pacific Northwest and Gulf Coast in comparison to CAOs. In addition, WWs appear to occur in distinct regions, while

CAOs tend to occur more uniformly across the U.S. This implies that WWs tend to be more localized events, while CAOs tend to be more geographically expansive events. Accordingly, there are likely different mechanisms responsible for WWs and CAOs.

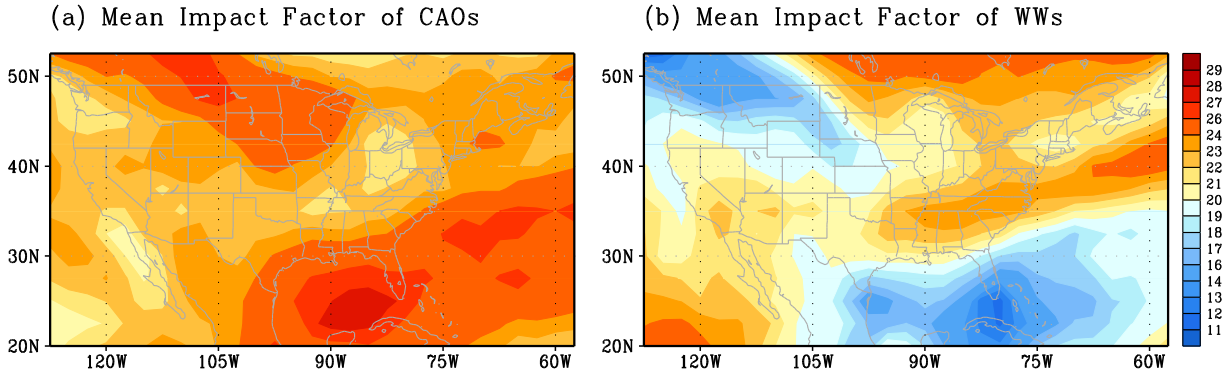

Figure 3.3: DJF seasonal-mean impact factor of days the detrended T' was (a) below -1σ (CAOs) and (b) above +1 σ (WWs), 1949-2011.

The trend analysis reveals that the trends in the impact factor from 1949 to 2011 are very small and insignificant across the continental United States (Figure 3.4). The only statistically significant trend found is a decrease in WWs over a small portion of the Pacific Northwest. Thus, these results indicate that there have not been any significant changes in the seasonal-mean behavior of boreal cool season ETRs over most of the United States between 1949 and 2011. For comparison, this analysis was repeated using nondetrended data (not shown). In this case, the patterns in the trends of ETRs, especially WWs, are collocated with the patterns describing trends in the long-term winter-mean temperatures (Fig. 3.2). Therefore, we find that the trends in ETRs identified using the nondetrended data are an artifact of trends in the background seasonal-mean temperature and is not related to changes in intraseasonal variability. Thus, in order for our analysis to

correctly describe variability in the behavior of temperature anomalies, it is deemed necessary to first detrend the temperature in our analysis. In summary, these results indicate that there have *not* been any significant changes in boreal cool season ETRs over most of the United States from 1949-2011.

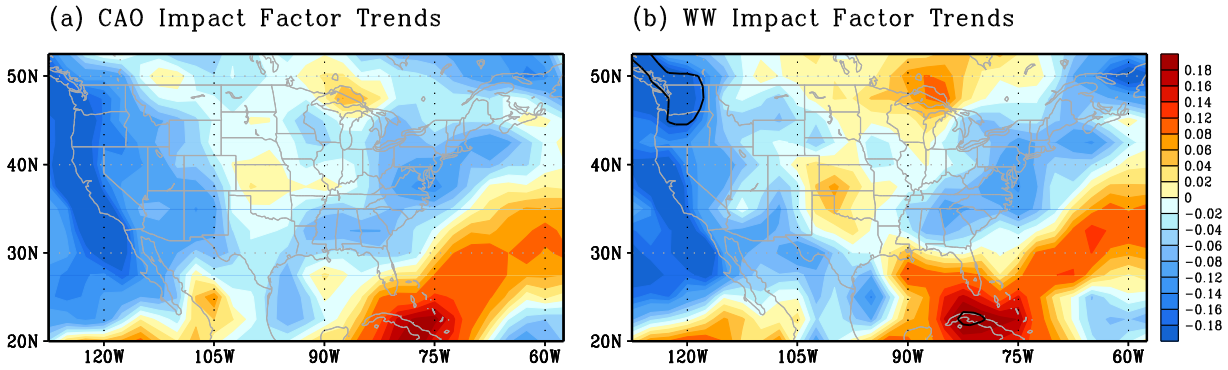

Figure 3.4: Trends (shaded) in the yearly impact factor for (a) CAOs and (b) WWs using detrended data, 1949-2011. The black closed contours indicate statistical significance at the 95% confidence level.

Our results extend and validate the findings of Walsh et al. (2001) and Portis et al. (2006), who found that there has been no decrease in boreal cool season CAO events over a shorter data record. However, one important distinction is that these prior studies did not detrend their data. It is likely that the background temperature trends were less of an issue in these earlier studies owing to the earlier time period analyzed. For instance, several recent studies (Wang et al. 2009, Pan et al. 2004, and Portmann et al. 2009, Cohen et al. 2012b) have emphasized the presence of the "warming hole" in the Southeast U.S. In particular, the Cohen et al. 2012b study examines DJF trends from 1988-2010 (their Figure 3), and finds strong cooling trends over the Southeast US, which encompasses the last decade and is not included in any of the prior studies on CAOs.

Therefore, these studies provide further evidence that the background mean temperatures of the US are in fact changing in a significant manner, and must be taken into account in studies that include the most recent decade and use the background mean temperatures as a benchmark for identifying temperature anomaly events. Nonetheless, our results are consistent with these prior studies on CAO variability.

While our results confirm earlier studies on CAO variability during the latter part of the 20th century (Walsh et al. 2001, Portis et al. 2006), they also present an interesting paradox given that a recent study by Hankes and Walsh (2011) found that the number of extreme cold air mass events in the subarctic of North America, a source region for the cold air masses responsible for CAOs in the continental United States, has dramatically decreased over a similar time period. It seems plausible, then, that these changes (i.e. the warming of arctic air masses) should also be reflected to some extent in the regions to the south that are affected by CAOs originating from these higher latitudes. Paradoxically, however, our current results suggest that changes in extreme cold air masses in the subarctic have not translated into a concomitant change in CAO frequency or amplitude over the continental United States (also see Walsh et al. 2001; Portis et al. 2006). These findings are consistent with recent CAO behavior [namely, during the winters of 2009/2010 and 2010/2011, which were characterized by prominent regional CAOs (Guirguis et al. 2011)] even within a background of anomalously warm hemispheric-average winter temperatures (Cohen et al. 2010). This indicates that interannual ETR variability is controlled by factors besides changes in the mean background temperature.

It is also interesting to consider the trends in ETRs on a regional basis. After the ETR metrics are assessed at each grid point in the domain considered, they are also

areally averaged over three distinct regions in the United States: the Southeast (SE), Midwest (MW), and the Northeast (NE) (Figure 3.5). These three regions were chosen to include several highly populated metropolitan cities, where the influence of CAOs and WWs is often the largest, while also minimizing the direct moderating effect on surface temperatures over the oceans. Hence, by not including the ocean and coastal areas, the impact of CAOs and WWs over the land surface is more effectively isolated. Our focus on the eastern half of the United States is largely based on the high societal impact of ETRs in this region (as described in Chapter 1 and shown in Figure 3.3), as well as the strong correlations between the ETR metrics and low-frequency modes observed in these regions (which will be discussed in section 3.3.2 and shown in Figure 3.6), especially for WWs. Further, there are ongoing research efforts focusing on temperature extremes over California and the western United States (e.g. Grotjahn and Faure 2008). Thus, we decided to focus our attention primarily on the eastern United States.

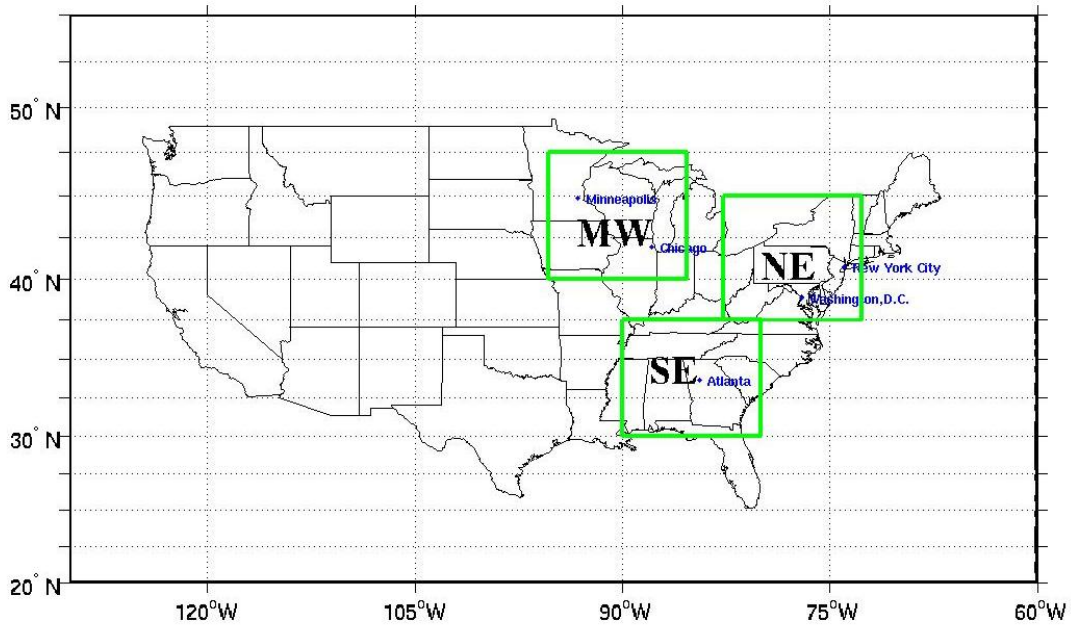

Figure 3.5: The three regions in the United States for which extreme temperature regimes (ETRs) were identified and analyzed.

The trends in ETRs on a regional basis are presented in Table 3.1. The trends for the full duration of the dataset (1948-2011) are provided, as well as a subset that was used for comparisons with CMIP5 data in an observational and model comparison study (Westby et al. 2013) on ETRs trends and variability. In the observations, there are some slight differences between the trend values for WWs between the full and shortened datasets for the SE and NE regions. More specifically, the observed trend for WWs in these two regions for 1949-2011 is slightly negative, while that for 1951-2005 is weakly positive. This discrepancy is not considered to be of great concern, however, because neither trend is found to be statistically significant. In fact, none of the trends in the observed dataset are statistically significant over either the shortened or full time period. Thus, the regional trends are consistent with the grid-point analyses and represent a general lack of significant ETR trends over the latter portion of the twentieth century.

Table 3.1: Linear trends (per year) in the yearly impact factor of cold days below −1σ and warm days above +1σ in the Southeast (SE), Northeast (NE), and Midwest (MW) regions, for DJF. All trends are *not* statistically significant.

		SE		NE		MW	
Observation	Years	CAOs	WWs	CAOs	WWs	CAOs	WWs
NNR- Full	1949-2011	−0.052	−0.040	−0.074	−0.070	−0.015	0.012
NNR - Short	1951-2005	−0.144	0.078	−0.078	0.012	−0.029	0.065

3.3.2. Modulation of ETRs by low frequency modes

We next present the results of our assessment of the relationship between seasonal-mean ETR behavior and various low-frequency modes. Figure 3.6 presents a local correlation analysis that reveals several spatially coherent and statistically significant associations between ETRs and prominent low-frequency modes, indicating that part of the interannual variability in ETRs is linked to these low-frequency modes. More specifically, ETRs within specific regions of the United States are preferentially modulated by subsets of the low-frequency modes considered. For instance, in the southeastern United States, CAOs are more likely to occur when the NAO is in its negative phase (Fig. 3.6, top left panel), which is consistent with the findings of prior studies (e.g., Walsh et al. 2001; Cellitti et al. 2006), while CAOs are more likely to occur over portions of the western United States during the negative phases of the PNA, PDO, and ENSO (Fig. 3.6, left). On the other hand, more WWs over the eastern United States are favored when the NAO (PNA, PDO, and ENSO) is in its positive (negative) phase (Fig. 3.6, right). However, the statistically significant relationship between WWs and the PNA, PDO, and ENSO is restricted in its northward extent compared to that for the NAO.

In addition, it is also clear in Figure 3.6 that the PNA, PDO and ENSO correlation patterns are very similar, and likely contain some redundant information due to correlations among the low frequency modes themselves. Thus, it is evident that ETR connections to climate modes are neither unique nor independent. Specifically, the regional influence of the PNA pattern on ETRs resembles that of both the PDO and ENSO. Because the midlatitude atmospheric patterns for both ENSO and the PDO have projections upon the PNA, this is not a surprising result. By itself, this information is not an issue. However, this similarity becomes of primary concern in pursuing analyses that use these variables as predictors, such as multiple linear regressions. This type of analysis is used in the subsequent section (c), and a discussion on how to account for this cross-information within such analyses is discussed at length in section 3.2.

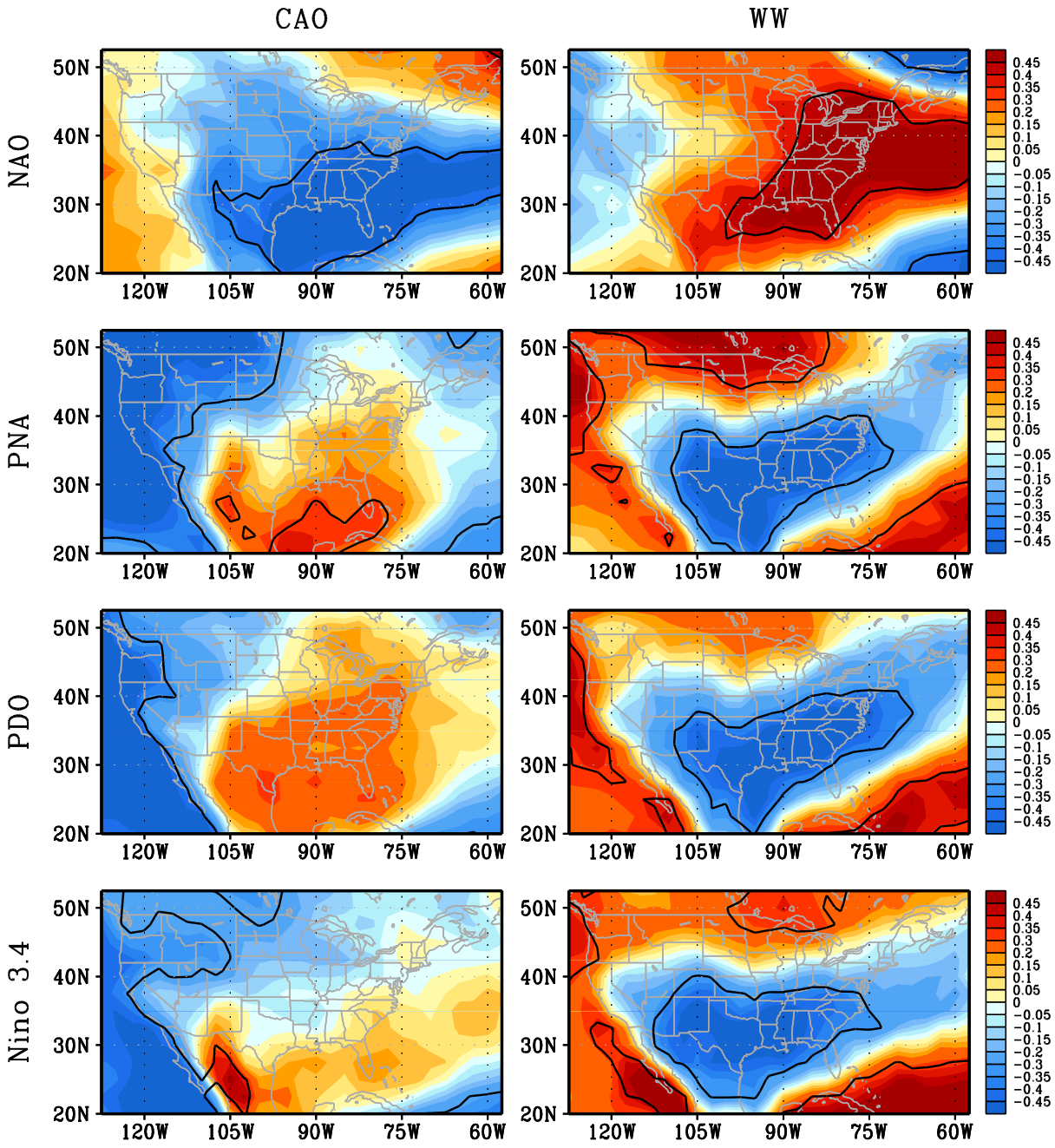

Figure 3.6: Correlation values of the yearly impact factor of cold days (left column) and warm days (right column) using detrended data and the seasonal-mean NAO Index (first row), PNA Index (second row), PDO Index (third row) and Niño 3.4 Index (fourth row), 1950-2011. The black closed contours indicate statistical significance at the 95% confidence level.

Another interesting result evident in Figure 3.6 relates to ENSO (based on the Nino 3.4 index) and its impact upon ETRs. Contradictory to the conventional understanding based on seasonal-mean temperatures, the influence of ENSO upon ETRs seems to be mainly limited to a modest modulation of WWs over the Southern US. There appears to be little influence by ENSO on CAOs, given the lack of statistically significant correlation over much of the US, except for the far west and Pacific-Northwest US. This suggests that these particular characteristics of ETRs, especially CAOs, may not be as sensitive to ENSO events as originally inferred.

The correlation analysis also reveals that a greater number of low-frequency modes are implicated in modulating WWs (4) compared to CAOs (1) in the eastern United States, while the reverse is true over the western United States (0 and 3, respectively). This is a previously unrecognized result. Based on these findings, for the eastern United States it appears easier to attribute interannual variability in WWs to low-frequency mode modulation than is possible for CAOs, while the opposite appears to be true for ETRs over the western United States. Thus, overall, the correlation analysis indicates that (i) ETRs in specific regions of the United States are modulated by certain low-frequency modes and (ii) there is an apparent asymmetry between the regional low frequency modulation of CAOs and WWs. This asymmetry may be related to the higher-order statistical moments, such as skewness and kurtosis.

3.3.3. Quantifying the low frequency mode modulation of ETRs

The multiple linear regression (MLR) analysis reveals that a linear combination of two predictors explains the maximum amount of variance in most cases, even though the

optimal combination of predictors was not limited to any specific number. Overall, where statistically significant correlations between ETRs and low-frequency modes exist in the United States (i.e., Fig. 3.6), various combinations of these low-frequency modes explain between 10% and 50% of the variance in the ETR metrics.

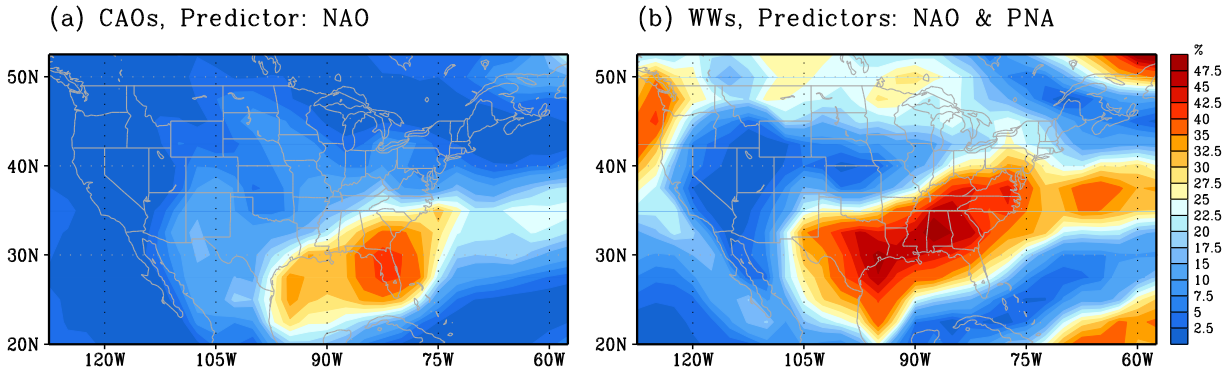

Figure 3.7: Variance explained (%) by multiple linear regressions for the yearly impact factor of warm (cold) days, with the NAO and PNA (NAO) as Predictors, Detrended, 1950-2011.

To provide a specific example, we consider the behavior of boreal cool season WWs and CAOs over the Southeast United States, which is impacted by all four low-frequency modes considered. The results of our MLR indicate that one predictor, the NAO, is the optimal subset of predictors for CAOs over the U.S. Southeast, explaining approximately 30% of the interannual variability (Figure 3.7, left panel). This finding agrees with the correlation maps provided in Fig. 3.6, which show that of the four low-frequency modes of interest, only the NAO provides a statistically significant modulation of CAOs in the Southeast. In contrast, the combination of the NAO and PNA indices is the optimal set of predictors for WWs in this region, explaining over 50% of the interannual variability (Figure 3.7, right panel). In fact, this combination of predictors

explains between 40% and 50% of the variability in the impact factor of warm days over a very large area, covering most of Texas and extending eastward through the Southeast and then northeastward into Kentucky and Virginia. These results are also consistent with the correlation patterns plotted in Fig. 3.6. Conversely, very little of the WW variability over the western United States is accounted for by the same two predictors. This is because neither the PNA nor the NAO have a statistically significant relationship with WWs in this region (Fig. 3.6, right). Therefore, in principle, in regions where low-frequency modes are significantly correlated with ETR metrics, predictions of the implicated low-frequency modes could be used to forecast at least a portion of the seasonal impact of ETRs.

3.4 Summary & Conclusions

In this research, we provide a baseline quantification of long-term ETR statistics. A range of statistical analyses were applied to (i) examine long-term variability in the regional impact of ETRs, and (ii) identify and quantify interannual modulation of ETR behavior by prominent modes of low-frequency variability.

Analyses of long-term ETR variability reveal that there have not been any statistically significant trends in either WWs or CAOs over most of the continental United States from 1949 to 2011. Nonetheless, strong interannual variability in ETRs is still evident and is linked to several prominent low-frequency modes. More specifically, a correlation analysis shows that regional ETR behavior is modulated by certain low-frequency modes with important regional asymmetries between the low frequency mode modulation of CAOs and WWs. In particular, we discover that the low-frequency

modulation of WWs over the eastern United States is considerably more robust than the parallel modulation of CAOs. Further, the influence of ENSO upon ETRs is found to be mainly limited to a modest modulation of WWs over the southern United States. This result counters prior studies of seasonal-mean temperature. Additionally, multiple linear regression analyses demonstrate that the collective influence of low-frequency modes can account for as much as 50% of the regional interannual variability in ETR behavior.

Extreme temperature regimes will remain of interest to weather forecasters because of their socioeconomic impacts. Based on the results of this research, particularly the lack of trends in historical ETR variability, ETRs may occur just as frequently and intensely as they have over the past 60 years. Therefore, accurate prediction and forecasting of these events remains desirable. However, our analysis has thus far been primarily statistical in nature, and therefore has not established the physical nature or mechanisms connecting ETRs to low frequency modes. The fact that the frequency and amplitude of CAOs in the United States has not changed, even with increasing background temperatures in the source regions, provides impetus for identifying and understanding the mechanisms responsible for CAOs. Furthermore, there is little existing research on the physical nature of boreal cool season WWs and low frequency modes. These topics are pursued via detailed diagnostic analyses of three-dimensional synoptic and dynamic circulation structures in the next chapter (Chapter 4).

CHAPTER 4

SYNOPTIC EVOLUTION AND CONNECTIONS TO LOW FREQUENCY MODES

The work presented in this chapter is in press in Weather and Forecasting (Westby and Black, 2015).

4.1 Background & Motivation

The important regional impacts of boreal winter CAOs and WWs underscore the necessity for regional preparedness in anticipation of future changes in their behavior (Kodra et al. 2011, Park et al. 2011, Scherer and Diffenbaugh 2014). To better understand these changes in ETRs, it is necessary to have a more complete understanding of the synoptic and physical nature of ETR events in the current climate, including the role of low frequency modes. An enhanced understanding of ETRs will allow us to more skillfully predict ETRs, adequately assess the ability of climate models in representing ETR events and better characterize the uncertainties in future projections in ETR behavior.

Several prior studies have examined the typical synoptic behavior of CAOs, while parallel studies of boreal winter WWs are rare in the literature. Past studies have identified several favorable synoptic conditions for CAOs occurring east of the Rocky Mountains: a 500 hPa dipole pattern with ridging (troughing) over the western (eastern) US (Hartjenstein and Bleck 1991, Colle and Mass 1995), high-latitude ridging at 500 hPa (Konrad 1998), a corresponding surface couplet with an anticyclone (cyclone) over the Western (Eastern) US (Konrad and Colucci 1989, Colle and Mass 1995, Konrad

1998, Ashcroft et al. 2009), cold-air mass advection across 55°N (Hartjenstein and Bleck 1991) and transient waves (Konrad 1998). This upper level ridge-trough pattern and surface couplet controls the strength of the meridional circulation, leading to strong northerly flow that transports cold air from high latitude source regions, ultimately leading to CAO onset. However, a few studies have found that, for the southeast (SE) US, the anticyclone strength plays a more important role than the accompanying cyclone in CAO onset (Konrad and Colucci 1989, Konrad 1996, Konrad 1998). This is especially true when cyclogenesis occurs after the initiation of the CAO event, and has been found to be associated with the strongest CAO events (Konrad and Colucci 1989, Konrad 1996). The timing of the surface cyclogenesis relative to event onset also affects the relative contributions of cold air advection and adiabatic processes during event onset (Konrad and Colucci 1989). On the other hand, very few studies on the synoptic behavior of winter WW events exist. A study by Teng et al. (2013) found that heat waves are typically preceded by a wavenumber-5 quasi-stationary wave pattern. Even though the study mainly focuses on summer heat waves, they remark that this wave pattern is observed in both winter and summer and thus may account for heat waves in both seasons. In principle, this type of circulation could provide the necessary warm air advection characteristic of WW events into the region of interest. It also makes sense to expect that the anomaly patterns associated with warm events are of opposite sign to, but structurally similar to, those associated with CAOs (Loikith and Broccoli 2012). In the accounts presented thus far, it is clear that synoptic scale circulations are critical to ETR development; however, it is also possible that these smaller-scale circulations may be embedded within larger planetary-scale circulation patterns that may persist much longer

(Konrad 1998). Therefore, circulations on a variety of scales may contribute to the formation of ETRs, ranging from frontal scale features up to hemispheric low frequency modes.

Indeed, prior statistical research has identified linkages between ETRs and the amplitude and phase of several low-frequency modes of variability. The most extreme temperatures tend to occur when the index value of at least one low frequency mode is in the upper or lower quartile of the distribution (Loikith and Broccoli 2014). Specifically, US CAOs have been linked to the positive phase of the Pacific-North American (PNA) teleconnection pattern (Downton and Miller 1993, Vavrus et al. 2006, Cellitti et al. 2006, Rogers and Rohli 1991, Westby et al. 2013, Loikith and Broccoli 2014), and the negative phases of the North Atlantic Oscillation (NAO) (Walsh et al. 2001, Cellitti et al. 2006, Westby et al. 2013), Arctic Oscillation (AO) (Lim and Schubert 2011), and Northern Annular Mode (NAM) (Loikith and Broccoli 2014) (noting that the NAO, AO and NAM are interrelated). Connections between CAOs and the positive phases of the Pacific Decadal Oscillation (PDO) (Westby et al. 2013) and El Nino-Southern Oscillation (ENSO) (Lim and Schubert 2011, Westby et al. 2013, Loikith and Broccoli 2014) have also been identified. Meanwhile, WW frequency is enhanced by the positive phase of the NAO and the negative phases of the PNA, PDO and ENSO (Westby et al. 2013). However, some of these low frequency modes seem to play a more important role than others. For instance, Loikith and Broccoli (2014) find that the PNA and NAM modes are more important than ENSO in modulating extreme temperatures over North America, and that the PNA is slightly more dominant than NAM. Westby et al. (2013) also find a weaker relationship between ENSO and ETRs compared to the PNA or AO. This is likely

because the primary atmospheric circulation anomalies associated with these modes of variability are more prominent over the continent and thus provide a stronger direct influence on temperatures in these regions. Low frequency modes also play a more prominent role in modulating ETRs in particular regions (e.g. the SE) of the US compared to others, and the simultaneous contribution of multiple modes may also be important (Loikith and Broccoli 2014, Westby et al. 2013). For example, over the SE region, nearly 30% of the interannual variability in CAOs can be attributed to the NAO, while over 50% of the variability in WWs can be attributed to the combined influence of the NAO and PNA (Westby et al. 2013).

Although there is a significant relationship between ETRs and the phase and magnitude of several low frequency modes, this is an imperfect relationship since the modes only explain a fraction of the interannual variability in ETRs (Westby et al. 2013). Therefore, other factors are required to account for the remaining variability. Loikith and Broccoli (2014) found that local, transient, synoptic-scale weather features represent another important factor for ETRs in many locations, and they often occur in conjunction with an unusually strong phase of an influential low frequency mode. For example, a CAO case study by Bosart et al. (1996) found that a 1993 CAO event resulted from an interaction between the slowly evolving planetary-scale circulation (perhaps associated with a teleconnection pattern) and a rapidly moving smaller-scale transient feature. Thus, there is not a one-to-one relationship between ETRs and low frequency modes. Other factors, such as synoptic-scale disturbances (Bosart et al. 1996) or internal variability (Teng et al. 2013), must come into play and may interact with the low-frequency modes through a positive feedback process that leads to the formation of ETRs. Given a

collective consideration of these studies, we hypothesize that the large-scale modes may be important in helping to form the predecessor cold or warm air masses, while the synoptic features provide a physical trigger to transport these air masses elsewhere and hence lead to ETR formation.

This current study applies categorical composite analyses to identify the primary synoptic and dynamic features associated with historical ETR onset over the SE US. The objective of our study is to provide a structured, comprehensive and updated analysis of the typical nature of SE ETRs emphasizing their linkage to prominent low frequency modes. Many studies thus far have focused on the statistical characteristics of ETRs (Walsh et al. 2001, Portis et al. 2006, Westby et al. 2013, among many others), examined the synoptic nature of individual cases (Bosart et al. 1996, Schultz et al. 1997, Colucci et al. 1999, Hartjenstein and Bleck 1991, Konrad and Colucci 1989), or have performed composite analyses without explicit consideration of the roles of low frequency modes (Portis et al. 2006, Dallavalle and Bosart 1975, Konrad 1996, Colle and Mass 1995, Loikith and Broccoli 2012). Further, as discussed above, there is little or no existing research on the behavior of boreal cool season WWs. The current research aims to fill these gaps.

Given the prominent role of low frequency modes in modulating SE ETRs (Westby et al. 2013), we choose to focus our attention on CAOs and WWs occurring in the SE US in the current study. In our approach, we will first categorize events in terms of the phase and amplitude of the primary implicated low frequency modes, allowing for a more explicit delineation of their physical role. We will then study the composite time evolution of the temperature and circulation anomaly patterns leading up to and during

ETR onset. These analyses aim to identify key atmospheric features associated with high-impact ETR events to aid local forecasters with precursor pattern recognition and improve the accuracy of predictions of ETRs over the region of interest.

4.2 Data & Methods

Once the detrended SAT anomalies were calculated for the period 1948-2011 for this region as described in Chapter 2, discrete ETR events were identified using magnitude, duration and separation criteria. The first requirement is that each warm wave (cold air outbreak) consists of times when the SAT anomalies exceed (fall below) $+1\sigma$ (-1σ). Using this threshold ensures an adequate sample size for statistical significance testing. Second, each event is required to last at least 5 days. The duration requirement of 5 days allows us to study relatively high impact events. Third, to ensure independence, events in each category are required to be separated from one another by at least 10 days.

Table 4.1: Number of CAO and WW events that occurred in the Southeast US from 1949-2011 during various phases of low frequency modes and the average length of the events during that phase.

	Number of Events	**Average Length of Events (days)**
SE CAOs, Neutral NAO (Case 1)	**12**	**7.18**
SE CAOs, Negative NAO (Case 2)	**17**	**9.28**
SE CAOs, Positive NAO*	**0**	**–**
SE WWs, Neutral PNA (Case 3)	**11**	**7.20**
SE WWs, Negative PNA (Case 4)	**12**	**8.77**
SE WWs, Positive PNA*	**1**	**–**

* The events in the positive low frequency mode categories are not well represented and therefore are not assigned a case number or considered further in our analysis.

Composite analyses are used to identify fundamental synoptic circulation signatures and precursor features unique to specific classes of extreme events (Chen and

Zhai 2014, Sisson and Gyakum 2004, Grotjahn and Faure 2008, Milrad et al. 2009) and are used extensively in the current analysis. The composites were created by first categorizing warm wave (WW) or cold air outbreak (CAO) events by the sign and magnitude of the monthly low frequency mode index for the month of occurrence. Following the results of Westby et al. (2013), where it was determined that the NAO and PNA both strongly modulate ETR frequency in the SE (their Fig. 4), ETR events are classified based on the sign and magnitude of these two low frequency modes. The positive (negative) event category is defined as when the normalized low frequency mode index is $>+1\sigma$ ($<-1\sigma$), while the neutral event category is when $-1\sigma <$ normalized low frequency mode index $< +1\sigma$. The number of events in each category, as well as the average length of events, is provided in Table 4.1. Interestingly, the mean duration of events occurring during negative phases of the low frequency modes are longer than the other categories. Further, the relative lack of ETR events in the positive phases of the low frequency modes provides some insight about conditions that are not favorable for ETR development. However, because of the infrequent occurrence of ETRs during the positive phases of the low frequency modes, those categories are not considered further. Thus, our composite analyses focus on the following four most commonly populated categories:

1) SE CAOs – Neutral NAO, Varying PNA
2) SE CAOs – Negative NAO, Varying PNA
3) SE WWs – Neutral PNA, Varying NAO
4) SE WWs – Negative PNA, Varying NAO

where “varying” indicates no categorization in terms of this index. Our overall event classification is largely guided by the most robust statistical relationships identified in Westby et al (2013). We use “varying” classifications in cases where there isn’t an obvious way to categorize events based on the sign and amplitude of the secondary low frequency mode (partly reflecting the weak statistical relationship). For instance, when the NAO is negative, the events are distributed relatively evenly among the three phases of the PNA. This methodology also ensures that each category of events contains a sufficient number of events to adequately assess statistical significance. The inclusion of neutral cases allows us to directly compare and contrast to the low frequency mode cases, in order to isolate the distinct roles of the low frequency modes. The individual events included in each category are listed in Table 4.2.

Table 4.2: Discrete Event Dates for CAOs and WWs that occurred in the Southeast US from 1949-2011.

	Year	Start Month	Start Day	Start Hour	Length of Event (days)
Case 1 - SE CAOs, Neutral NAO	1955*	12	10	12	5.5
	1958	12	8	12	8.75
	1962	1	9	0	5.25
	1967	2	22	18	6
	1978	1	10	6	5
	1978	1	27	0	15.5
	1983	12	22	18	10.75
	1985	12	16	6	5.5
	1988	1	5	18	5
	1994	1	16	12	5.5
	1996	2	2	0	5.25
	2000	12	18	6	8.25
Case 2 - SE CAOs, Negative NAO	1958	2	8	18	13.25
	1962	12	8	0	8
	1963	1	22	18	5.75
	1963	2	20	18	5.5
	1963	12	14	18	9.75
	1966	1	24	18	12
	1968	2	9	18	17.5
	1970	1	5	12	7.25
	1977	1	14	18	9.25
	1980	1	31	0	6.5
	1982	1	9	12	7.5
	1985	1	19	6	6
	1989	12	14	6	13
	1995	12	22	6	6
	2010	1	2	18	10.25
	2010	2	9	6	9.25
	2010	12	5	18	11
Case 3 - SE WWs, Neutral PNA	1956*	12	13	6	10.25
	1961	2	14	6	9.5
	1982	12	23	12	5.25
	1984	2	11	12	6.5
	1996	2	21	12	5.75
	1998	1	4	6	5
	1999	1	19	0	12.5
	2001	12	4	6	5.25
	2002	1	27	6	5.5
	2004	12	31	6	8.5
	2007	12	9	6	5.25
Case 4 - SE WWs, Negative PNA	1950*	1	11	6	6.75
	1952*	1	14	6	6.5
	1957*	1	28	6	13.75
	1965	12	30	18	5
	1971	12	8	6	8.75
	1974	1	16	6	17.25
	1975	1	26	18	7.25
	1976	2	13	6	7.5
	1984	12	12	6	11.25
	1990	2	11	6	5.75
	1990	12	15	6	7
	1996	12	28	12	8.5

* Indicates dates that are included in the NCEP/NCAR composites, but are ***not*** included in the ERA composites due to the availability of the data.

Time-evolving composite fields are constructed for each the four categories outlined above in order to isolate the synoptic and dynamic structural distinctions among the different categories of ETR events. For the composite anomaly calculations, the background 6-hourly climatological value of each parameter is calculated for the period 1948-2011 (NNR data) or 1958-2011 (for ERA). The time evolution of these composite fields are analyzed relative to the onset day (Day 0, when the anomaly threshold value is first crossed) with Day *n* referring to the *n*th day prior to (negative value) or after (positive value) ETR onset. We construct composites from Day -8 to +4 at 6-hourly intervals, although for space considerations the results are presented at 2-day intervals. We display results for specific days in a temporal window encompassing the period characterized by the strongest statistically significant features (which varies from case to case). Statistical significance is assessed using a two-tailed Student's *t* test with a confidence level of 95%. Statistical significance is displayed as color shading, green contours or bolded black contours as detailed in the figure captions. Nevertheless, we note that although a statistically significant feature in the composite may not occur in every ETR event the composite comprises (Grotjahn and Faure 2008), it is likely present in most cases. Further, local maxima or minima in the composite anomaly field may indicate either (1) the presence of a stronger feature in many of the events or (2) that a given feature is more consistently located in a given location (Konrad 1996).

In order to identify important dynamical features during ETR onset, one of the anomaly fields analyzed in our composite analyses is potential vorticity (PV). Significant PV anomaly features are isolated in both horizontal maps (at 925 hPa and 250 hPa levels) and in vertical cross-sections. In addition, we reiterate that a fundamental part of the PV

anomaly distribution is the distribution of potential temperature anomalies (i.e., "surface theta") at the lower boundary, taken to be 962.5 hPa (see discussion in Chapter 2). Since the lower boundary is a constant pressure surface in an isobaric QG framework, this also implies that the surface potential temperature anomalies are directly proportional to the 925 hPa air temperature anomalies which, in turn, are closely related to the surface air temperature anomaly field (given the proximity of the 925 hPa surface to the ground). Thus, local anomalies in surface air temperature are an effective proxy for identifying the structure in the surface potential temperature anomaly field. Recalling that warm (cold) surface theta corresponds to an effective positive (negative) PV anomaly (Chapter 2), we can directly relate SAT anomaly patterns to effective PV anomaly patterns of opposite sign. For example, a regionalized cold SAT anomaly feature will represent a negative PV anomaly which will serve to induce an anticyclonic horizontal circulation.

Because we are interested in identifying significant features surrounding the time of ETR onset, Days -2, 0 and +2 are studied in the PV anomaly cross sections. The longitudes examined span 60°W to 120°W, which covers the continental United States (CONUS). Vertical cross-sections are constructed at 40°N, 45°N and 50°N. The variety of latitudes and time steps chosen account for the fact that the PV anomalies are often mobile features and also allows us to better discern the 3-dimensional spatial position of individual PV anomaly features.

4.3 Results & Discussion

Composite analyses of the four cases examined in this study indicate that there are large-scale as well as synoptic-scale signatures in several atmospheric variables that can

be tracked backward in time for several days and hence may provide telling information on the impending arrival of such ETR events. Broad quasi-stationary circulations are usually indicative of low frequency mode modulation, whereas smaller-scale mobile circulations generally indicate synoptic features or disturbances. In addition, several structurally coherent and statistically significant features having moderate to strong amplitude are observed in our composite PV anomaly analyses. The results of each of the four cases are detailed in the following subsections.

4.3.1. Case 1 – SE CAOs: Neutral NAO

For SE CAOs, we try to delineate the role of the NAO pattern during CAO onset, given that CAOs are favored during the negative phase of the NAO. Case 1 considers CAO events occurring during the neutral phase of the NAO. Composite time evolution analyses for Case 1 are presented in Fig. 4.1 (horizontal maps of several fields) and Fig. 4.2 (left column, vertical cross-sections of PV anomalies). In this case, a mass of cold air hovers over Canada between Days -8 to -4 (not shown). By Day -2, the western portion of this air mass starts to traverse southward into the central US, in association with northwesterly winds to the east of the Rockies (Fig. 4.1, column 1). Meanwhile, northwesterly winds at the trailing (northward) edge of the cold air mass continue to feed cold air into the system, allowing for air mass intensification. By Day 0, the cold air covers almost all of the central and eastern US, with northwesterly winds still feeding the air mass via an anomalous cyclonic circulation over southeast Canada. The demise of the CAO event begins at Day +2 when the northerlies and resulting cold air advection behind the air mass are shut off (due in part to an anticyclonic circulation that migrates

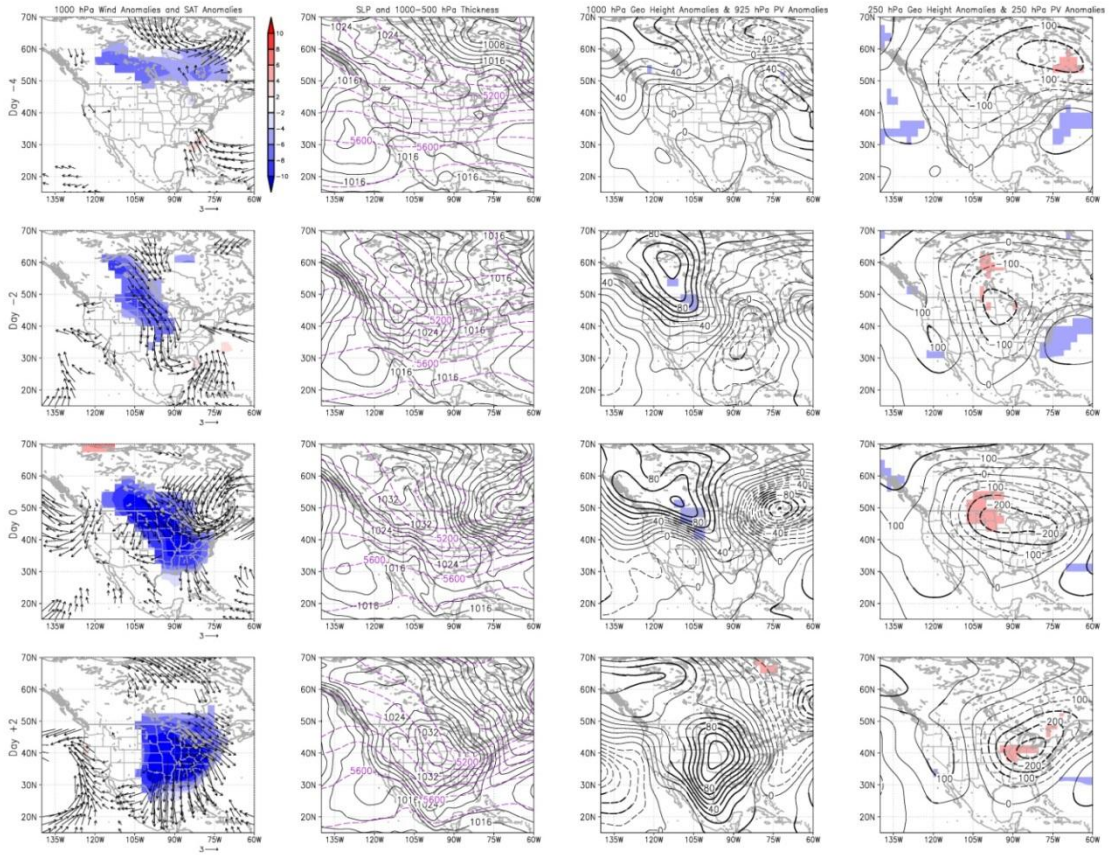

Figure 4.1: Composite Time Evolution Plots for Days -4, -2, 0 and +2 for Case 1 – SE CAOs, Neutral NAO. Column 1: 1000 hPa wind anomalies (m/s) and SAT anomalies (°C, shaded). Column 2: SLP (hPa) (black lines, contour interval of 2 hPa) and total 1000-500 hPa thickness (m) (purple dashed lines, contour interval of 100 m). Column 3: 1000 hPa geopotential height anomalies (m) (black lines, contour interval of 10 m) and 925 hPa PV anomalies (shaded). Column 4: 250 hPa geopotential height anomalies (m) (black lines, contour interval of 50 m) and 250 hPa PV anomalies (shaded). The shaded anomalies in all columns shown are statistically significant at the 95% confidence level. Blue (red) shading represents negative (positive) values. In columns 3 and 4, the shaded PV anomalies indicate the sign only, while the bolded contours indicate where the geopotential height anomalies are statistically significant.

southeastward from Southwest Canada and intensifies). By Day +4, the temperature anomalies have decreased significantly in magnitude (not shown), likely due to the significant reduction in cold air advection.

The role of cold air advection, which has been found to be a key player in CAOs (Colle and Mass 1995), and its association with several prominent synoptic features is confirmed in column 2 of Fig. 4.1. Several days prior to the onset of the CAO events, there is a high pressure ridge extending over western Canada (Day -4), coupled with a region of low SLP over eastern Canada. This synoptic structure may be the factor that initially set the cold air mass into motion. Some prior studies had found that the cold air responsible for CAOs may be forced southward from its high-latitude source region by northerly winds that develop between an anticyclone-cyclone couplet in the lower troposphere (Konrad 1996, Konrad and Colucci 1989). Further, the formation of anticyclones in this region of the high latitudes is a common circulation feature during the winter months as relatively warm maritime polar air from the northeast Pacific flows over the snow and ice surfaces and transforms into a continental polar air mass via radiative cooling, leading to anticyclogenesis (Curry 1987) while also likely contributing to the cold air pool in the high latitude regions. By Day -2, this region of high pressure has intensified and become meridionally elongated, leading to strong cold air advection along its eastern flank where northwesterly winds are crossing the thickness contours. Further, the cold air advection is co-located with the region of statistically significant wind anomalies (Fig. 4.1, column 1). By Day 0, the ridge has slightly intensified and becomes tilted with a northwest-southeast orientation, while a robust surface low pressure system has formed over easternmost Canada. The circulation associated with this strengthening

couplet is favorable for both sustaining and spreading the cold air mass southeastward toward the SE (as discussed above). By Day +2, the anticyclone has migrated into the central US and taken on a more circular shape while the low pressure system has propagated well to the east. This change in structure effectively shuts off the cold air outbreak as the closed anticyclonic circulation over the central US begins to feed relatively warm air into the upper Midwest. Finally, by Day +4 (not shown), the cold advection is substantially weaker and limited to the far eastern US, while warm advection continues to occur on the western and northwestern flanks of the high pressure center. This temporal sequencing is consistent with the findings of Konrad and Colucci (1989), who found that some CAOs over the eastern US developed prior to cyclogenesis over the western Atlantic Ocean, and also contains many of the aspects described in Colle and Mass's (1995) conceptual model of CAO events east of the Rocky Mountains.

These synoptic features are also apparent in the 1000 hPa geopotential height anomaly field (Fig. 4.1, column 3), with positive (negative) anomalies corresponding to the regions of high (low) pressure. One key difference between the total SLP field and 1000 hPa geopotential height anomaly field is that the developing surface cyclone over the eastern US is clearly evident slightly earlier (Day -2) in the time evolution of the latter. This cyclone seems to form just ahead of the cold air associated with the CAO event. Otherwise, the two fields match each other quite well. Meanwhile at 925 hPa, we note that statistically significant negative PV anomalies are found in the base of the surface ridge at Days -2 and 0, but no other significant anomaly features are observed. This PV anomaly feature is relatively stationary and would help enact a clockwise circulation. In addition, the developing cold SAT anomaly feature, itself (representing an

effective negative PV anomaly), will also induce an anticylonic circulation. Therefore, both the surface theta and lower tropospheric PV likely help contribute to northerly or northwesterly winds to the east consistent with the other composite analyses presented.

At upper levels, a significant long-wave trough feature is observed over eastern North America, as indicated by the intensifying negative geopotential height anomaly signature at 250 hPa (Fig. 4.1, column 4). Such a feature has also been cited in prior work (Colle and Mass 1995, among others) and provides dynamical support for the surface cyclogenesis. Meanwhile, weaker amplitude positive geopotential height anomalies are present over western North America. The primary PV anomaly signature found at this level is a positive anomaly located near the center of the upper level trough. Unlike the lower tropospheric PV anomaly pattern, the 250 hPa PV anomaly signature is mobile and propagates southeastward as the trough deepens. This feature would result in a counterclockwise circulation, which in most of the time steps shown would be associated with northerly or northwesterly winds over the north central US. The superposition of the upper and lower level PV anomalies would contribute simultaneously to the CAO onset by moving cold air from Canada into the central and eastern US, consistent with the behavior observed in the lower troposphere.

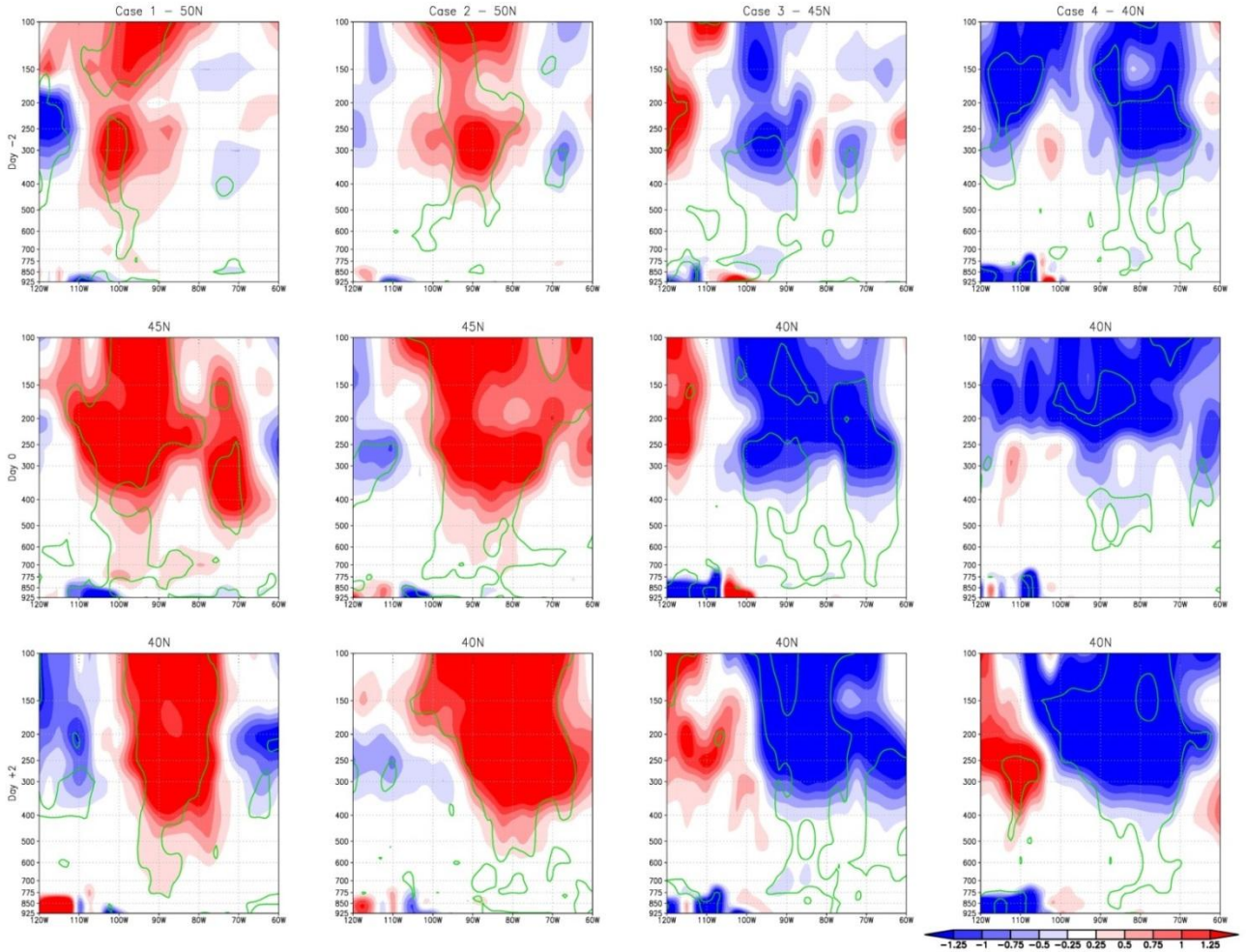

Figure 4.2: Composite Time Evolution Vertical Cross-sections of PV Anomalies for Days -2, 0 and +2 for all 4 cases. The color shading indicates the sign and magnitude of the PV anomalies in PVUs (1 PVU = 10^{-6} $m^2s^{-1}Kkg^{-1}$), while the green contours indicate statistical significance at the 95% confidence level. Blue (red) shading represents negative (positive) values. The latitude of each cross section is specified above each panel.

A consideration of the vertical cross-sections of the composite PV anomaly field (Fig. 4.2, left column) helps us to establish which PV anomaly features are most significant during ETR onset as well as their spatial extent. At Day -2, statistically significant positive PV anomalies in the upper atmosphere (at 50°N) extend from the upper troposphere down to ~750 hPa, while the statistically significant negative PV anomaly signature near the surface extends upward to 850 hPa. By Day 0, the upper level PV signature has strengthened, spatially expanded and propagated southward (centered at 45°N) while the near-surface PV feature has primarily strengthened. At this time, significant positive PV anomalies extend downward to 850 hPa, or just above the planetary boundary layer (PBL). Thus, the positive PV anomaly signature is likely close enough to the surface to promote northerly surface flow. A similar structure is present on Day +2, except that the upper level PV feature has progressed eastward and southward (to 40°N) while most of the near-surface feature is no longer significant. We generally find that for Case 1 the most significant PV anomaly features are found in middle to upper (positive) and lowermost (negative) portions of the troposphere, with the largest anomaly magnitudes above 500 hPa. In addition, the longitudinal phase relationship between the lower level negative PV anomalies and the upper level positive PV allows for the two dynamical features to collectively produce anomalous northerly winds at the surface. The role of the former is most prominent just prior to and during onset while the latter feature persists longer and tends to progress eastward leading the cold air progression. Given the near-surface PV anomaly's somewhat limited role in contributing to the surface wind field, as well as its displacement to the west of the surface circulation, it is likely that a primary contribution to the surface wind field (at least during the latter

portion of the onset period) arises from the negative SAT anomaly discussed earlier. In Figure 4.1 (column 1) on Day +2, the statistically significant wind anomaly pattern is centered around the cold anomaly, which is physically consistent with the circulation around a negative PV anomaly. Additionally, this feature may help contribute to the eastward progression of the CAO event after onset (bringing up the interesting concept of eastward self-progression during the latter stages of ETR onset).

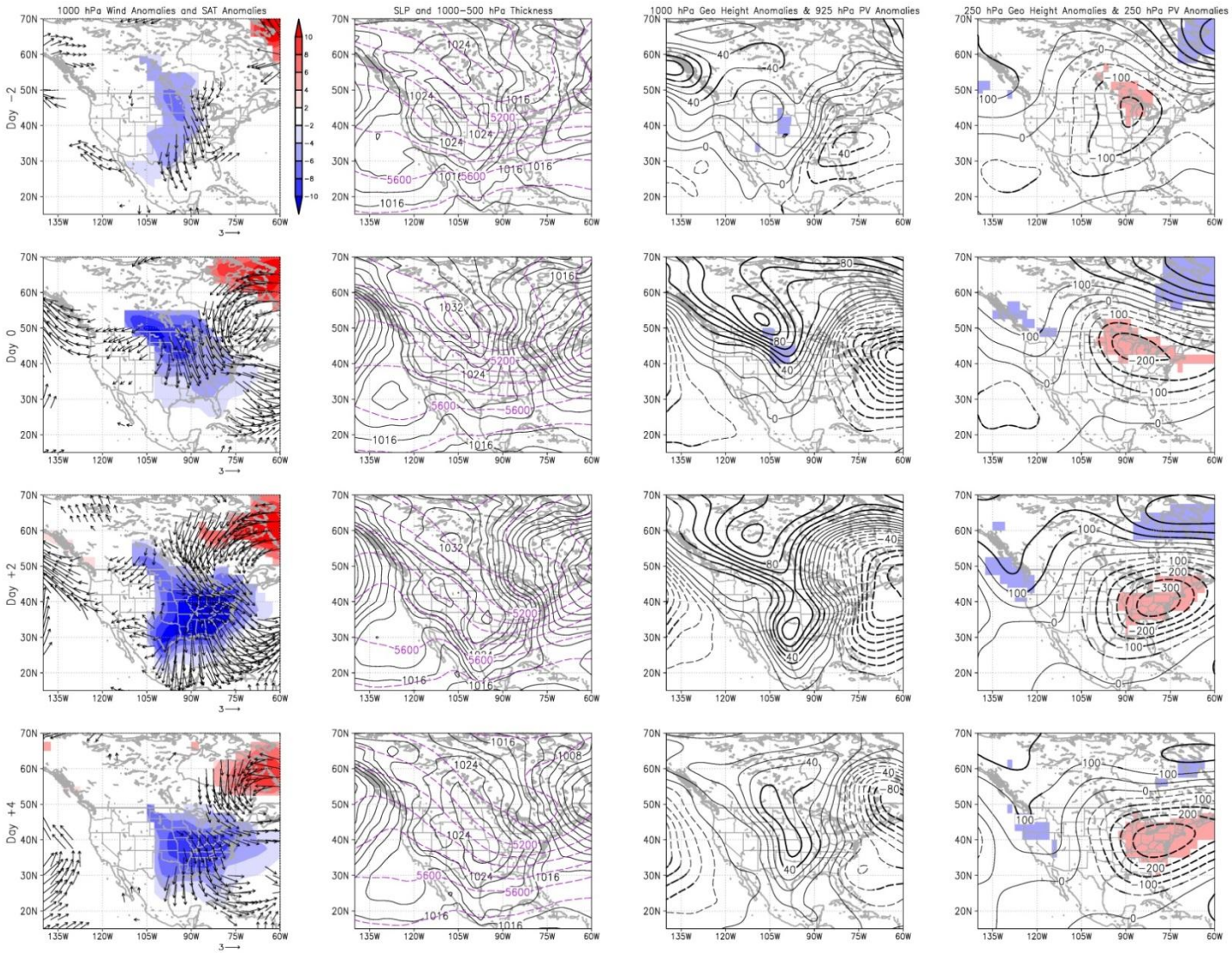

Figure 4.3: Same as Figure 4.1, except for Days -2, 0, +2 and +4 for Case 2 – SE CAOs, Negative NAO.

4.3.2. Case 2 – SE CAOs: Negative NAO

Unlike Case 1, Case 2 CAO events do not begin with a large pool of cold air over Canada that hovers for several days prior to event onset. Significant cold anomalies do not emerge until Day -4 when relatively weak signatures appear over the Pacific Northwest US and south-central Canada, respectively (not shown). By Day -2, these two cold anomaly features have merged, intensified and spread into central North America with a northerly wind signature at the leading edge of the cold air mass (Fig. 4.3, column 1). Unlike Case 1, the anomalous wind pattern in Case 2 does not directly coincide with the temperature anomaly signature, which may account for the weaker temperature anomaly signature at this time lag. Another feature of interest at Day -2 is the emerging region of significant positive temperature anomalies in the far northeast corner of the map. As will be discussed further, this feature arises from the large-scale quasi-stationary circulation associated with the negative NAO phase and is present at all time lags in Fig. 4.3. This feature, not present in Case 1, highlights a fundamental difference between these two types of CAO events. Of course, this is largely anticipated, given the prescribed NAO categorization used in creating the composites. In fact, a significant NAO signature is observed in the height anomaly field over the North Atlantic Ocean at least 8 days prior to CAO onset. The longitudinal extent of the NAO circulation anomaly pattern during winter allows it to directly influence the eastern portions of North America (Thompson and Wallace 2001, Cellitti et al. 2006, Hurrell 1995). By Day 0, there is a noticeable increase in the intensity and spatial extent of the cold air mass, which now covers most of the central and eastern US. At this time, there is a substantial north-northwesterly circulation anomaly signature coincident with the cold pool. The eastern portion of this

pattern is part of a broader large-scale cyclonic circulation signature that emanates from the North Atlantic in association with the concurrent negative NAO pattern. Ironically, this easterly onshore flow into northeastern Canada is also responsible for the surface warm anomaly pattern that develops over northeast Canada. However, the role of temperature advection in producing the cold pool anomaly intensification between Days -2 and 0 isn't immediately clear (given the lack of statistically significant northerly wind anomalies trailing the cold air mass, as was seen during intensification in Case 1). It is possible that some other in-situ mechanism (or aspects of case-to-case variability) helps account for this rapid intensification. By Day +2, the cold air pattern has intensified and expanded further with largest anomaly magnitudes located over the eastern and southeastern US. However, northeasterly flow coming from the emerging warm anomaly over northeast Canada (which has intensified and expanded) is now funneling warm, moist air *toward* the northern edge of the cold air mass. This subsequently serves to effectively "shut off" the ability of the large-scale circulation to tap into cold continental air from Canada, not only preventing the CAO from further intensification, but also leading to its eventual demise. It is evident that this weakening process has begun by Day +4. We normally think of the NAO as creating favorable conditions in the atmospheric circulation for cold air to funnel into the eastern US since it is associated with a trough over the eastern US (e.g., Fig. 4.3; column 4). However, as illustrated here, the role of long-lived NAO events may not be quite so straightforward as the NAO can also contribute to CAO demise at longer time lags. Thus, the role of the NAO in CAO events may be *self-limiting*, as it can both help initiate CAO onset (at short time lags) as well as contribute to CAO demise (at longer time lags). The duration of the CAO events is likely

determined by how fast the warm anomaly over northeastern Canada sets up, which may ultimately be related to the strength of the NAO. However, even though the CAO events in Case 2 dissipate rapidly in response to the modulation by the negative NAO, the average length of the events in this category is still longer than in the neutral NAO case (Case 1). This is consistent with the expectation that the ETR events associated with quasi-stationary features have longer time-scales.

Several days prior to CAO onset (Day -4), a high pressure region exists over southwest Canada with low pressure over eastern Canada and the western Atlantic (not shown), similar to the initial set up for Case 1. However, the two case evolutions diverge thereafter. By Day 0, the region of high pressure has intensified and expanded southward into the western US, leading to cold air advection along the eastern flank of the surface ridge, while the low pressure center also strengthens (Fig. 4.3, column 2). This general pattern persists through Day +4, with minimal propagation eastward. By Day +4, the cold advection over the eastern US has weakened, consistent with a weakening of the SLP couplet. This sequence of events confirms the anomalous circulations in the wind field and is consistent with the evolution of the temperature anomalies.

These features are also evident in the 1000 hPa geopotential height anomaly field (Fig. 4.3, column 3), with significant positive (negative) height anomalies over the western (eastern) US. Another feature of interest is the region of positive geopotential height anomalies observed just off the western coast of British Columbia. These anomalies are initially present at Day -4, but have strengthened by Day -2. By Day 0, this feature has moved eastward and merged with another ridge over the eastern slopes of the Rockies. Therefore, unlike Case 1, Case 2 onset is strongly affected by a large-scale low

frequency mode juxtaposed with a migratory synoptic-scale disturbance. It appears that the synoptic-scale disturbance originally over western North America interacts with the NAO circulation to produce a more intense ETR. This observation is consistent with prior research that has shown that high-frequency transient eddies can amplify teleconnection patterns via positive feedback (Barnes and Hartmann 2010 and references therein). At 925 hPa, statistically significant negative PV anomalies are located within the surface ridge at Days -2 and Day 0, similar to Case 1. These PV anomalies remain stationary, as they do in Case 1, over the northern Great Plains and would help to promote a clockwise surface circulation. This would produce northerly or northwesterly winds over the north central US consistent with the other fields presented. In addition (and similar to Case 1), the cold SAT anomalies, themselves, will likely help promote northerly flow to the east by acting as an effective negative PV anomaly.

In the upper troposphere, a persistent long-wave trough is observed over eastern North America, associated with negative geopotential height anomalies at 250 hPa (Fig. 4.3, column 4), and intensifies through the onset period. As expected during a negative NAO event, this trough is paired with an oppositely-signed ridge feature to the north. This pairing is further exemplified in Fig. 4.4A (right column) where the negative NAO signature over the North Atlantic Ocean is clearly evident. This quasi-stationary north-south dipole structure is distinct from the more transient and mobile trough structure observed in Case 1, and is evident by the comparison provided in Figure 4.4A. There is also a weaker amplitude positive height anomaly feature over the west coast of North America. The parallel 250 hPa PV anomaly evolution reveals two persistent and roughly quasi-stationary features consistent with the geopotential height field: A low over high

dipole over the eastern portion of the domain and a negative anomaly feature over the west coast. These features are more expansive and geographically fixed than those observed in Case 1. The eastern PV dipole structure would be associated with a circulation that would favor both northerly flow over the central US and easterly flow over northeast Canada contributing to both CAO onset as well as its follow-up demise via onshore flow over eastern Canada. The region of negative PV anomalies in the upper ridge over the west coast is probably located too far away from the CAO event to make an appreciable direct contribution, but may indirectly play a role by developing the surface high-pressure system east of the Rockies which in turn contributes to the CAO. This upper level anticyclonic signature is not as prominent in Case 1, but has been identified in prior studies as an important feature during CAO events in the SE US (e.g. Konrad 1998).

The vertical PV anomaly cross-sections for Case 2 are discussed next (Fig. 4.2, second column). Although there is some qualitative commonality with Case 1, there are also differences that parallel the discussion of Fig. 4.3. First, the upper-level positive PV anomaly signature is longitudinally more expansive and less mobile in Case 2 than Case 1. In addition, the relatively stationary nature of the upper level PV anomaly feature identified in the horizontal PV anomaly maps (Fig. 4.3) is also evident in the vertical cross-sections, as the primary vertical axis remains centered near 90W during onset. Similar to Case 1, at Day 0 significant positive anomalies extend down to about 775 hPa or just above the PBL. There is also a region of significant negative anomalies near the surface over the western US at this time, as noted in Fig. 4.3 (column 3). However, the lower-level negative PV anomaly feature (located in the surface ridge) is weaker and less

statistically robust in Case 2. By Day +2 the two features are more clearly detached from one another as the mid-tropospheric signature erodes above the PBL. As in Case 1, the upper-level positive anomaly signature is strongest at this time lag. Further, the strongest lower level negative PV anomalies are located to the west of the positive PV anomalies at upper-levels. This placement allows for the collective influence of both anomalies in producing northerly winds at the surface, as discussed earlier. Further, and as discussed for Case 1, it is likely that a contribution to the surface wind field (especially during the latter portion of the onset period) arises from the negative surface temperature anomaly. In Figure 4.2 (column 2) on Days +2 and +4, the eastern portion of the wind anomaly pattern is consistent with the induction of anticyclonic flow by the cold SAT anomaly (which acts as an effective negative PV anomaly).

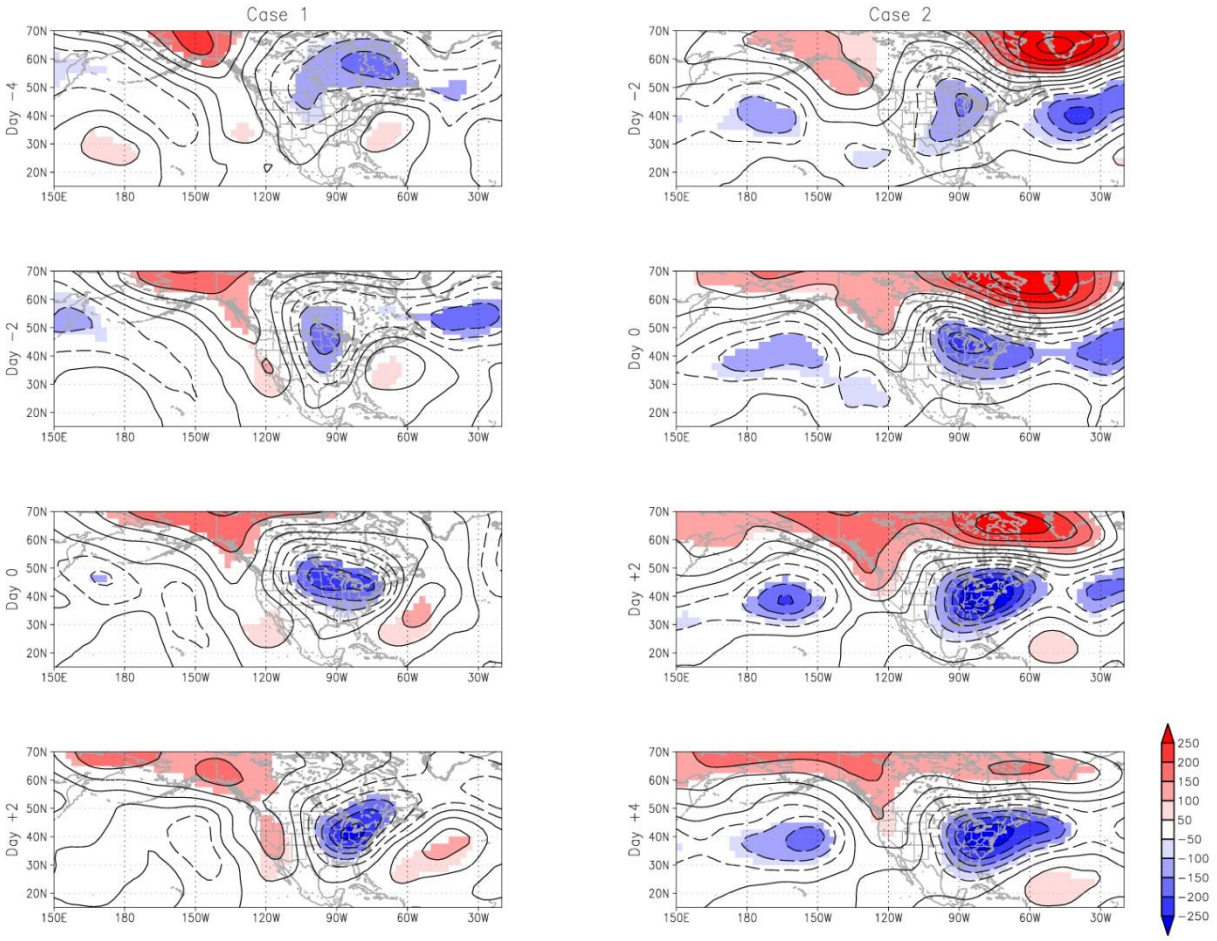

Figure 4.4A: Composite Time Evolution Plots for 250 hPa geopotential height (m) (black lines, contour interval of 50 m) for Days -4, -2, 0 and +2 for Case 1 – SE CAOs, Neutral NAO and Days -2, 0, +2, and +4 for Case 2 – SE CAOs, Negative NAO. The shaded anomalies indicate magnitude and statistical significance at the 95% confidence level.

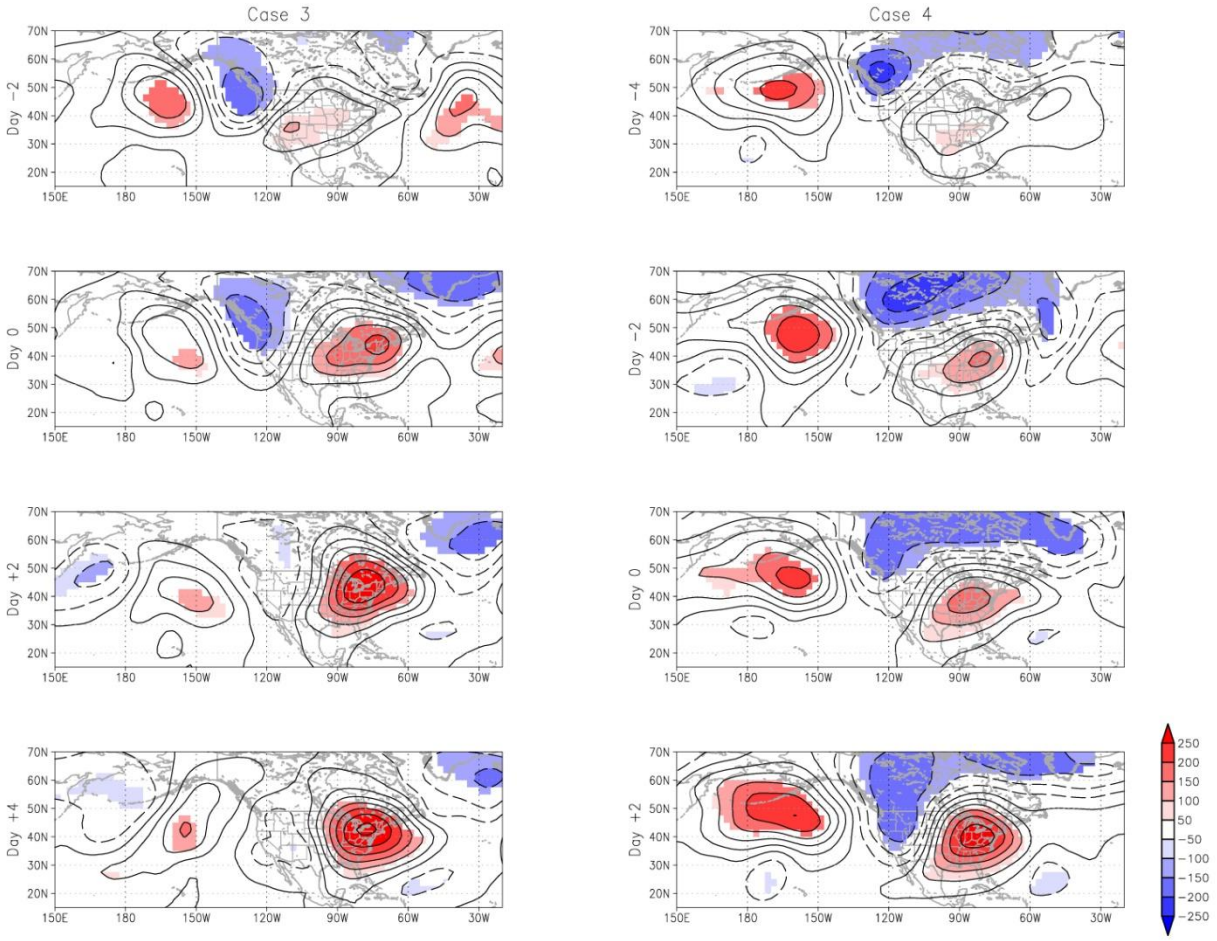

Figure 4.4B: Composite Time Evolution Plots for 250 hPa geopotential height (m) (black lines, contour interval of 50 m) for Days -2, 0, +2, and +4 for Case 3 – SE WWs, Neutral PNA and Days -4, -2, 0 and +2 for Case 4 – SE WWs, Negative PNA with an expanded domain to include the Pacific Ocean to highlight the role of the wave train. The shaded anomalies indicate magnitude and statistical significance at the 95% confidence level.

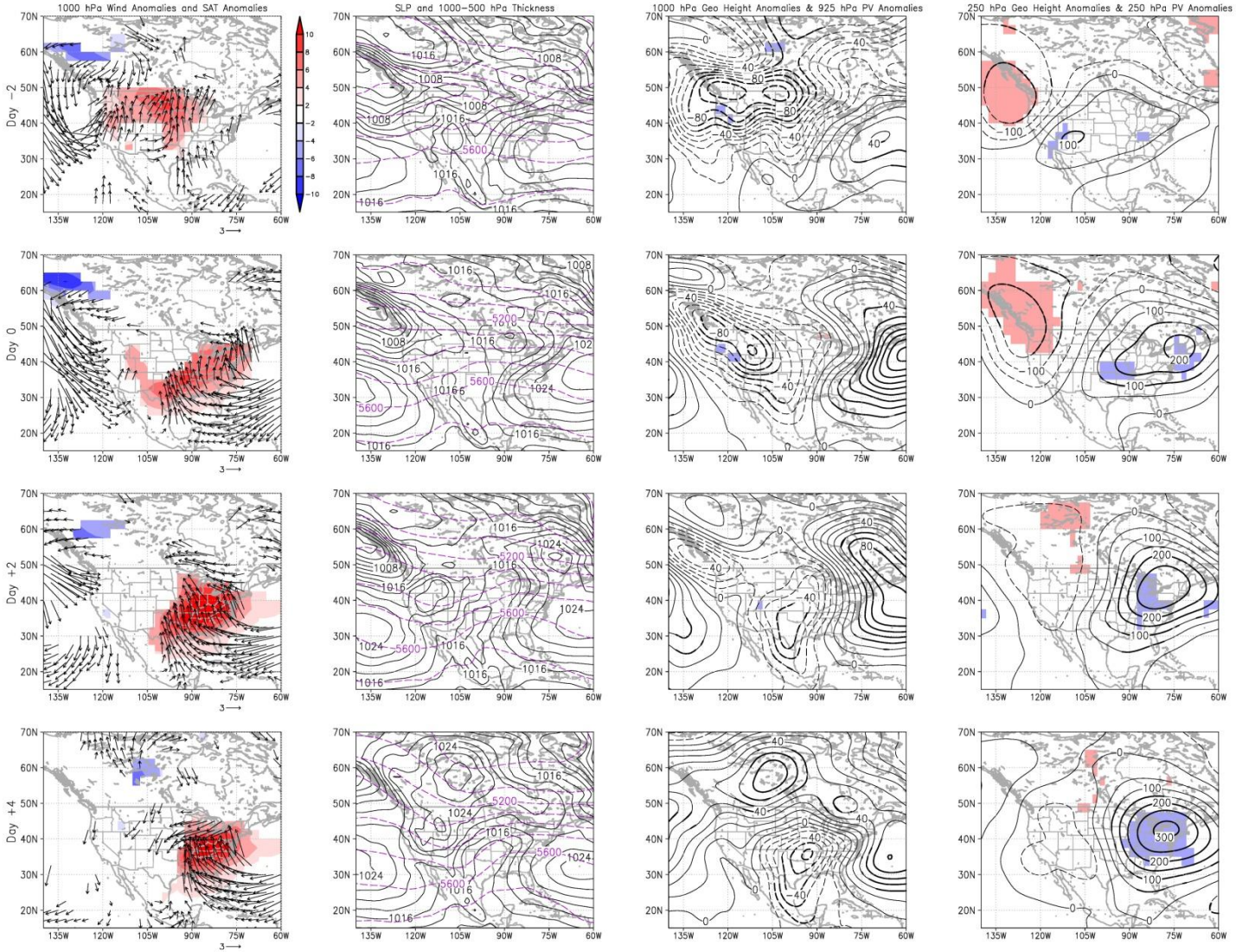

Figure 4.5: Same as Figure 4.1, except for Days -2, 0, +2 and +4 for Case 3 – SE WWs, Neutral PNA.

4.3.3. Case 3 – SE WWs: Neutral PNA

The WW counterparts to CAOs are discussed next. For SE WWs, we attempt to delineate the role of the PNA pattern in WW onset, noting that WWs are favored during the negative phase of the PNA (Westby et al. 2013). Case 3 considers WW events occurring during the neutral phase of the PNA with the composite synoptic analyses presented in Fig. 4.5. Prior to WW onset, an anomalous cyclonic flow develops over the west coast of North America with anomalous southerly flow at its leading edge producing local surface warming (Fig. 4.5; column 1). At Day -2, we also see the initial circulation signature over the SE US of an anomalous high-pressure system forming in situ over the western North Atlantic. By Day 0, the cyclone has extended southeastward and the combined circulation signature of this cyclone/anticyclone couplet leads to a broad swath of anomalous southerly flow extending from Texas to New England. An elongated warm air anomaly forms in association with this southerly flow. By Day +2, the warm anomaly has intensified and expanded into the upper Midwest. Around Day +4 (not shown), the event starts to weaken as the warm air advection reaches a peak. The evolving wind field in this case appears to be associated with both mobile (cyclone) and quasi-stationary (anticyclone) synoptic features.

The cyclone/anticyclone couplet is also evident in the SLP field (Fig. 4.5, column 2). On Day -2, there is a trough of low pressure extending into the Pacific Northwest from the Gulf of Alaska and a developing high pressure system just off the SE Coast. These pressure features are linked to the anomalous circulations presented in column 1, and warm advection occurs over the north central US in association with the low pressure feature. By Day 0, both have intensified, with the trough (high pressure system)

expanding southeastward (northeastward) and a broad area of warm advection extending in between. A distinct low pressure system emerges by Day +2 over the southern US, while the trough over the Pacific NW becomes less distinct. These features are separated by a weak high pressure system. Meanwhile, the high pressure system to the east of the US strengthens and becomes anchored over Bermuda (akin to a Bermuda High). Southerly flow becomes concentrated in between the southern low and the Bermuda High, feeding warm air into the eastern US. However, by Day +4 the areal extent of the warm advection is reduced, in association with the eastward movement of the surface low.

Many of these synoptic features are also evident in the 1000 hPa height anomaly field (Fig. 4.5, column 3), with negative (positive) anomalies corresponding to anomalous low (high) pressure. The height anomaly field isolates the migratory behavior of the surface low pressure system as well as the more in situ development of the offshore high pressure system. Little to no coherent structure exists in the accompanying 925 hPa composite PV anomaly field, in contrast to the earlier discussed CAO cases. However, the developing warm anomaly feature, itself, serves as an effective positive PV anomaly feature at the lower boundary and will likely induce a cyclonic circulation at the surface.

In the upper troposphere, a weakening (strengthening) trough (ridge) anomaly is observed over the western (eastern) North America (Fig. 4.5, column 4). This pattern is generally opposite to those observed for the CAO cases. The negative geopotential height anomalies are associated with the trough, while the positive anomalies are indicative of the ridge. On Day -2, the primary features of significance are (a) the broad negative height anomaly feature off the Pacific Coast and (b) a short wave ridge anomaly over the

southwest US. By Day 0, both have propagated eastward with a new ridge feature arising over the northeast US. Thereafter, the trough dissipates while the two ridge features merge, intensify and stall over the northeast US. The simultaneous weakening of the upstream trough and strengthening of the downstream ridge is consistent with eastward dispersion of Rossby wave energy (e.g., Blackmon et al. 1984a,b). The upper level ridge feature is likely dynamically linked to the oceanic surface high located to its east. Both the western trough and eastern ridge are associated with statistically significant PV anomaly features at 250 hPa that track the movement and intensity of the upper level height anomaly features. Both a decaying positive PV anomaly to the west and a strengthening negative PV anomaly to the east are configured in such a manner to contribute (intermittently) to anomalous southerly flow observed initially over the upper Midwest (Day -2) and thereafter over the eastern US.

Vertical cross-sections of composite PV anomalies for Case 3 are presented in column 3 of Fig. 4.2. Two days prior to WW onset, there are significant large-amplitude upper-level PV anomalies at 45°N in association with the western trough (positive anomalies) and the two eastern ridge features (negative anomalies). Below 500 hPa the PV anomaly signature is locally either weak in amplitude or insignificant (or both). The sole exception to this rule is a modest negative anomaly feature centered around 775 hPa at 95°W. By Day 0, the two significant negative PV anomaly features begin to merge at upper levels. Appreciable anomaly amplitudes extend downward from these two features to the mid-troposphere (~500 hPa). There are no notable significant PV anomaly structures found in the lower troposphere. The upper level negative PV anomalies may contribute to the southerly surface winds observed over the south-central US at this time.

By Day +2, the two lobes have shifted eastward slightly while continuing to slowly merge longitudinally. It is useful to note that we end up focusing our WW cross-sections primarily along 40°N (except for Day -2 of Case 3). This reflects the general latitudinal stationarity of the most prominent WW dynamical features in contrast to the gradual southward movement of key dynamical features for the CAO events. Another distinction between the WW and CAO events is the general lack of coherent lower level PV anomaly features having appreciable amplitude and/or significance in WW cases, suggesting that WW events may be largely driven by upper tropospheric dynamics. Nevertheless, and like the CAO cases, it's likely that at least some of the near surface circulation can be attributed to the warm surface temperature anomaly, itself, especially the southerly flow observed on the eastern periphery of the warm anomaly. However, the suggested role of the surface temperature anomaly in this case isn't quite as obvious as it was in the CAO cases as southerly flow occurs over a rather broad region.

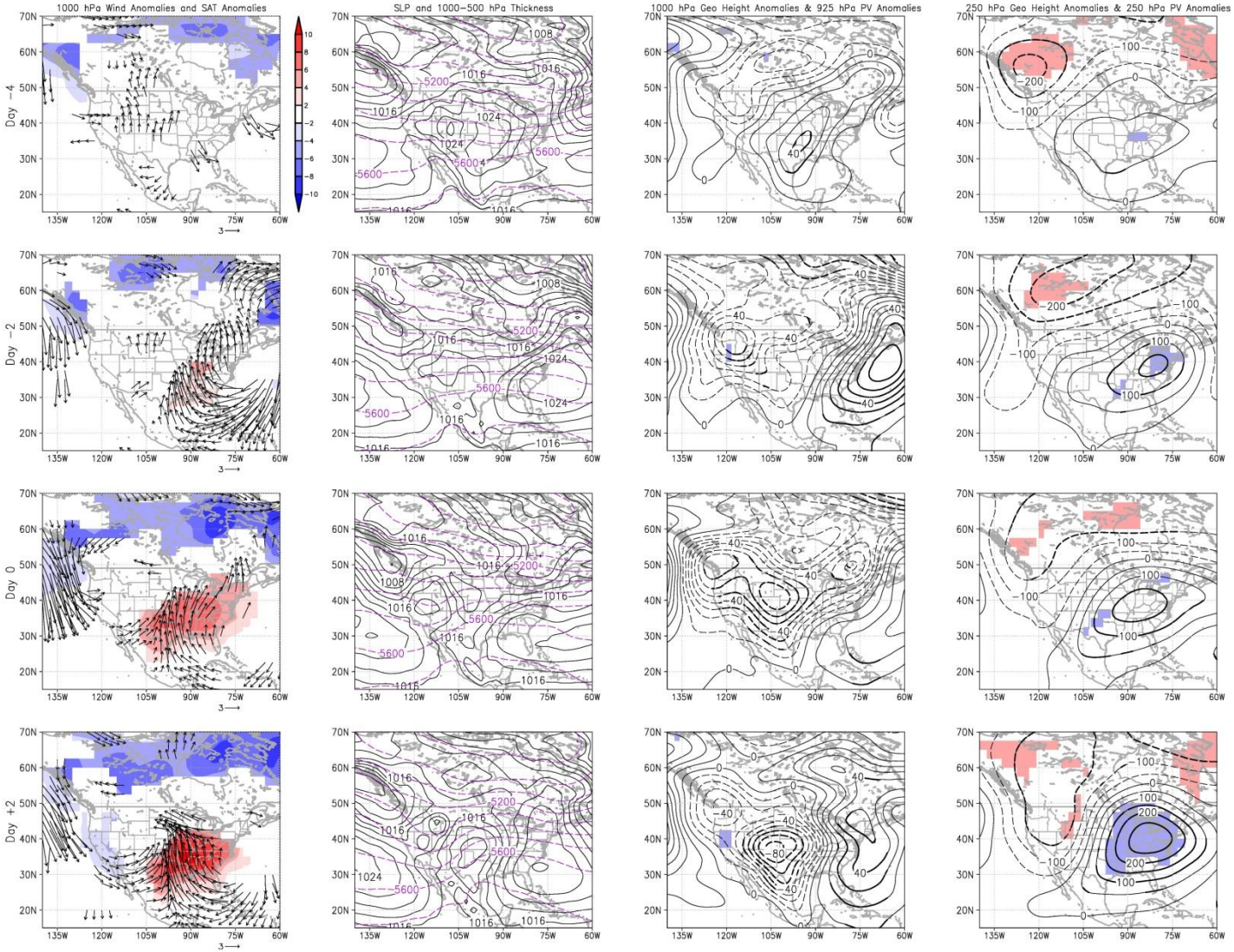

Figure 4.6: Same as Figure 4.1, except for Days -4, -2, 0 and +2 for Case 4 – SE WWs, Negative PNA.

4.3.4. Case 4 – SE WWs: Negative PNA

The evolution of Case 4 is quite different from the previous WW case just considered. In Case 4, the warm anomaly forms more abruptly around the time of event onset. Unlike the previous case, at Day -4, no significant warm anomaly features are observed (Fig. 4.6, column 1), nor are there any statistically significant southerly winds in the region of interest. By Day -2, very weak warm anomalies begin to emerge over the SE, in association with a robust anomalous anticyclonic circulation that forms along the middle Atlantic coast. This circulation promotes warm advection over a broad region encompassing the SE US. By Day 0, the warm pattern has expanded to now include the southeast, northeast and south-central US, and has intensified in strength. Meanwhile, the eastern edge of an emerging anomalous cyclonic circulation is now observed in the wind anomaly field over the Midwest. The east-west dipole pattern across the US is highly reminiscent of the surface manifestation of the PNA (Wallace and Gutzler 1981). This feature is not surprising given the prescribed sign of the PNA used in creating the composites. As will be discussed in relation to Fig. 4.4B (right column), the PNA signature is visible in the upper tropospheric geopotential height field at least 4 days prior to WW onset. This feature was not present in Case 3, and highlights a fundamental difference between the two categories of WW cases. By Day +2, the warm SAT anomalies reach their maximum amplitude, as southerly winds between the anticyclone-cyclone couplet continue to advect warm air into the region. Another interesting feature present in the composite at Day +2 is the distinct front/dryline over the south-central US. Such frontal-type features are evident in several of the near-surface fields presented in

Fig. 4.6, illustrating one of the benefits of using four-times daily data. By Day +4 (not shown), the warm anomaly begins to weaken and retract in areal extent.

The role of the warm advection and its connection to several prominent synoptic features are confirmed in column 2 of Fig. 4.6. Several days prior to onset (Day -4), there is a region of relatively high surface pressure located over the central US which, if anything, is associated with cold advection over the SE US. However, by Day -2, this area of high pressure has migrated eastward and becomes centered just off the SE coast, leading to warm advection over the SE region consistent with the anomalous wind field (column 1). The anticyclone weakens slightly by the time of onset (Day 0), while surface pressure falls are observed east of the US Rockies. These lower pressures are associated with the cyclonic circulation signature noted earlier in the wind anomaly field. By Day +2, the anticyclone strengthens once again and expands northward, leading to concentrated warm advection over the SE region. In addition, a closed low pressure center emerges over the central US. The counterclockwise circulation associated with this feature contributes to the southerly winds and warm advection over the SE region. The frontal feature is also evident as a trough trailing southward from the center of the low pressure system. By Day +4 (not shown) both of the pressure systems have weakened in magnitude and migrated such that the southerly flow over the SE region is reduced, ultimately leading to event demise.

These near-surface synoptic features are also evident in the 1000 hPa geopotential height anomaly field (Fig. 4.6, column 3), with positive (negative) height anomalies corresponding to the regions of high (low) pressure. However, the degree of similarity between the SLP and 1000 hPa height anomaly fields appears to be less for this case

compared to the previous 3 composites, particularly over the western US. This is due to mismatches in the regional patterns of the climatological and anomalous height/pressure fields. Like Case 3, no significant PV anomaly structures are observed at 925 hPa. Thus, Cases 3 and 4 do not exhibit lower-tropospheric PV anomalies that are opposite in sign to those at higher levels. Further, although there is a significant warm SAT anomaly pattern that likely provides a cyclonic circulation by acting as an effective PV anomaly, its influence is less evident in the net surface wind anomaly pattern in this case.

In the upper troposphere, we observe a persistent (strengthening) quasi-stationary trough (ridge) anomaly feature over northwest (southeast) North America (Fig. 4.6, column 4). This pattern and its temporal evolution are qualitatively similar to Case 3, but the centers of action in the current case are on average (a) stronger and (b) less mobile (more geographically fixed). At Day -4, a significant trough feature is observed over western Canada. By Day -2, the trough anomaly has strengthened and extended northeastward, resulting in a southwest to northeast horizontal "tilt" in the anomaly structure. Such a structure is favorable for southward dispersion of Rossby wave energy toward the continental US (e.g., Hoskins et al. 1983). This tilted structure is maintained through Day 0 and during this time the ridge anomaly over the eastern US intensifies, consistent with expectations of Rossby wave theory. By Day +2, the large-scale wave pattern has become more amplified as the ridge over the eastern US strengthens. However the upstream trough has altered in structure with more of a north-south anomaly "tilt". Thereafter (not shown), the overall flow pattern continues, but the ridge amplitude weakens as the trough structure is less favorable for southward energy dispersion. The 250 hPa composite PV anomaly evolution parallels the height anomaly evolution, with

positive (negative) PV anomalies located over Western Canada (Eastern US). Like Case 3, the configuration of these upper level PV anomaly features leads to an associated circulation anomaly pattern that is consistent with the observed anomalous southerly flow over the central US. However, in contrast to Case 3, the anomalies are quasi-stationary during the evolution and there seems to be a pulsing of energy through the quasi-stationary wave pattern (with the downstream center strengthening at the expense of the upstream center). These characteristics suggest a prominent role for a quasi-stationary wave-train feature in Case 4 WW onset. To further investigate the role of a stationary wave-train feature, we have studied the 250 hPa geopotential height anomaly field over an expanded domain that includes much of the North Pacific Ocean (Fig. 4.4B, right column). There is, in fact, a statistically significant east-west wave-train anomaly structure (of alternating sign) emanating from near the Aleutian Islands and arching northeastward into Canada and then southeastward into the eastern US, consistent with the negative PNA pattern. We additionally note that the evolution shows that the downstream ridge anomaly strengthens after the formation of significant anomaly centers upstream, consistent with Rossby wave energy dispersion through a quasi-stationary wave-train. This quasi-stationary structure is distinct from the more transient and mobile feature observed in Case 3, and is evident by the comparison provided in Figure 4.4B. Interestingly, in contrast to Case 2 where the negative NAO interacts with a synoptic-scale disturbance, Case 4 does not include a synoptic disturbance that interacts with the negative PNA. This observation is consistent with prior studies that have found that the NAO is governed by nonlinear dynamics, whereas the PNA is primarily driven by linear dynamics (Feldstein 2002, Feldstein 2003, Evans and Black 2003).

The PV anomaly cross-sections for Case 4 (Fig. 4.2, column 4) mainly reflect the structure associated with the ridge anomaly over the eastern US, as the western trough anomaly is largely confined to higher latitudes. Similar to Case 3, the primary signatures of note are located at 500 hPa and above. Generally, we find that the most prominent PV anomalies are found in the mid to upper troposphere, with the largest anomalies located near the tropopause. The initially amorphous upper-level negative PV anomaly signature (related to the eastern ridge) coalesces and strengthens during WW onset. The relatively stationary nature of the upper-level PV anomalies that was identified in the horizontal maps of Fig. 4.6 is also evident in the vertical profiles, as the negative upper-level anomalies remain centered between 80°W - 90°W. In this case, however, we do observe a significant near-surface negative PV anomaly feature over the western US that extends up to about 775 hPa. However, this feature does not appear to play a role in WW onset. In addition, like in Case 3, the role of the surface temperature anomaly in contributing to the surface wind field isn't as clear as it was in the CAO cases.

4.3.5. Specifics of the Role of Low Frequency Modes

The specific role of low frequency modes in ETR evolution is interesting and includes some unexpected aspects. In particular, in Case 2 the NAO contributes to both SE CAO onset as well as event demise. This result is somewhat counterintuitive as the low frequency forcing ends up limiting the event time scale (even though the low frequency mode, itself, persists). However, as described above, even with the time scale limitation, the CAO events that occur in association with the NAO still have a longer duration than if the NAO were in its neutral phase. A prominent role for low frequency

modes is also indicated for Case 4, in which case the PNA teleconnection pattern helps to establish the essential North American circulation centers. Thus, our results indicate that low frequency modes serve to both favor ETR formation (Cases 2 and 4) as well as modulate the event duration (Case 2). Further, these results seem to imply that the presence of a low frequency mode is not a sufficient condition for ETR development given the role of synoptic events in each of the low frequency mode cases (Case 2 and 4).

To further support the idea that low frequency modes favor ETR formation as opposed to directly triggering ETR events, we have analyzed the temporal evolution of the normalized daily NAO and PNA indices during ETR onset. The corresponding figures for Cases 2 and 4 are shown in Figures 4.7A and 4.7B, respectively. For Case 2, the normalized daily NAO index remains below a value of -1 from approximately Day -5 to Day +1. Given that strongly negative NAO conditions *precede* CAO onset, the NAO seems to provide a favorable environment for CAOs to occur. After Day -1, the NAO index increases monotonically suggesting a decreasing role for the NAO over time. Therefore, there is not a one-to-one causal relationship between the NAO and CAOs (i.e. low frequency modes don't directly *trigger* ETR events). The time lag also makes physical sense given the proximity of the North Atlantic to the region of interest. In comparison, the result for Case 4 indicates a slightly different behavior for the role of the PNA pattern in WW onset. While the normalized daily PNA index approaches a value of -1 in the days prior to onset, it continues to decrease throughout the period encompassing onset. Thus, the PNA pattern initially seems to provide a favorable environment for WW onset. However, the continued decrease in the normalized daily PNA index after onset has two possible implications: (1) the strengthening of the negative PNA pattern

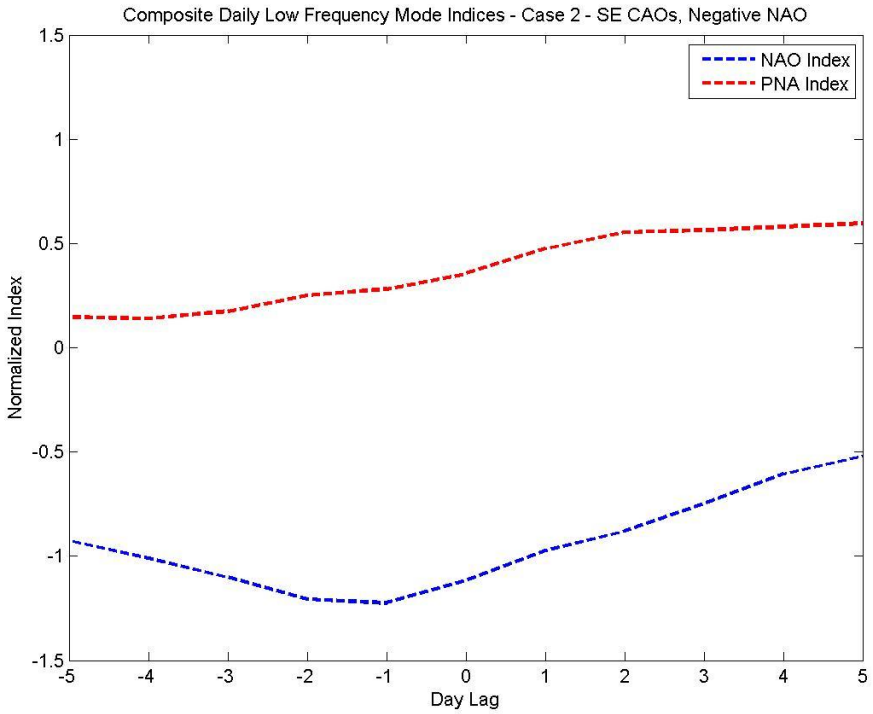

Figure 4.7A: Daily Composited NAO and PNA Normalized Indices for Case 2.

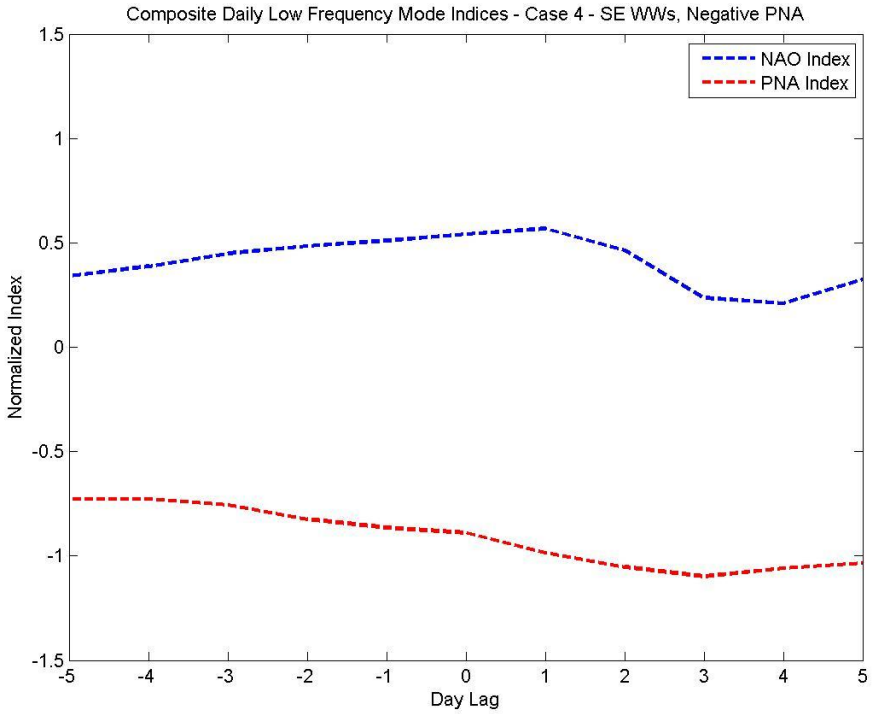

Figure 4.7B: Daily Composited NAO and PNA Normalized Indices for Case 4.

contributes to amplification of the WW event, or (2) the formation of the WW event initialized by the PNA pattern helps to strengthen the PNA in a self-sustaining manner. In any case, we can conclude that the NAO and PNA patterns *provide favorable environments for* ETRs as opposed to directly triggering onset.

Subsequently, by providing favorable environments for ETRs, the events associated with low frequency modes should be able to grow more rapidly in association with their dynamical triggers (which in our analyses are usually synoptic weather events). This is confirmed in our research results, which seem to indicate that the ETRs associated with the negative NAO and PNA grow more rapidly.

4.4 Summary & Conclusions

Our study identifies the main synoptic and dynamic signatures associated with different categories of ETR onset over the southeast (SE) US with an emphasis on delineating the role of large-scale low frequency modes. This is approached via composite time evolution analyses of several different field variables for four different ETR categories (two CAO and two WW categories) based upon the concurrent sign and amplitude of relevant low frequency modes. Our composite analyses reveal significant roles for both synoptic and large-scale disturbances during CAO and WW onset over the SE. Each of the four categories of events involves transient synoptic features, a low frequency mode influence or a juxtaposition of the two. To summarize the main features identified:

- **Case 1 (SE CAOs - Neutral NAO)**: CAOs of this type are linked to a transient high pressure system propagating southeastward from Canada followed by synoptic-scale cyclogenesis over eastern Canada.
- **Case 2 (SE CAOs - Negative NAO)**: Although CAOs of this type are also associated with a mobile high pressure system from the west, it is also linked to a large-scale quasi-stationary low pressure system over the eastern US which represents part of the southern manifestation of the NAO pattern. Thus, the NAO pattern plays a direct role in establishing the regional circulation pattern leading to the CAO.
- **Case 3 (SE WWs - Neutral PNA)**: WWs of this type are initially (subsequently) associated with anomalous low (high) pressure near the Pacific Northwest (SE) coast. Both of these features are transient and exhibit eastward propagation.
- **Case 4 (SE WWs - Negative PNA)**: Although WWs of this type are also associated with anomalous low (high) pressure to the northwest (east), these features are nearly quasi-stationary and represent the downstream centers of the negative phase of the PNA pattern. Thus, these events have dynamical roots in the extratropical North Pacific.

Thus our results provide a qualitative indication of the role of low frequency modes in ETR onset via their impact on regional circulation and temperature advection.

The composite circulation anomaly patterns observed preceding and during ETR onset generally consist of either negative (CAOs) or positive (WWs) geopotential height

anomalies in the upper troposphere near the region of interest (SE) with oppositely-signed anomalies located in the lower troposphere west of the region of interest (over the central US). In some of the cases, an east-west dipole pattern is present at the surface, resulting in enhanced northerly or southerly flow. In any case, the anomalous circulation patterns act to promote cold (CAO) or warm (WW) advection into the region of interest, ultimately forming the cold or warm SAT anomalies that define the extreme events. The primary differences among these cases lie in the origin and nature of the circulation anomaly features linked to ETR onset. These results generally confirm aspects of prior CAO studies (e.g. Konrad 1996, Konrad 1998, Konrad and Colucci 1989, Colle and Mass 1995) while providing distinctly new results on the synoptic behavior of WW development and establishing the synoptic role of low frequency modes in both CAO and WW onset.

Our composite PV anomaly analysis provides additional information regarding coherent dynamical features associated with ETR onset. The composite PV anomaly structure is generally characterized by prominent PV anomaly patterns in the mid to upper troposphere consistent with the coincident geopotential height anomaly patterns (i.e., anomalous ridge features are linked to negative PV anomalies while anomalous troughs are related to regions of above normal PV). The largest PV anomaly amplitudes are found in the upper troposphere with weaker anomalies in the lower atmosphere nearest the surface. The weakest anomalies are located in the mid-troposphere. These upper tropospheric PV anomaly patterns have horizontal structures that would be associated with southerly (northerly) winds over the central and eastern US during WW

(CAO) onset. In some cases, these induced flow patterns are supplemented with contributions from upstream PV anomaly features of opposite sign.

Interestingly, the primary PV structures evolve similarly in the mode cases and neutral cases (for both WWs and CAOs). Given that the responsible local circulation features for CAO and WW development in the mode cases and neutral cases are similar (whether they are transient, quasi-stationary or a combination of both), it shouldn't be surprising that the PV signatures are very similar. For instance, in the CAO cases, Case 1 is associated with a transient cyclone-anticyclone couplet while Case 2 is associated with a quasi-stationary couplet that is locally enhanced by a transient circulation feature. Even though the time scales of these features are different, the instantaneous associated cyclone-anticyclone couplets are located in the same regions and are characterized by similar PV signatures. Comparatively, even though the PV anomaly amplitudes near the surface are smaller in magnitude and area than those in the upper troposphere, their closer proximity to the surface, where the key meridional air temperature transport occurs, gives them the potential to provide a fundamental contribution to ETR onset. In addition to the near-surface PV anomalies, it is likely that a portion of the surface wind field arises from the SAT anomalies themselves acting as effective PV anomalies.

The specific role of low frequency modes in ETR evolution is interesting and includes some unexpected aspects. Specifically, our results indicate that low frequency modes serve to both favor ETR formation (Cases 2 and 4) as well as modulate the event duration (Case 2). Nevertheless, in principle, such links to low frequency modes suggest some potential for longer-term predictability of ETR events. For instance, a recent study by Scaife et al. (2014) demonstrated that aspects of the NAO behavior can be predicted

months in advance. Because the NAO strongly modulates winter weather over North America and Europe, the predictability of the NAO may ultimately lead to increased skill in predicting regional winter climate behavior (Scaife et al. 2014). However, advances in predicting specific ETR episodes (or their likelihood) will be predicated on first obtaining a more complete mechanistic understanding of the physical linkages between NAO events and ETR life cycles. Such knowledge would help in moderating or reducing the risk of ETR-related impacts on society.

This research has also provided some insight to the general behavior and development of CAOs and WWs. One distinction between these two classes of events is that CAOs appear to be related to substantial air mass transport (normally from Canadian latitudes) while WW formation occurs more locally over the region of interest (with air mass emanating from the adjacent Gulf of Mexico or North Atlantic). This behavior is indicated in our composite wind analyses (column 1) as during CAOs the strong northerlies are typically observed at the leading edge of the cold air mass (Figs. 1 and 3), while during WWs strong southerlies spatially coincide with the developing warm air mass (Figs. 5 and 6). In addition, CAO cold air masses form in high latitudes and move southward at least 20° of latitude, while WW warm air masses form in more southerly latitudes but typically only traverse 5° latitude or less.

Although the current research provides an important synoptic-dynamic characterization of ETR formation, additional dynamically-based diagnostic research will be required to obtain a more complete mechanistic understanding of ETR life cycles including the specific role of low frequency modes. Our follow up research efforts will include regional heat budget, wave activity and potential vorticity inversion diagnoses.

The thermodynamic budget will provide quantitative insight into the relative importance of temperature advection, adiabatic and diabatic processes in ETR formation, while the wave activity flux analyses will help clarify the role of low frequency modes for different ETR categories. Under the assumption that horizontal temperature advection plays a leading role in ETR onset, the PV inversion analyses can be used to directly assess which of the dynamical features identified in the current study directly contribute to local temperature changes that occur. For example, this will allow us to directly assess the respective roles of the upstream anticyclone and downstream cyclone during CAO onset (e.g. Konrad 1998). Such additional knowledge of ETR physics is essential for optimizing the simulation of ETR events in both weather forecasts and climate simulations.

CHAPTER 5

PHYSICAL AND DYNAMICAL MECHANISMS

The work presented in this chapter is in preparation for journal submission.

5.1 Background & Motivation

The goal of this research is to identify the primary mechanism(s) leading to ETR development. Extensive diagnostic analyses are conducted to determine the thermodynamic and dynamic processes and physical mechanisms producing the onset of ETRs. Although the research I have presented thus far provides important information on the trends and variability of ETRs (Chapter 3) and the synoptic-dynamic behavior of ETR formation (Chapter 4), it does not quantify the specific processes responsible for ETR development. Because they are based on fundamental dynamical and thermodynamical principles, the analyses presented in the current chapter provide a strong quantitative basis for identifying the primary processes and mechanisms responsible for ETR development. Further, they will dynamically clarify the role of low frequency modes in ETR development implicated in the previous chapter.

The scientific understanding of which processes determine the evolution of ETRs and the physical mechanisms that are responsible for their development is incomplete. In this study, we will focus on determining the sources for the development of ETRs. Further, we will examine in more detail how the characteristic synoptic features described in the previous chapter are related to dynamical processes that occur during ETR onset. Given the potential for eventual changes in ETR behavior related to global warming (e.g., Yu et al. 2015) it is very important to isolate the underlying dynamical

and physical processes responsible for ETRs to ensure the reliable simulation and prediction of ETRs in global models.

Heat budget analyses will first be used to provide information on the thermodynamic processes occurring in ETRs. Heat budget analyses for CAOs occurring over the eastern US and related synoptic features have been conducted in both case studies (Konrad and Colucci 1989, Colucci et al. 1999, Colle and Mass 1995, Tanaka and Milkovich 1990, Tan and Curry 1993) and composite analyses (Portis et al. 2006, Turner and Gyakum 2011) using observations as well as model data. Konrad and Colucci (1989) found that the timing of the observed CAO events and their interaction with other features (such as cyclogenesis either before or after CAO onset) are important in determining the spatial characteristics and relative contributions of the cold air advection and adiabatic warming. However, in most cases, cold air advection is partly counteracted by adiabatic warming. A second observational study found that horizontal cold advection is a key player in CAO development, and that it is stronger than the adiabatic warming effects over the eastern US (Colle and Mass 1995). In contrast, a modeled CAO case study by Colucci et al. (1999) found that there is a subtle balance between diabatic and adiabatic processes in CAO formation. Further, Portis et al. (2006) find that there are regional differences in the relative roles of the dynamic and thermodynamic processes during CAO events.

It is evident from the discussion above that there is not a scientific consensus yet on the relative importance of the various mechanisms contributing to CAO development. Further, none of these studies address the mechanisms contributing to WW development. Some of the differences in the aforementioned studies may be attributed to whether it was

a case study or composite study, employed model data or observations, region definitions, areal averaging (such as in Portis et al. 2006), and the terms in the thermodynamic equation that were considered. Several of the studies neglected diabatic effects completely or considered them in combination with the adiabatic effects (Konrad and Colucci 1989, Colle and Mass 1995).

The near-surface heat budgets used in this study will quantify the thermodynamic contributions to ETR onset, and will allow us to determine to what extent the temperature anomalies observed in the composite analyses are generated locally or advected from other regions. Further, it will allow us to assess the relative importance of the advective, adiabatic, and diabatic processes in ETR onset. The benefits of this particular study over prior analyses is that (a) no areal-averaging is performed, (b) the nonlinear temperature advection, adiabatic and diabatic terms are explicitly quantified (unlike previous studies where these terms were often ignored), and (c) data with higher spatial and temporal resolution is used.

The dynamical features associated with ETR onset are examined using potential vorticity (PV) inversion analyses. A potential vorticity (PV) framework is a simple and effective way to study large-scale dynamical processes (Hoskins et al. 1985). The invertibility principle and PV conservation imply that a complete description of the flow can be obtained using the three-dimensional PV distribution (Black and Dole 1993). For large-scale motions such as those of interest in this study, quasi-geostrophy provides a highly accurate description of PV dynamics, thus QG PV inversion is used in this analysis. The strength of QG PV inversion is its simplicity, and it has the advantage of being linear which makes it computationally inexpensive to solve (Davis 1992). The

linearity also allows for an unambiguous one-to-one association between each PV "piece" and its associated circulation anomaly feature. PV inversions have been used to clarify the dynamical mechanisms for other types of weather events, including persistent flow anomalies (Black and Dole 1993), stratospheric NAM events (Black and McDaniel 2004), cyclogenesis (Davis and Emanuel 1991), and weather regime transitions (Evans and Black 2003). PV inversions are used in this study to help clarify the dynamical mechanisms involved in ETR development by isolating the tropospheric PV anomalies responsible for key lower level circulation features. Information on the dynamical mechanisms behind ETR formation and their link to the role of low frequency modes is incomplete in the current literature. A primary objective of the thesis is to close these gaps in our scientific understanding of ETRs.

5.2 Data & Methods

Dynamic and thermodynamic diagnostic analyses are presented in this chapter. Guided by the composite synoptic analyses from the previous chapter, near-surface heat budgets and piecewise QGPV inversions are performed. As will be explicitly illustrated in section 5.2.2, the QG framework provides an excellent quantitative representation of the synoptic features of interest. The input observational data is the same as that employed earlier.

5.2.1 Heat Budget Analyses

To obtain quantitative estimates of the processes producing the observed temperature anomalies in Figures 4.1, 4.3, 4.5 and 4.6, the isobaric thermodynamic

equation is evaluated over the onset period of ETRs. This type of analysis can help distinguish whether a temperature anomaly is generated locally (by diabatic or adiabatic processes) or is due to horizontal transport (Turner and Gyakum 2011). A field decomposition into climatological-mean and anomaly components also allows for an assessment of eddy-mean flow interaction. Composite-mean time averages for each term in the isobaric thermodynamic equation were assessed for the period of ETR onset from Day -4 to +2. This time period corresponds to the most rapid development period for most ETR events, and, for ease of comparison, is chosen to be the same for each ETR category considered. Equation (1) shows the composite temperature anomaly tendency used in this analysis:

$$\frac{\partial\langle T'\rangle}{\partial t} = -\langle \mathbf{V}'\rangle \cdot \nabla\bar{T} - \bar{\boldsymbol{V}} \cdot \nabla\langle T'\rangle - (\langle \boldsymbol{V}' \cdot \nabla T' - \overline{\boldsymbol{V}' \cdot \nabla T'}\rangle) + S_p\langle\omega'\rangle + \langle\frac{\dot{Q}'}{C_p}\rangle \qquad (5.1)$$

In (5.1) the overbar represents a climatological-mean (DJF-mean) value and the primes denote local deviations from the climatological-mean. The angle brackets indicate a composite average over all the ETR events in that category (see Tables 4.1 and 4.2 for the events included in each category). The quantity $S_p$represents the static stability parameter in pressure coordinates and is defined as $S_p = \frac{\sigma p}{R}$, where σ is the standard atmosphere static stability parameter, p is pressure level and R is the gas constant for dry air. Further, we assume that $\sigma = 2.5x10^{-6}\frac{m^2}{Pa^2s^2}$ (Holton, 2004) since this value does not vary appreciably between the mid- and lower-troposphere in the midlatitudes. The first two terms on the right hand side of (5.1) are linear with respect to the composite anomaly

field, and represent advection of the climatological-mean temperature by the composite wind anomalies and the advection of the composite temperature anomalies by the climatological-mean wind, respectively. Unlike the first two terms, the terms within parentheses are nonlinear and represent the anomalous nonlinear eddy temperature advection. Together, these two terms represent the net contribution of anomalous horizontal temperature advection to the composite temperature tendencies. The final two terms on the right hand side of (5.1) are the contributions to temperature tendencies resulting from anomalous adiabatic expansion/contraction and diabatic processes, respectively. The latter diabatic term is obtained as a residual by calculating the difference between the observed temperature tendencies and the sum of the four remaining terms on the right hand side of (1). This budget framework parallels that employed in Dole and Black's study of persistent flow anomalies (1990). The temperature anomaly tendencies on the left side of (5.1) are calculated using finite differences between the endpoints. Results are shown for the 925 hPa level, a near-surface layer, where key thermodynamic processes responsible for ETRs occur.

5.2.2 PV and PV Inversion Analyses

In the previous chapter, regions of anomalous PV that might contribute to ETR events were identified via a synoptic analysis of the PV anomaly time evolution (Figure 4.2). In a similar manner, composite PV anomalies were calculated over the same time period used for the heat budget analyses (Days -4 to +2) to help identify regions of high PV that might be responsible for the ETR events. Horizontal maps of the period-average PV anomalies at 925 hPa, 500 hPa and 250 hPa are constructed in addition to vertical

profiles of the period-average anomalies from 925 hPa up to 100 hPa. Next, piecewise QGPV inversions are performed to determine the individual contributions of distinct PV anomaly features to the near surface horizontal circulation anomalies occurring during ETR onset. As discussed earlier, given a PV distribution, the associated wind, pressure and temperature fields can be deduced (Hoskins et al. 1985). Therefore, any subset (or "piece") of the PV anomaly field can be inverted to identify its contribution to both local and remote circulation anomalies (Black and McDaniel 2004).

Specifically, piecewise PV inversion is the process of inverting a specified subset of the 3-D PV anomaly field. However, in order to perform the PV inversion, three specifications must be made (as described by Hoskins et al. 1985): (1) specify a balance condition (here, we assume quasigeostrophic balance and we show later in the results section that this assumption is valid), (2) specify a reference state (here, we use a DJF-climatology), and (3) solve the inversion over a suitable spatial domain with proper attention to boundary conditions (we select the Northern Hemisphere). Inputs to the PV inversion routine are geopotential height anomalies and climatological-mean (DJF) geopotential height. In the following analysis, we assume that the climatological-mean flow is a balanced reference state. Our ultimate objective is to use piecewise PV inversion to determine the near-surface (925 hPa) wind anomalies that are induced by various PV anomaly features throughout the troposphere. Thus, the output geopotential height anomaly field from the inversion process is used to subsequently calculate the corresponding wind anomaly field using geostrophic balance. The balance condition that relates q' and Z' for quasigeostrophic flow on a sphere (which is a modified form of the q' equation from Black (2002) using the relationship $Z=\Phi/g_0$) is given by:

$$q' = \mathrm{g}\left[\frac{1}{f(a\cos\phi)^2}\frac{\partial^2 Z'}{\partial\lambda^2} + \frac{\tan\phi}{a^2}\frac{\partial}{\partial\phi}\left(\frac{\cot\phi}{f}\frac{\partial \mathrm{Z}'}{\partial\phi}\right) + f\frac{\partial}{\partial p}\left(\frac{1}{\sigma}\frac{\partial Z'}{\partial p}\right)\right] \quad (5.2)$$

In (5.2), q is the quasigeostrophic potential vorticity, *f* is the Coriolis parameter, g is the gravitational constant, Z is the geopotential height and σ is the static stability parameter. The geostrophic winds are subsequently calculated from the geopotential height anomalies via the geostrophic wind equations (5.3a,b):

$$u_g' = -\frac{g}{f}\frac{\partial Z'}{\partial y} \quad (5.3a)$$

$$v_g' = \frac{g}{f}\frac{\partial Z'}{\partial x} \quad (5.3b)$$

As will be demonstrated, the geostrophic winds provide a quantitatively accurate approximation to the actual composite wind field for the cases considered here. The PV inversion code was originally developed by Chris Davis and was subsequently modified at Georgia Tech (and graciously provided by) Jason Furtado.

We first examine how each individual layer of PV anomalies from 1000 hPa to 100 hPa contributes to the surface wind field (925 hPa), focusing on the lower- and upper-troposphere where prominent PV anomalies were identified in Chapter 4. Consistent with the prior analyses, the lower- and upper-troposphere exhibited the largest contribution to the near-surface (925 hPa) winds. Based on these results, we divide the atmosphere up into three layers (or vertical partitions), lower-, mid- and upper-troposphere (1000-850 hPa, 700-500 hPa, and 400-100 hPa). These layers were chosen since each level contained in these layers contributes in a similar manner to the near-surface flow. Then, we separately invert the PV anomalies within each layer to determine

the respective contribution to the near surface circulation. For Case 2, we also horizontally partition the PV anomaly field to isolate the role of the NAO in CAO development. The specific details of the horizontal partitioning are included in the results section.

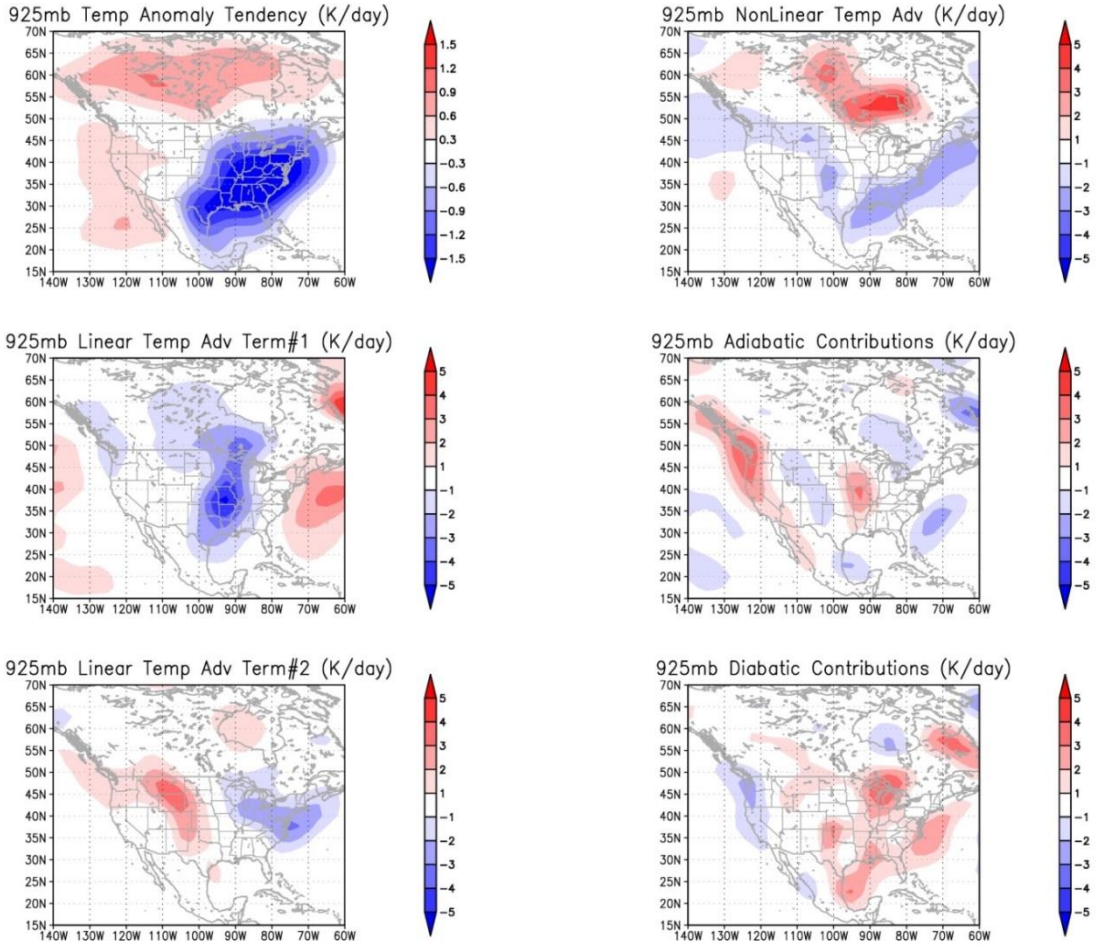

Figure 5.1: Composite thermodynamic heat budget analyses for days −4 to +2 for Case 1 – SE CAOs, Neutral NAO at 925 hPa. Quantities shown (K/day) are the temperature anomaly tendency (top left), the linear advection of the climatological-mean temperatures by the composite wind anomalies (middle left), the linear advection of the composite temperature anomalies by the climatological-mean winds (bottom left), the nonlinear temperature advection by eddies (top right), the anomalous adiabatic cooling (middle right) and anomalous diabatic heating (bottom right). Red (blue) shading indicates a positive (negative) contribution.

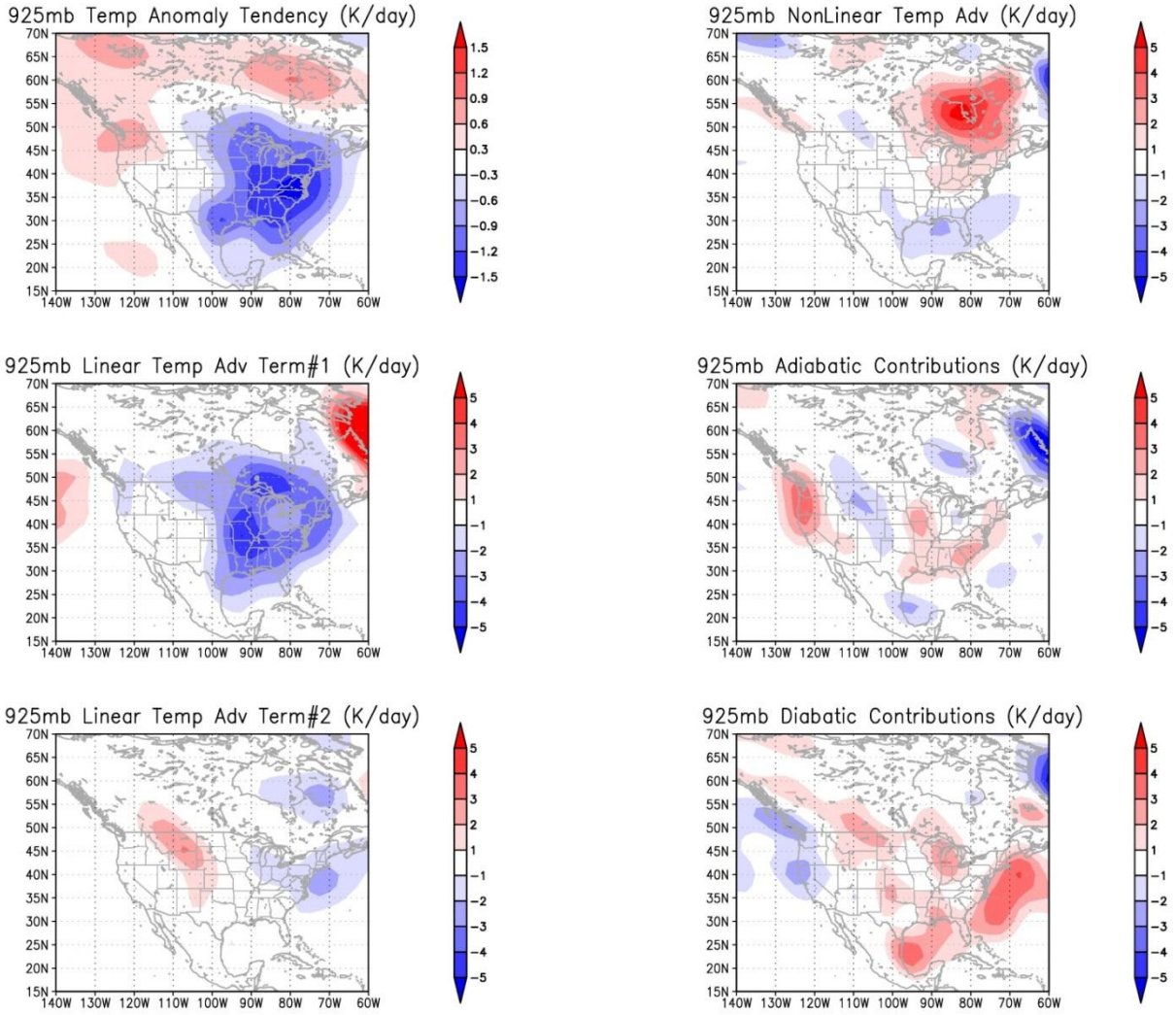

Figure 5.2: Same as Figure 5.1, except for Case 2 – SE CAOs, Negative NAO.

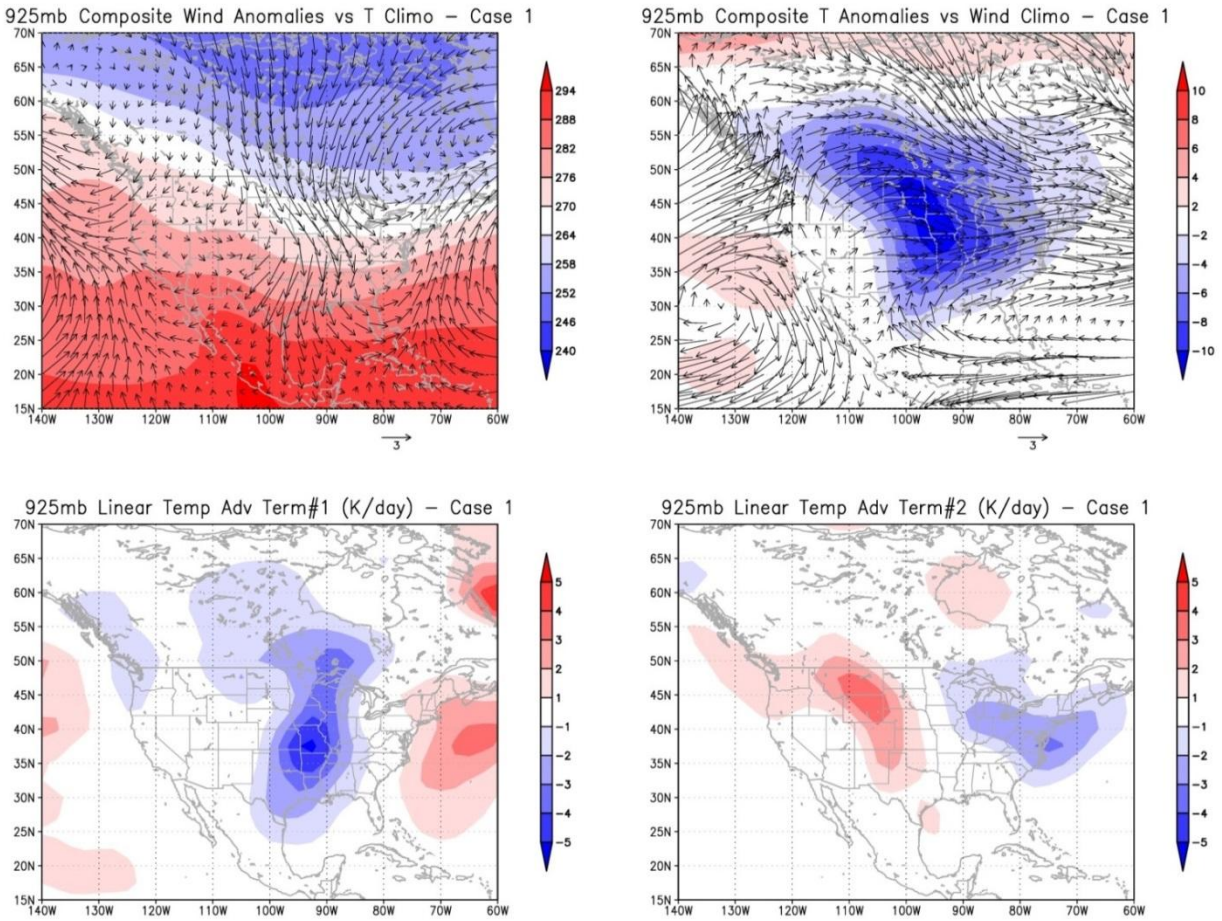

Figure 5.3: Composite linear decomposition analysis for for days −4 to +2 for Case 1 – SE CAOs, Neutral NAO at 925 hPa. The fields shown are the climatological-mean temperatures (K) with the composite wind anomalies (m/s) (top left), the corresponding the linear advection of the climatological-mean temperatures by the composite wind anomalies (m/s) (bottom left), the composite temperature anomalies (K) with the climatological-mean winds (top right), and the corresponding linear advection of the composite temperature anomalies by the climatological-mean winds (K/day) (bottom right).

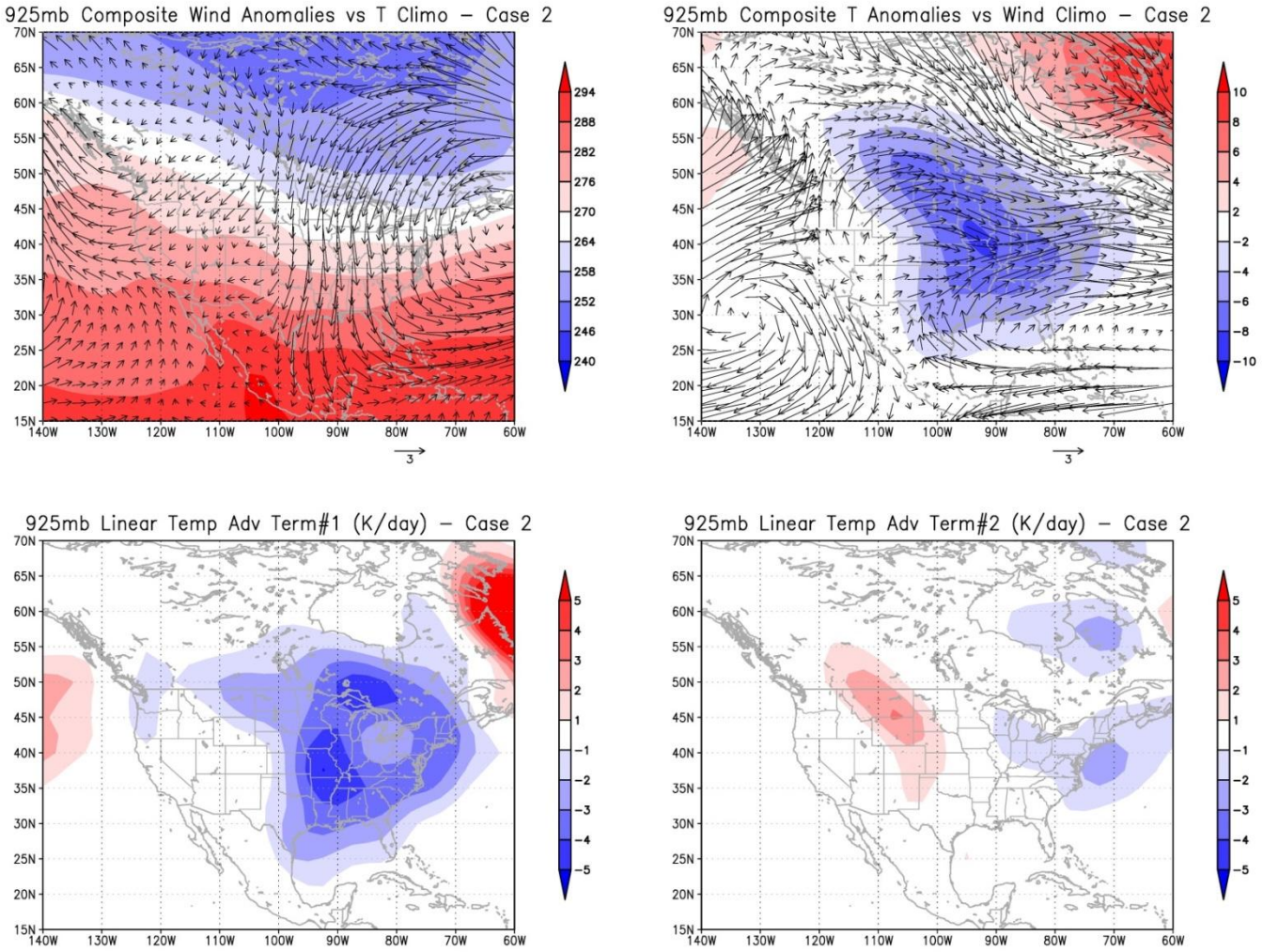

Figure 5.4: Same as Figure 5.3, except for Case 2 – SE CAOs, Negative NAO.

5.3 Results & Discussion

5.3.1 Heat Budget Analyses

Each term in the heat budget equation evaluated for Case 1 is displayed in Figure 5.1. The temperature anomaly tendency term (Figure 5.1, top left panel) is negative over the entire eastern half of the US, which includes the SE region where our events are defined. On the other hand, this term is positive over much of Canada and the far Western US. The positive values in Canada are consistent with the idea that this is where the cold air originates from and subsequently moves out of into the central and eastern US. The linear temperature advection terms (Figure 5.1, middle and bottom left panel) collectively provide cold advection over the eastern half of the continental US during this time period. The strongest signature is located over the central US, the region through which the cold SAT anomalies traverse during the lifecycle of these events. By comparing the two linear advection terms, it is evident that Term #1 (the advection of the climatological-mean temperatures by the composite wind anomalies) accounts for most of the cold advection over the central US while Term #2 (the advection of the composite temperature anomalies by the climatological-mean wind) provides a substantial contribution over the mid-Atlantic region. Except for modest cold advection over the Deep South, the nonlinear advection term is relatively weak over the continental US (Figure 5.1, top right panel). A relatively strong nonlinear warming signature is observed near the southern tip of the Hudson Bay in Canada. Given the prominence of the linear advective terms over the US, we conclude that the composite anomaly fields capture the primary features of interest contributing to ETR onset. The adiabatic term (Figure 5.1, middle right panel) is generally weak in amplitude across most of the continental US. The strongest region of

adiabatic warming lies along the Northwest and West Coast of the US, with a region of relatively strong adiabatic warming occurring over the central US, collocated with the region of linear temperature advection (Term #1). This is consistent with theoretical expectations of QG theory as cold advection is expected to induce subsidence and adiabatic warming (e.g., Holton 1984), partially offsetting the local cooling tendency. The southward air mass migration also brings the cold air mass into contact with warmer land surfaces leading to local heating, as is indicated by the residual diabatic heating term (Figure 5.1, bottom right panel) which is positive over the eastern half of the US, especially just off the East Coast. The observed diabatic heating pattern is physically very consistent with the presence of the Gulf Stream in those locations.

A corresponding analysis for Case 2 is shown in Figure 5.2. There is a high degree of similarity between these two cases, albeit with a few minor differences. Like in Case 1, the temperature anomaly tendency term (Figure 5.2, top left panel) is negative over the entire eastern half of the US, including over the SE region. Interestingly, the temperature anomaly tendency appears to be a bit stronger in Case 1 than Case 2. This is likely related to two things: (1) the temperature anomalies in Case 1 are slightly stronger over a larger area (Chapter 4, Figures 4.1 and 4.3), implying that the anomalies are larger in magnitude, and (2) the rapidity and location of the cold air outbreak. Nonetheless, the sign and location of the temperature tendencies are qualitatively very similar. Also similar to the previous case, there is concomitant warming over Canada and parts of the far Western US, where the cold air originates. The linear temperature advection terms (Figure 5.2, middle and bottom left panel) both indicate cold advection over the eastern US during this time period. Like the previous case, the strongest signature is over the

central US, and it is evident that Term #1 (the advection of the climatological-mean temperatures by the composite wind anomalies) accounts for the vast majority of the cold advection occurring. The linear advection Term #2 (the advection of the composite temperature anomalies by the climatological-mean winds) is smaller in magnitude in Case 2 than in Case 1. Over most of the continental US, the nonlinear advection term is quite weak (Figure 5.2, top right panel). Only over the southern tip of the Hudson Bay in Canada is there a relatively strong nonlinear warming contribution, and this is even stronger than in Case 1. However, the negative nonlinear contributions are much weaker than in Case 1 and are mainly limited to the Gulf Coast region. The stronger role of the nonlinear advection term in Case 1 may be a product of how we partition the cases. It is possible that there is a greater role for synoptic-scale eddies in Case 1 given the lack of prominent NAO influence, placing less restriction on the structure of the large scale circulation. Also, there are fewer events comprising the Case 1 composite, perhaps making the results a bit noisier. In either case, the apparent extended band of negative contributions may reflect case-to-case variability in the precise location of the leading cold front associated with each CAO event. Therefore, by comparing the linear and nonlinear advection terms in Case 1, it is possible that the primary term is the linear term until Day 0, after which the nonlinear term plays a greater role. The adiabatic term (Figure 5.2, middle right panel) is generally weak across most of the continental US, although there is weak adiabatic warming over portions of the eastern and southeast US, similar to Case 1. However, one difference between these two cases is the region of adiabatic warming just east of the Appalachian Mountains. As air descends down the leeward side of the mountain, it will warm adiabatically. This is consistent with the

location of a local minima in the temperature anomaly tendency field (as well as the linear temperature advection term #1), which is shifted further east in Case 2. As in Case 1, the diabatic heating contributions (Figure 5.2, bottom right panel) are weakly positive over much of the continental US, with a particularly strong maximum just off the East Coast (that is even stronger than in Case 1) which can be attributed to cold continental air being heated by the Gulf Stream.

To clarify the physical nature of the two linear advection terms, we graphically explore the relationship between the climatological-mean and composite anomaly fields. The two linear advection terms are decomposed into their separate field components for Case 1 and Case 2 in Figures 5.3 and 5.4, respectively. The results provide insight as to why the linear advection term #2 is stronger in Case 1. Comparing the top right panels in Figures 5.3 and 5.4, it is evident that differences in the linear temperature advection term #2 in Cases 1 and 2 (redisplayed in the bottom panels in Figures 5.3 and 5.4) are due to the relative magnitude of the composite temperature anomaly field across which the climatological westerly winds blow (towards the NE US). The temperature anomalies, and hence the temperature gradient, are stronger in Case 1, and leads to a stronger linear temperature advection term #2. This decomposition analysis also provides insight into the observed differences in the temperature tendencies. Notice the northward extent of the northerly anomalous winds in each case, shown in Figures 5.3 and 5.4 (top left panels). In Case 1, the northerlies originate in central Canada, where there is a very cold pool of air, while in Case 2, it appears that the northerlies are linked, at least in part, to the NAO circulation, originating instead over southeast Canada where the temperatures are not as cold, comparatively. These differences likely account for the differences in the magnitude

of the composite temperature anomalies between the two cases and accordingly, the temperature tendencies. Thus, the linear decomposition analyses are very illustrative and provide us with further insight into the underlying processes responsible for these cases.

Each term in the thermodynamic heat budget equation is evaluated for Case 3 as shown in Figure 5.5. The temperature anomaly tendency (Figure 5.5, top left panel) is positive over the entire eastern US and into eastern Canada, consistent with the sign of the temperature anomalies associated with these WW events, in opposition to the CAO cases. On the other hand, this term is negative over western Canada and over parts of the far western US. The linear advection terms (Figure 5.5, middle and bottom left panels) indicate collectively that there is warm advection occurring over the eastern half of the continental US during this time period, although it is evident that Term #1 accounts for nearly all of the linear advection occurring. The nonlinear advection term (Figure 5.5, top right panel) is quite small, especially over the SE region. Anomalous adiabatic cooling (Figure 5.5, middle right panel) occurs over the central and portions of the eastern US, coinciding with the strongest warm advection. This is consistent with the fact that warming air leads to rising motion and ultimately adiabatic cooling. Finally, the diabatic heating contributions (Figure 5.5, bottom right panel) are weakly negative over much of the US, with a particularly strong minimum just off the East Coast. The implication and interpretation of these diabatic heating contributions is not as straightforward as in the CAO cases and will be discussed in detail in a subsequent paragraph (page 115).

The corresponding analysis for Case 4 is shown in Figure 5.6. There is a high degree of similarity between the two WW cases, albeit with a few minor differences. Like for Case 3, the temperature anomaly tendency (Figure 5.6, top left panel) is positive over

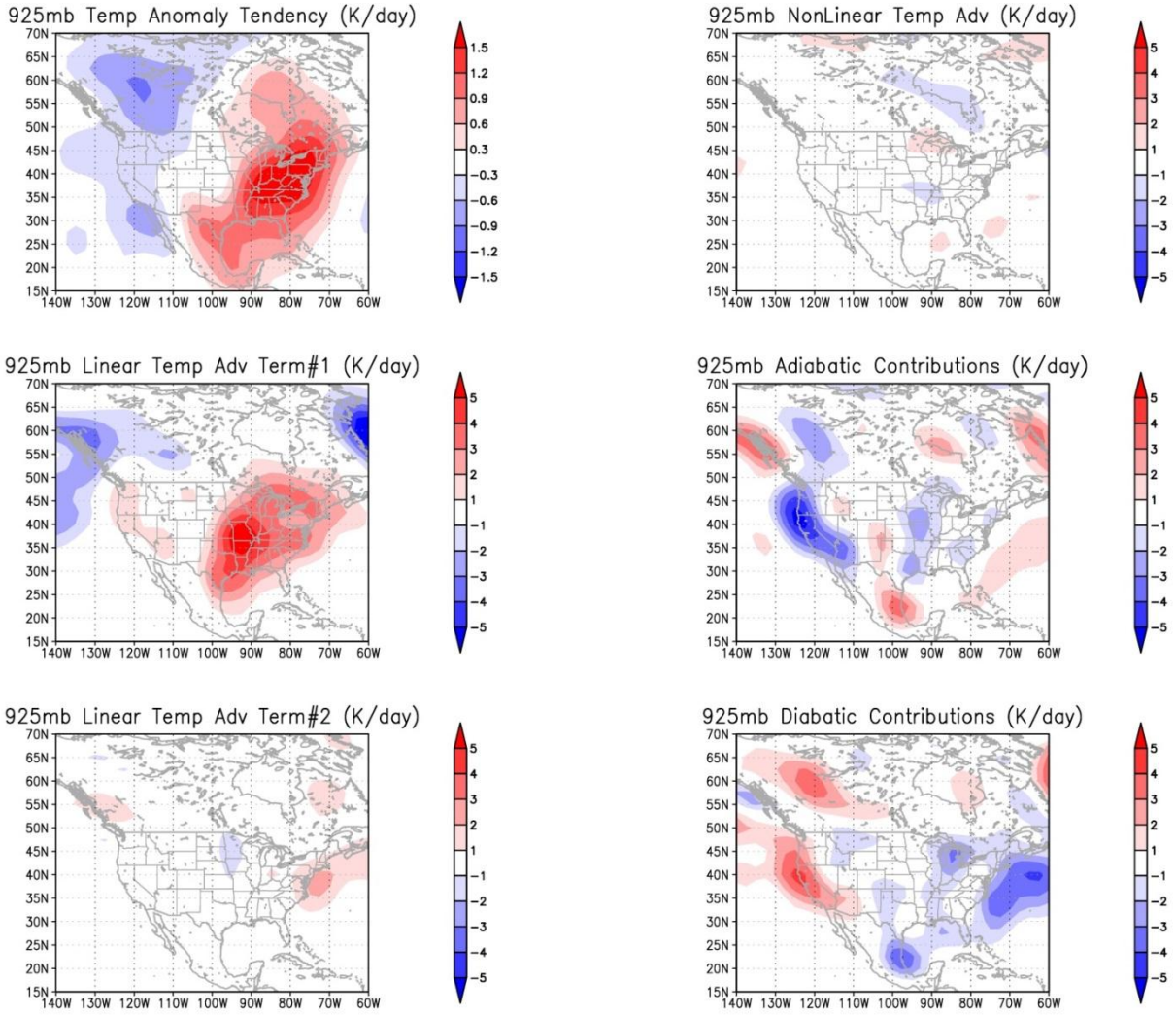

Figure 5.5: Same as Figure 5.1, except for Case 3 – SE WWs, Neutral PNA.

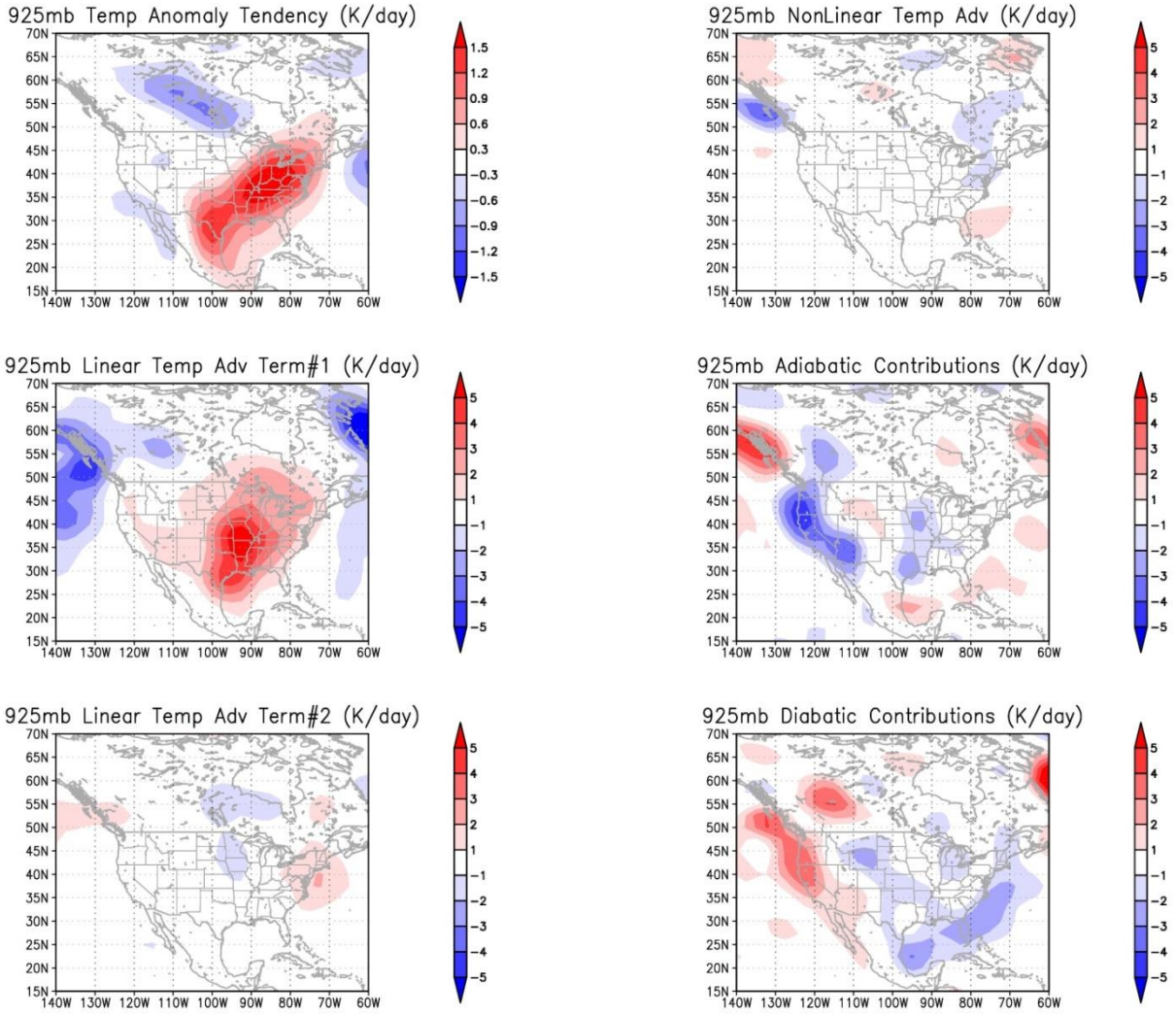

Figure 5.6: Same as Figure 5.1, except for Case 4 – SE WWs, Negative PNA

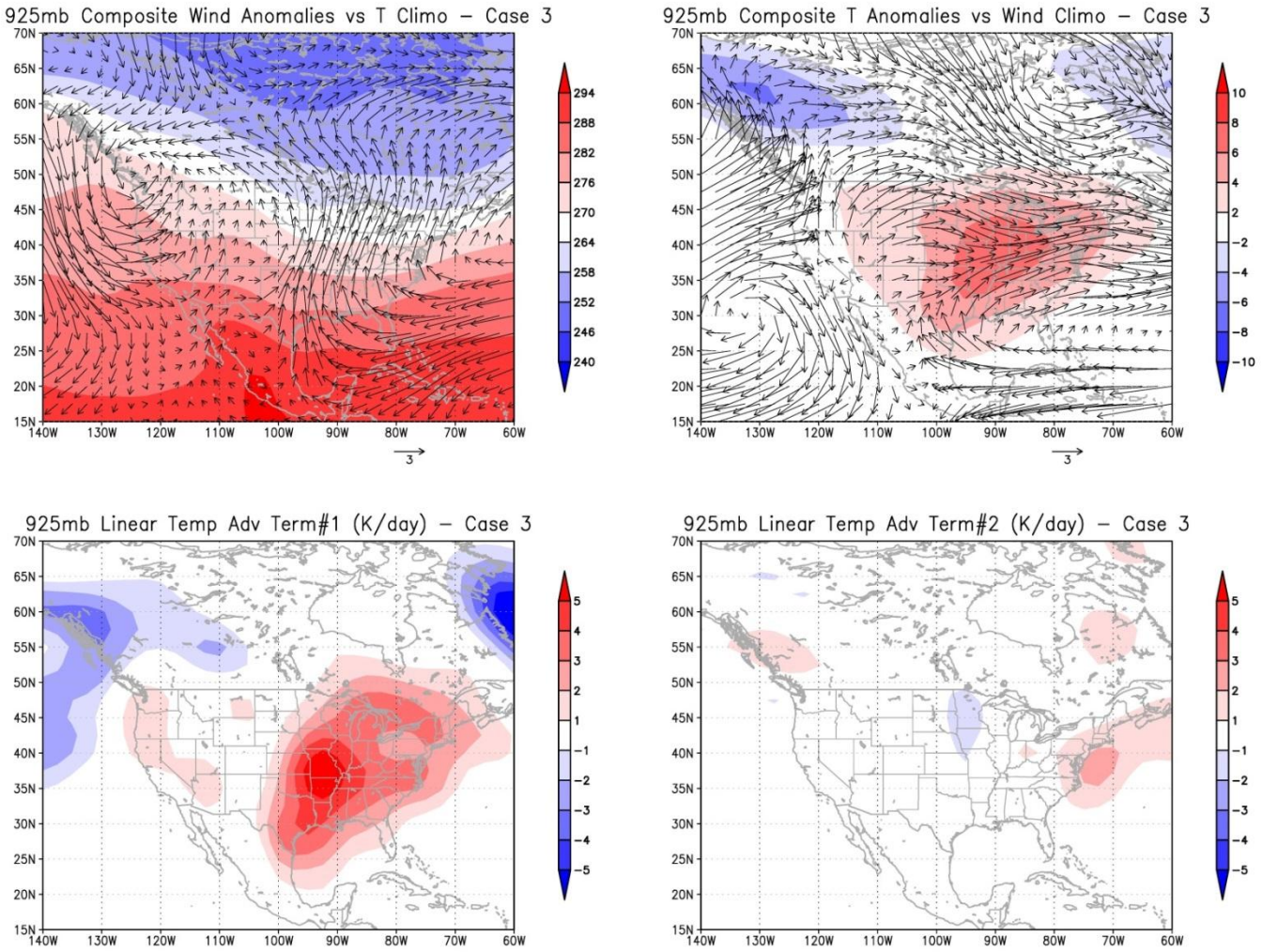

Figure 5.7: Same as Figure 5.3, except for Case 3 – SE WWs, Neutral PNA.

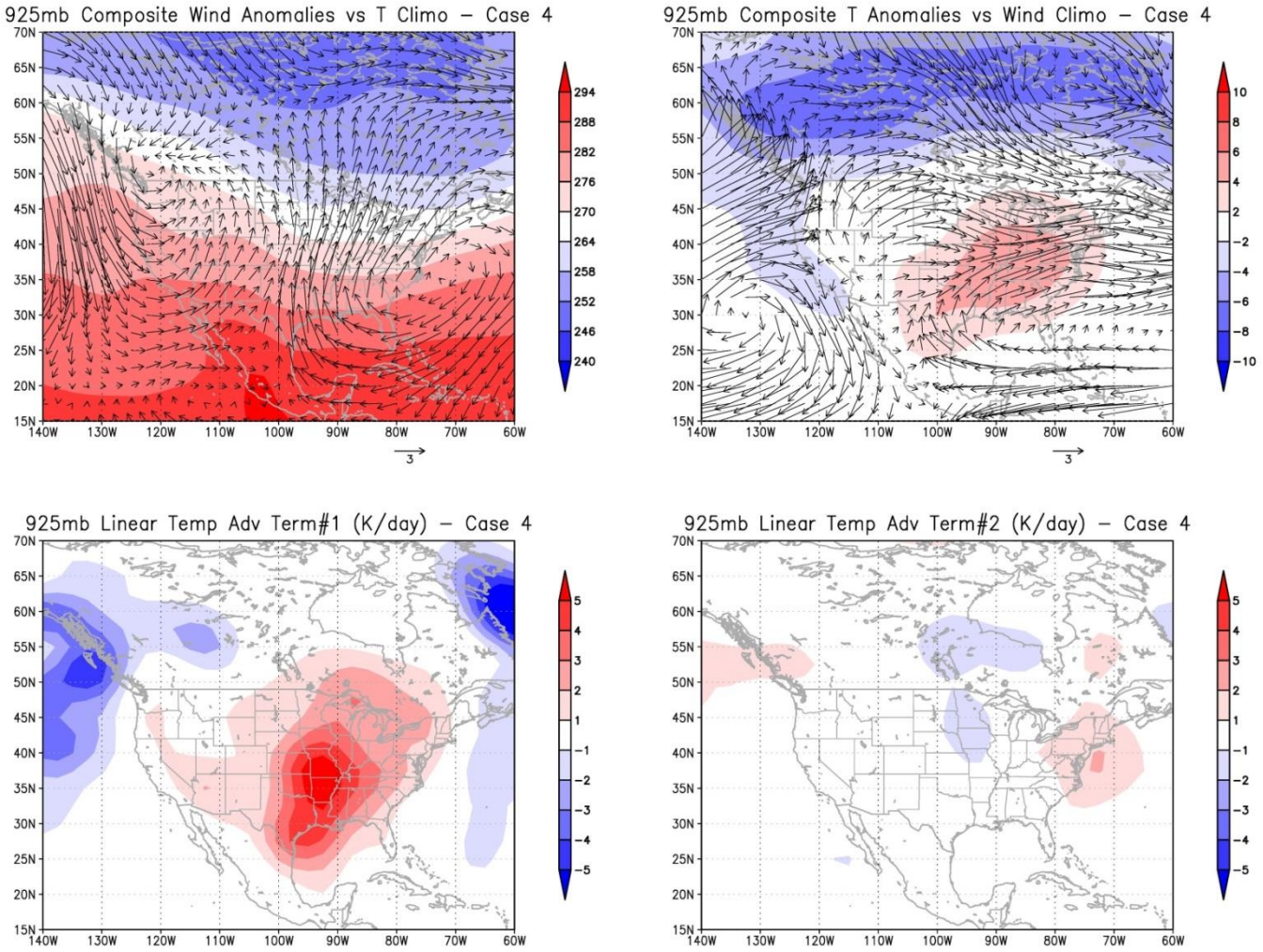

Figure 5.8: Same as Figure 5.3, except for Case 4 – SE WWs, Negative PNA.

the entire eastern US and into eastern Canada. However, in Case 4, the negative temperature tendencies are limited to central Canada and the temperature tendencies are not as spatially expansive as they are in Case 3. Together, the linear advection terms (Figure 5.6, middle and bottom left panels) indicate that there is warm advection occurring over the eastern half of the continental US during this time period, similar to the previous case. Again, it is evident that Term #1 accounts for virtually all of the warm advection occurring. Compared to Case 3, the magnitude of this term is slightly smaller in the current case. In addition, the contribution of this term in Case 4 spreads throughout nearly the entire continental US, whereas in Case 3 the warming is confined primarily to the eastern half of the US with a small signature on the West Coast. Otherwise, the structure of the maxima and minima are quite similar in the two WW composites. The linear advection Term #2 is slightly smaller in Case 4 than in Case 3. Similar to Case 3, the nonlinear advection term (Figure 5.6, top right panel) provides little contribution. As in the previous WW case, adiabatic cooling (Figure 5.6, middle right panel) occurs over portions of the continental US (although covering a slightly smaller area) in association with the strong warm advection. The maxima and minima in adiabatic cooling are similar in location and magnitude in both WW cases. Finally, the diabatic heating contributions (Figure 5.6, bottom right panel) are weakly negative over much of the US, with a relatively strong minimum just off the East Coast, although not as strong as in Case 3.

The companion linear decomposition analyses were also performed for the WW cases. As for CAOs, the linear advection Term #2 is *weaker* in the composite for which low frequency modes are implicated. Comparing the top right panels in Figures 5.7 and 5.8, it is evident that differences in the linear temperature advection term #2 in Cases 3

and 4 (shown again in the bottom panels in Figures 5.7 and 5.8) can be accounted for by the relative magnitude of the composite temperature anomalies and associated temperature anomaly gradient. This result is very similar to that found for the CAO cases.

Comparing the results for CAOs and WWs, several differences are identified. First, the terms on the right hand side of the thermodynamic equation (5.1) are generally slightly *smaller* in magnitude for WWs than for CAOs. However, it is not clear why this is the case. Further, while the signs of the linear advection terms switch over the region of interest between the WW and CAO cases, the spatial patterns are *not* mirror images of one another. The extrema are in slightly different locations, possibly indicating either (i) different mechanisms are at play in each event type or (ii) differences in the air mass source regions in the respective cases. Finally, as eluded to previously, in the CAO cases, the Gulf Stream provides a positive diabatic heating anomaly contribution off the East Coast while in the WW cases we observe a negative diabatic anomaly. The interpretation of the diabatic warming in the CAO cases is straight-forward, as the observed diabatic heating anomaly pattern is physically consistent with the presence of the Gulf Stream (i.e. the warm waters of the Gulf Stream heat the air from below). However, the interpretation of the anomalous diabatic cooling in the WW cases comes from a consideration of the composite anomaly heat budget in relation to the climatological-mean heat budget (not shown). More specifically, the negative diabatic contribution in the WW cases is likely due to a reduced (from climatological values) warming in this region in association with anomalous *onshore* flow. In the CAO cases, the very cold air clearly gets swept out over the very warm Gulf Stream, where the warm ocean below heats the cold air in the lower troposphere. However, in the WW cases, the winds are blowing warm, oceanic air to the

continent. In a climatological-mean sense, however, there is typically some degree of offshore flow due to the prevailing westerly flow. This is partially offset during the WW cases, leading to a reduction in diabatic heating rates compared to climatological-mean values. Thus, we attribute the negative diabatic heating anomalies in the WW cases to a "lack" of warming due to diminished offshore flow.

Thus, warm (cold) advection is the largest contributor to the observed temperature tendencies in both WW and CAO cases. The linear advection of the climatological-mean temperatures by composite wind anomalies plays the primary role, while the nonlinear advection plays a smaller role (especially in the WW cases). This helps to justify our use of composite analyses to study ETR events (since case-to-case variability is embedded in the nonlinear advection term). Both the linear and nonlinear terms contribute positively to the temperature tendencies of interest. In the CAO cases, we attribute the nonlinear cold advection signatures found along the Gulf and Atlantic coasts to case-to-case variability in the spatial progression of the leading edge cold fronts after Day 0 (noting that these frontal features will be more closely aligned with one another at Day 0, the time of cold wave onset). In contrast, both the adiabatic and diabatic terms generally oppose the local temperature tendencies, effectively offsetting a portion of the advection contributions.

Given the primary importance of Term #1, the linear advection of climatological-mean 925 hPa temperature by the composite 925 hPa wind anomaly field, it is of direct scientific interest to assess which atmospheric dynamical features are responsible for inducing the 925 hPa wind anomaly field. Since the forcing term is linear with respect to the anomaly field, this issue can be addressed by simply considering the period-averaged

circulation anomaly field. This is approached using a PV dynamical formalism to relate the 925 hPa circulation anomaly field to distinct features in the 3-D PV anomaly field.

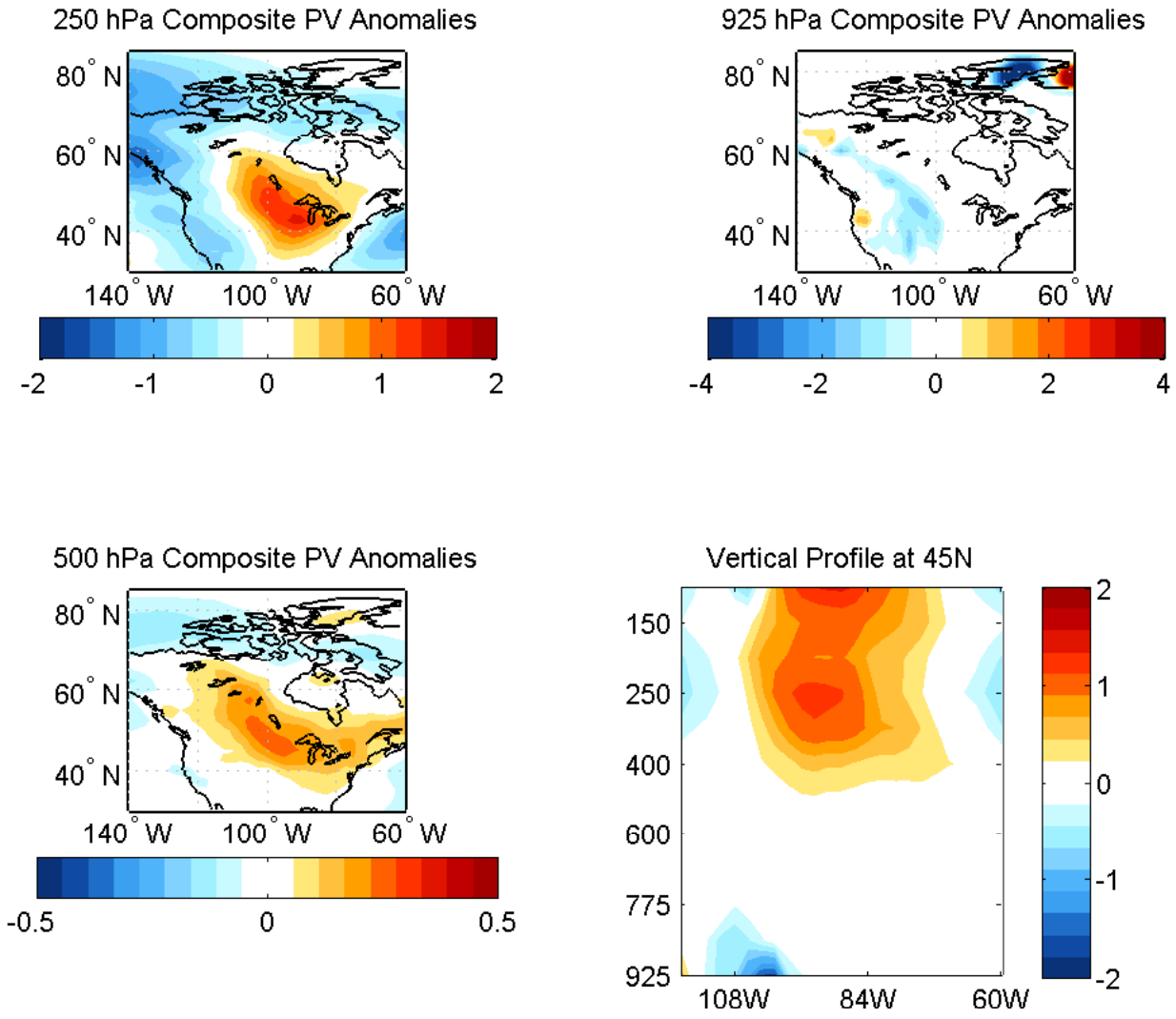

Figure 5.9: Composite PV Anomalies in PVUs (1 PVU = 10^{-6} $m^2s^{-1}Kkg^{-1}$) at 250 hPa, 500 hPa, and 925 hPa and a Vertical Profile at 40N for Case 1.

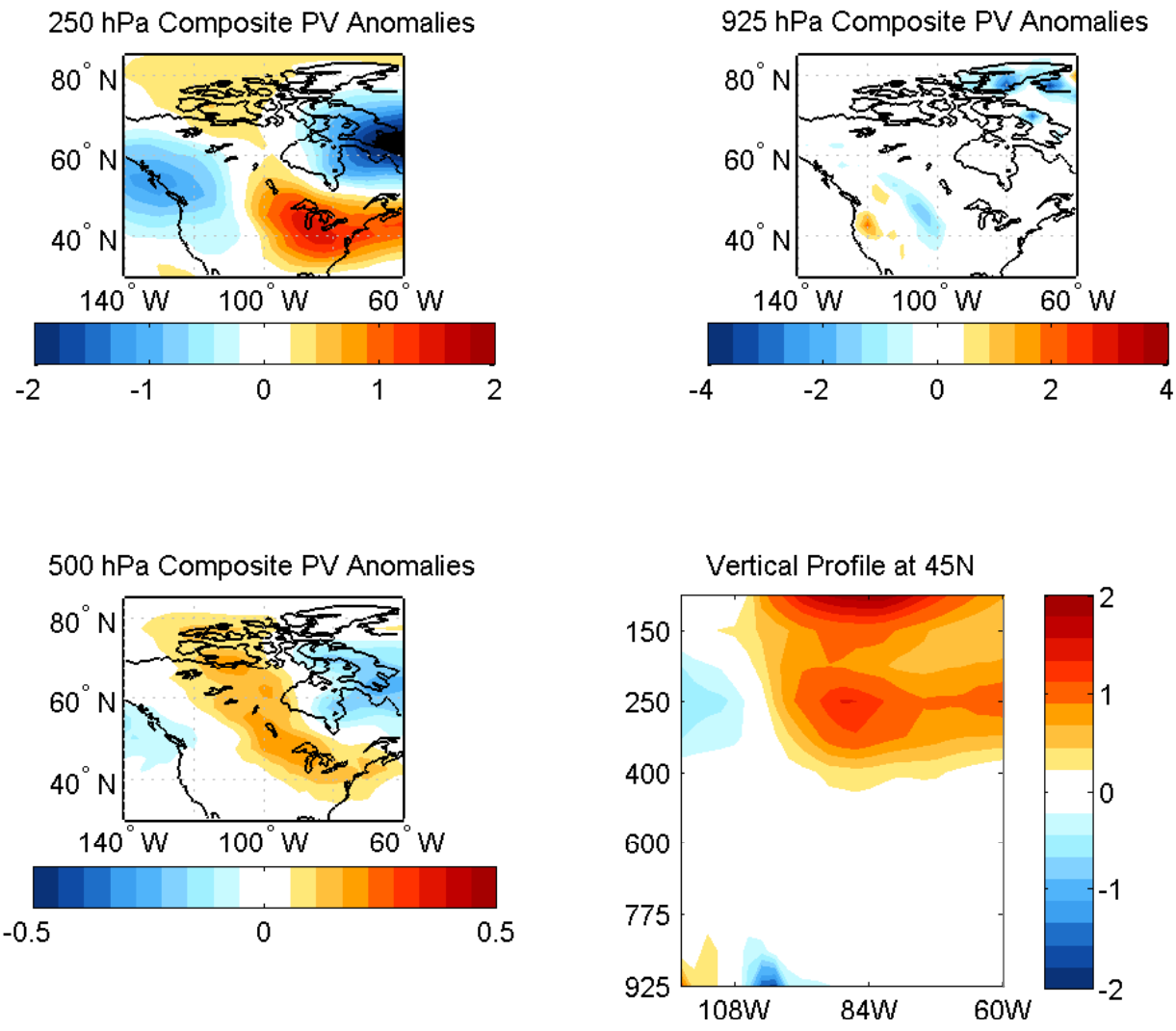

Figure 5.10: Same as Figure 5.9, except for Case 2.

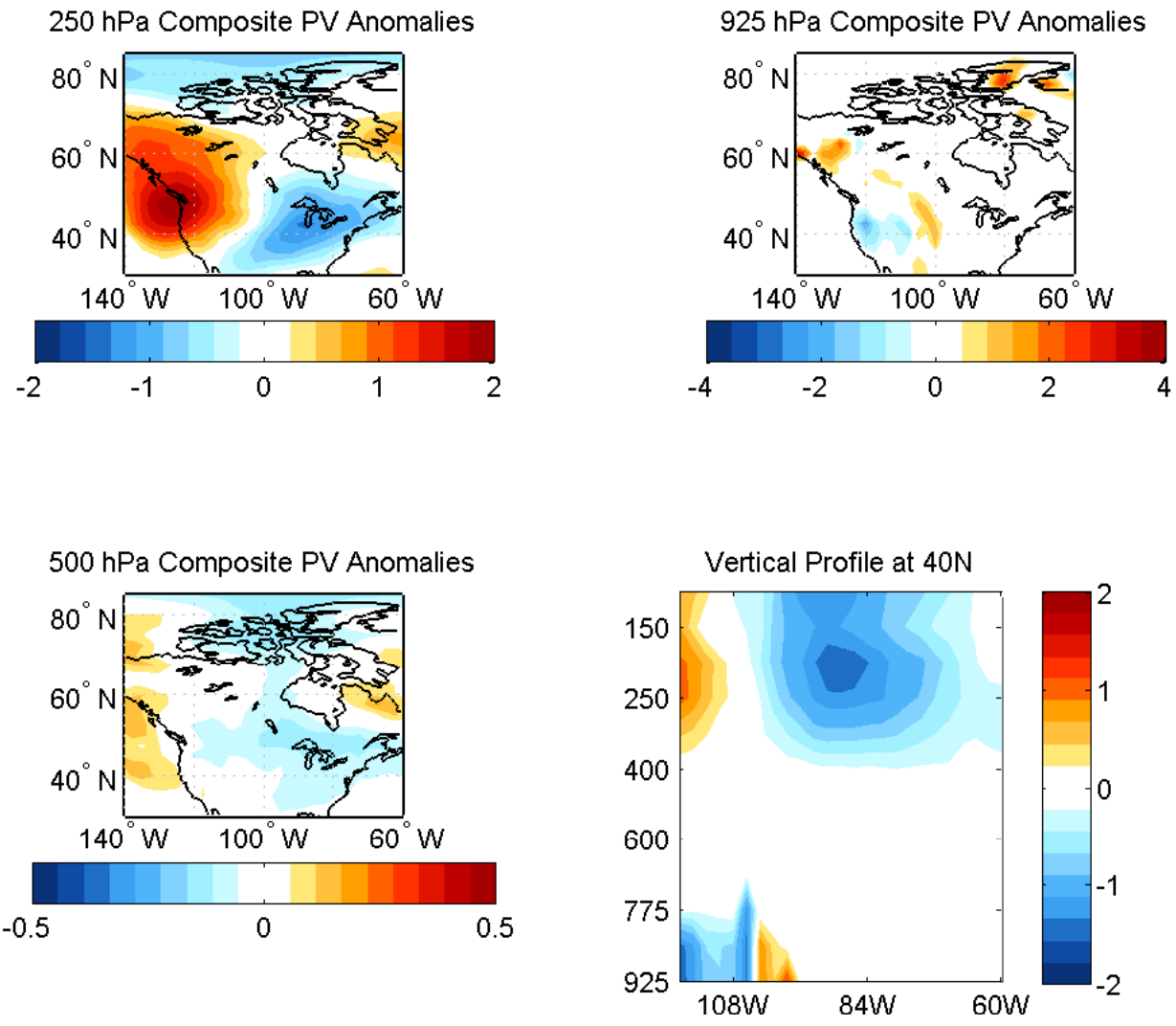

Figure 5.11: Composite PV Anomalies at 250 hPa, 500 hPa, and 925 hPa and a Vertical Profile at 45N for Case 3.

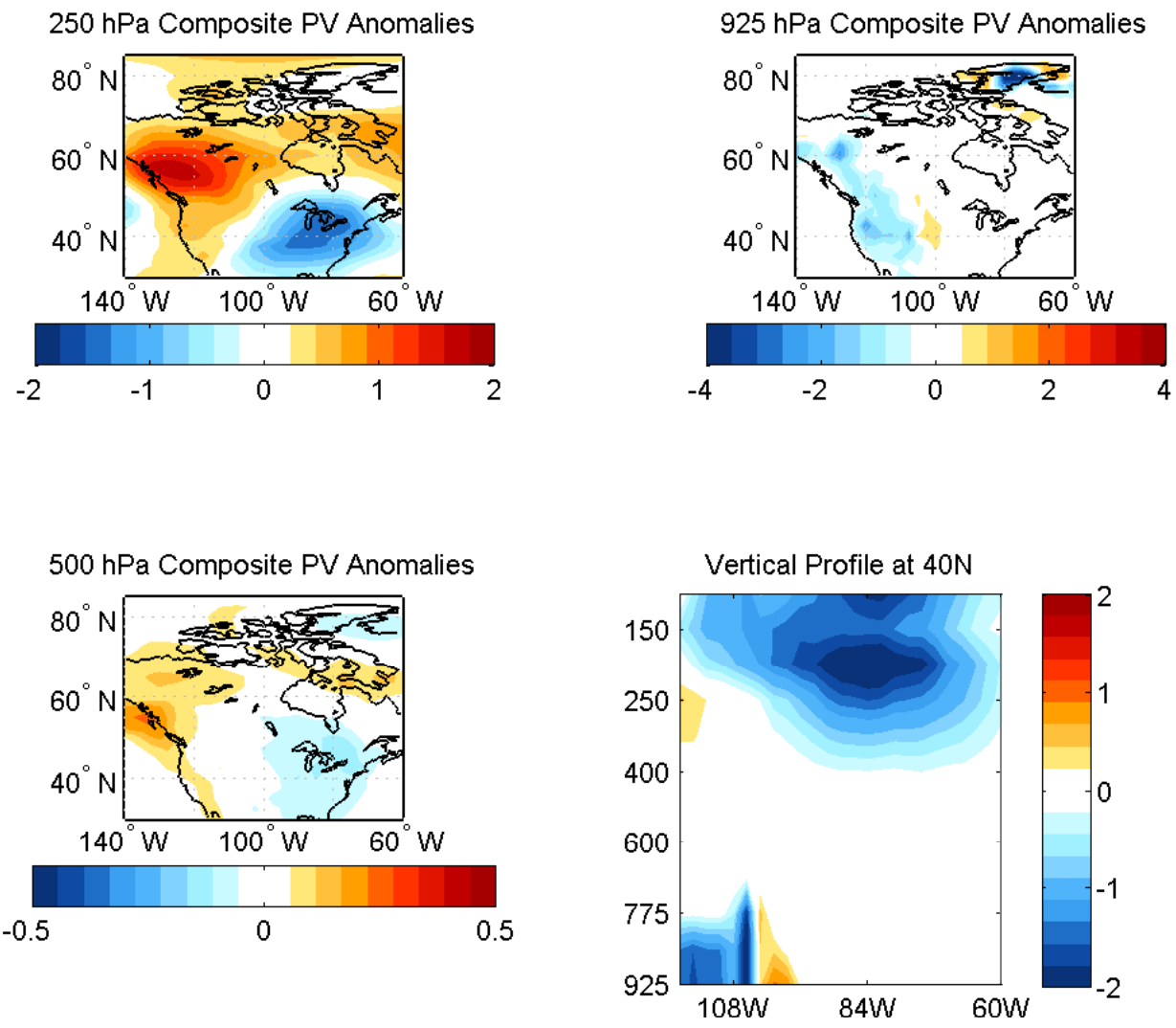

Figure 5.12: Same as Figure 5.11, except for Case 4.

5.3.2 PV Analyses

A suite of piecewise PV inversion analyses are performed next in order to isolate the contributions of distinct dynamical features to the near-surface composite circulation anomaly fields determined to be mainly responsible for ETR onset (in the heat budget analyses discussed above). Such analyses will provide specific dynamical insight into the

mechanisms leading to ETR onset. The next analyses will address several questions: (i) Which atmospheric levels exhibit notable composite PV anomaly structures during ETR events? (ii) Which PV anomaly features are dynamically linked to the circulation pattern in the lower troposphere and provide notable contributions to the 925 hPa surface wind anomaly field?, and (iii) Do these PV anomaly features influence the movement of the cold (warm) air associated with CAO (WW) onset? A local PV anomaly feature induces an oppositely-signed geopotential anomaly field that extends horizontally and vertically into the far field, with progressive amplitude decay (Hoskins et al. 1985, Black and McDaniel 2004). Upper tropospheric PV anomalies having large amplitude and/or spatial scales will have the potential to impact the near-surface circulation.

Period-averaged composite PV analyses and piecewise PV inversion analyses are performed to provide answers to the above questions. However, before the inversions are performed, composites of the PV anomalies averaged over the same time period used for the heat budget analyses (Days -4 to +2) are analyzed to help identify which PV anomaly structures to use in the inversions. Horizontal maps and vertical cross-sections of period-averaged PV anomalies are shown in Figures 5.9-5.12 for each composite. The levels presented for the horizontal PV anomaly analyses are 925 hPa, 500 hPa and 250 hPa, corresponding to the levels analyzed in the composite analyses presented in Chapter 4. The vertical profiles are shown at 40N and 45N for WWs and CAOs, respectively. These latitudes were chosen because they provide the most coherent depiction of PV anomaly structures. These selections are also consistent with the idea that WWs tend to be centered slightly further south than their CAO counterparts (likely due to the respective locations of their source regions). Overall, these composite PV anomaly analyses reveal

coherent dynamical features associated with ETR onset, helping to synthesize the time evolving synoptic analyses presented in the previous chapter. The largest PV anomaly amplitudes are found in the upper troposphere with weaker anomalies found in the lower atmosphere near the surface. The weakest anomalies are typically located in the mid-troposphere. The upper tropospheric PV anomaly patterns have horizontal structures that would be associated with southerly (northerly) winds over the central and eastern US during WW (CAO) onset. In some cases, these induced flow patterns are supplemented with contributions from upstream upper-level PV anomaly features of opposite sign. As seen in the previous chapter, the main upper-level PV structures are structurally similar in the mode cases and neutral cases (for both WWs and CAOs) leading to similar local 925 hPa circulation anomaly in the mode cases and neutral cases (whether they originate from propagating and/or quasi-stationary disturbances). For instance, in the CAO cases, Case 1 is associated with a transient cyclone-anticyclone couplet while Case 2 is associated with a quasi-stationary couplet that is locally enhanced by a transient circulation feature. Even though these features are different in nature, the resulting cyclone-anticyclone couplets occurring during CAO onset are located in the same regions and are characterized by similar PV anomaly signatures. Even though the PV anomaly amplitudes near the surface are smaller in magnitude and area than those in the upper troposphere, their proximity to the surface, where the key meridional air temperature transport occurs, gives them the potential to provide a fundamental contribution to ETR onset. Thus, from the composite PV analyses, we had identified distinct and potentially important PV anomaly features. Specifically, there are coherent PV anomaly features located in both the upper and lower atmosphere for each ETR category, with the upper level PV signatures more prominent

(stronger and larger) than the ones at the surface. Because the influence of the PV anomalies extends radially outward, this implies that it is possible that some of the upper level PV anomaly features may provide important contributions to the surface wind field. Therefore, we want to now assess *which of these regions of PV are most important in inducing the composite surface wind anomalies* associated with ETR onset. This is readily approached using a piecewise PV inversion approach.

Before using PV inversions to isolate specific layers and regions of PV, we first verify the quantitative utility of a quasi-geostrophic approach in this setting. This is done via a comparison of the actual composite wind anomaly field to the geostrophic wind anomaly field obtained from inverting the entire distribution of QGPV anomalies. These respective fields are contrasted for each case in Figure 5.13. It is evident that, in the regions of interest, there is a very high degree of similarity between these two fields in each case (noting the disagreement occurring over the western mountains, where some of the levels we analyze extend below the surface). These results confirm the utility of employing the QG approach and using the geostrophic wind as a proxy for the actual wind (and hence, our assumption is valid). There are two main reasons why this is useful for our purposes: (i) the quasi-geostrophic balance condition (relating PV anomalies to geopotential height anomalies) is linear (see equation 5.2), allowing for an unambiguous partitioning of the circulation anomaly field, and (ii) the parallel requirements of hydrostatic and geostrophic balance constrain the structure of the horizontal velocity field to be directly determined by the distribution of geopotential height on isobaric surfaces, which is in turn directly related to the PV distribution via the QG balance.

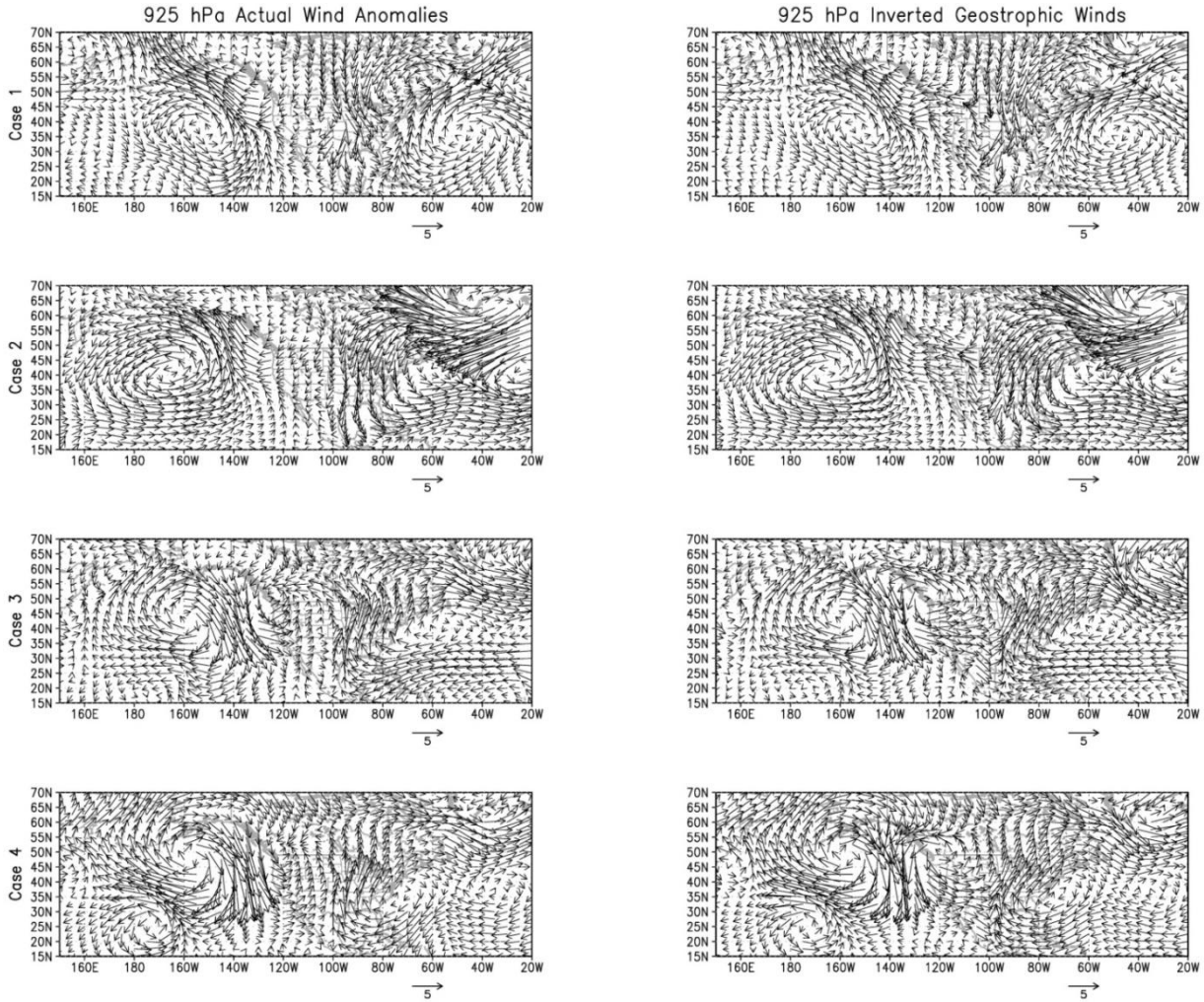

Figure 5.13: The 925 hPa actual wind anomalies (left column) compared to the 925 hPa inverted geostrophic winds (right column) for each case. The high degree of similarity between the columns verifies that the inversion routine is working properly and that the geostrophic wind is a good approximation of the actual wind field.

First, PV anomalies on individual isobaric layers, ranging from 1000 hPa to 100 hPa, are inverted (not shown) to assess the individual contribution of each layer toward the 925 hPa wind anomaly field. These analyses provided information on the nature of how each PV layer contributes. Noting that vertically adjacent layers sometimes provide a similar contribution, the results can be used to vertically partition the PV anomaly fields into groups of levels that provide a similar impact. In addition, the vertical profiles of PV anomalies (see Figures 5.9-5.12) indicated several vertically coherent PV anomaly structures. Based on a combined consideration of the layer-by-layer PV inversion and the vertical PV cross sections, the tropospheric PV anomaly distribution is partitioned into three distinct layers: (1) the lower troposphere (LTPV; 1000-850 hPa, which includes the contribution of surface potential temperature anomalies), (2) the middle troposphere (MTPV; 700-500 hPa) and (3) upper troposphere (UTPV; 400-100 hPa). The results of the multi-layer piecewise PV inversion analyses are shown in Figures 5.14 (for CAOs) and 5.16 (for WWs). Our proximate objective in pursuing these analyses is to discern which tropospheric dynamical features induce the composite horizontal wind anomaly field (vectors) over the central and eastern continental US displayed in the upper left panel of Figures 5.3 and 5.4 (for CAOs) and Figures 5.7 and 5.8 (for WWs), since our heat budget analyses indicate that these anomalies provide the primary forcing for ETR onset.

Figure 5.14 (left column) displays the respective contributions of the three tropospheric layers to the 925 hPa level wind field. The LTPV induces a strong clockwise circulation centered over Minnesota that contributes strongly to the northerlies over the eastern US and is consistent with the cold SAT anomaly pattern in that area (indicating a

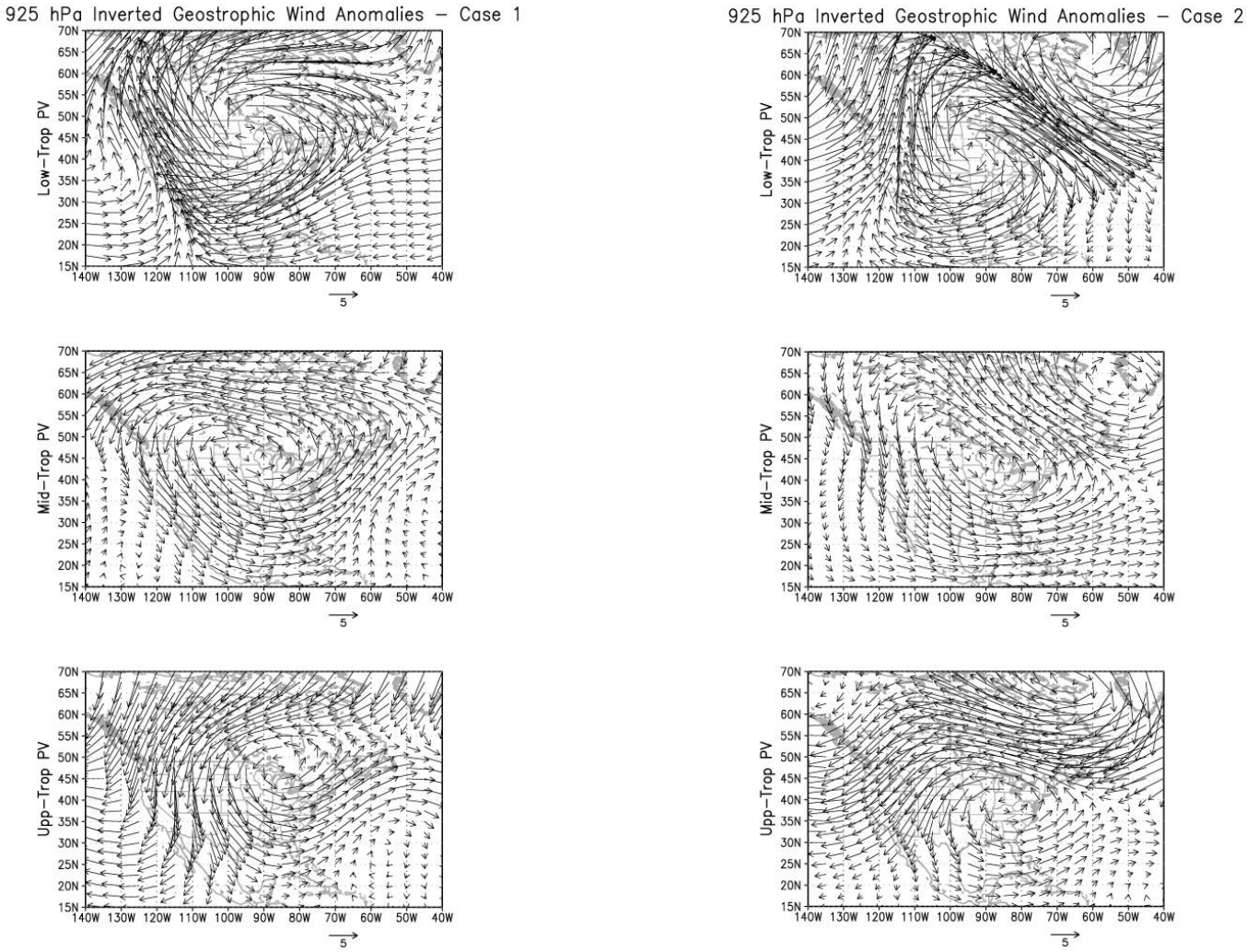

Figure 5.14: The 925 hPa inverted geostrophic wind anomalies for Case 1 and Case 2 when only the lower-tropospheric PV (top row), the mid-tropospheric PV (middle row), and the upper-tropospheric PV (bottom row) is inverted.

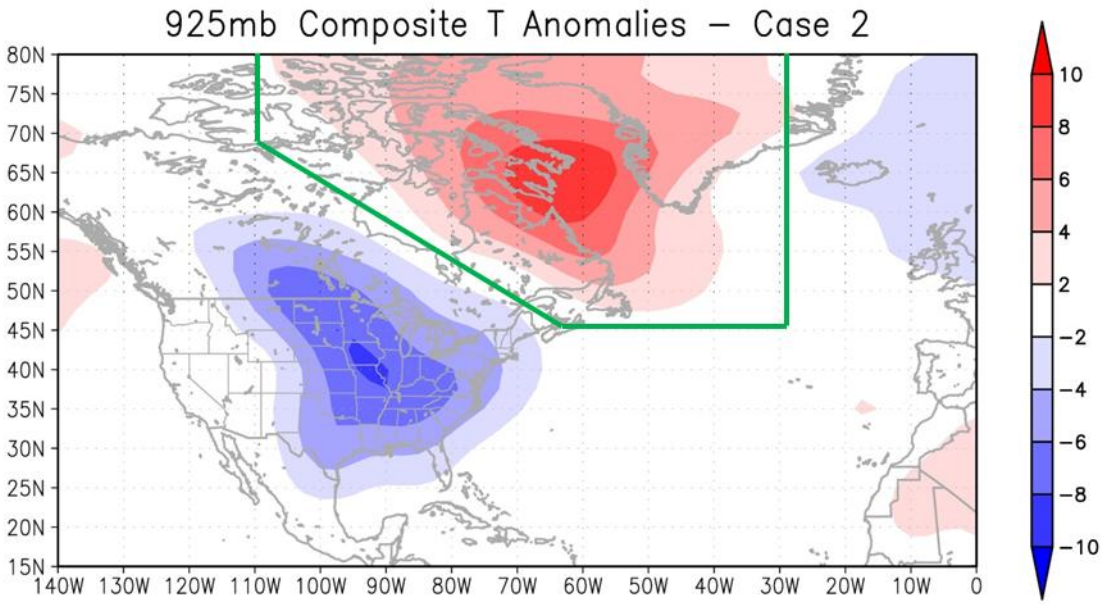

Figure 5.15A: 925 hPa Composite surface air temperature anomalies for Case 2. For the horizontal partition, the positive anomaly associated with the negative NAO is isolated and is outlined in green.

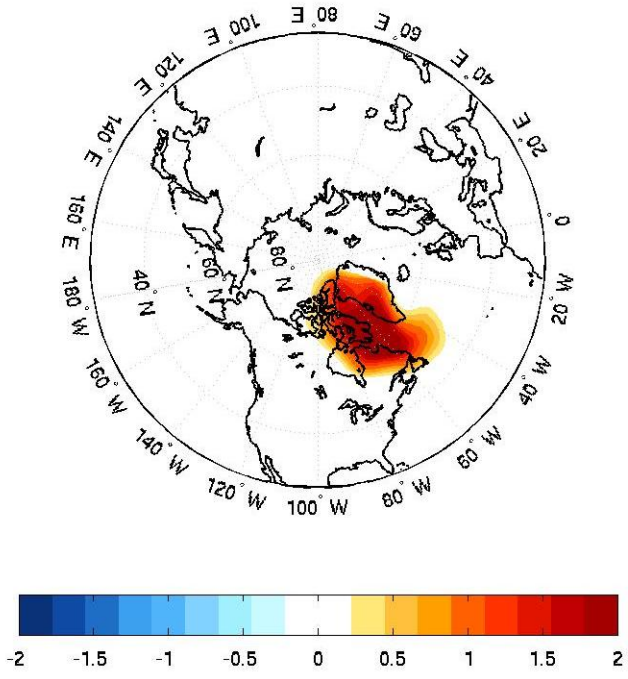

Figure 5.15B: The corresponding region of input QGPV at 925 hPa associated with the warm T anomaly for the horizontal partition PV inversion analysis for Case 2.

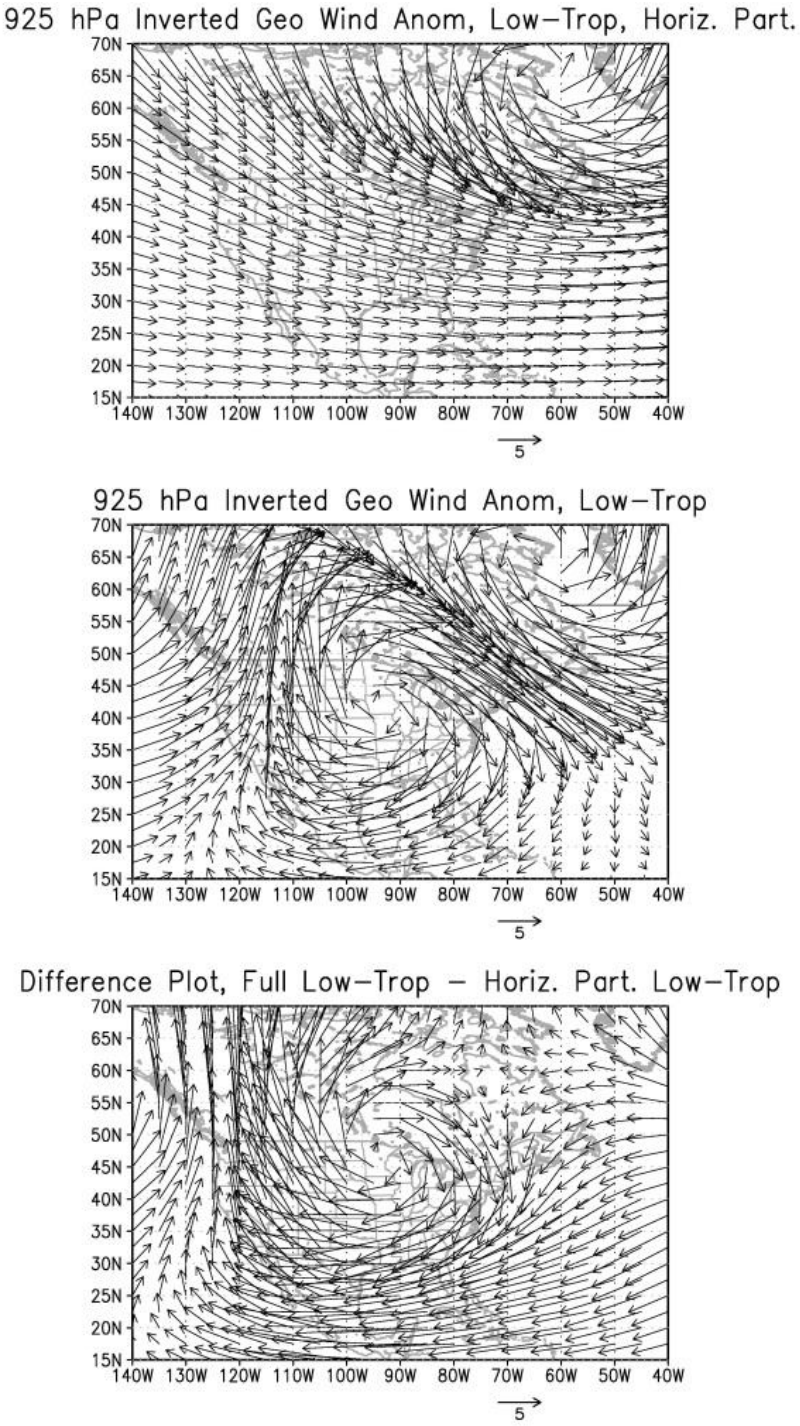

Figure 5.16: The 925 hPa inverted geostrophic wind anomalies when the lower-tropospheric PV is inverted with the horizontal partition applied (top panel). For comparison, the middle panel shows the 925 hPa inverted geostrophic wind anomalies when the entire lower-tropospheric PV field is inverted. The difference between these two fields is shown in the bottom panel.

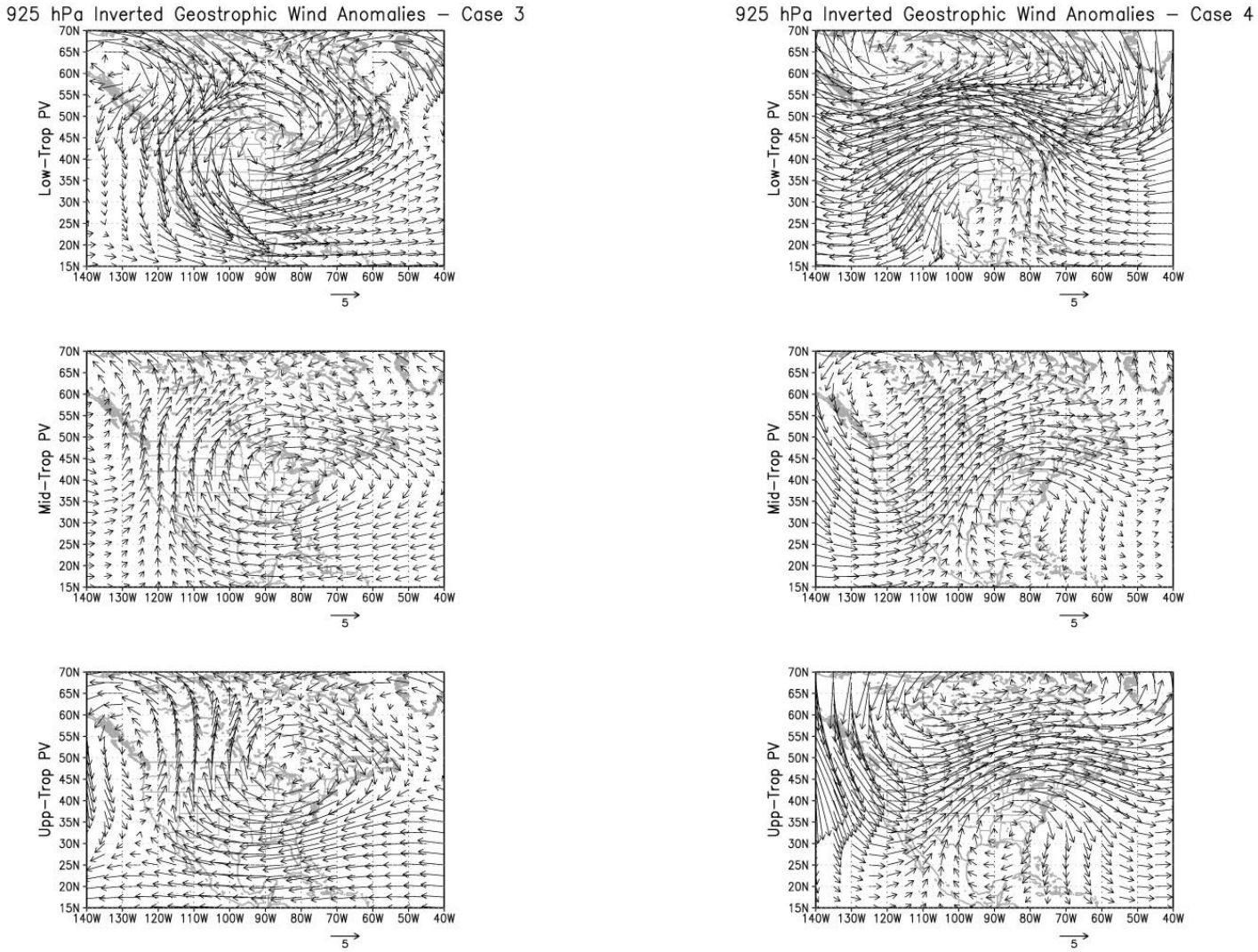

Figure 5.17: Same as Figure 5.14, except for Case 3 and Case 4

robust contribution from surface potential temperature). In contrast, the MTPV provides an opposing contribution (southerly winds) over the eastern US. Although the UTPV also opposes the LTPV contribution over the eastern US, it provides northerly flow over the upper Midwest and central US, contributing positively to cold advection over this region. The similarities in the contributions of MTPV and UTPV is consistent with our vertical profiles of PV anomalies, where we identified similar-signed (albeit phase-shifted) PV anomalies in the mid- and upper-troposphere which are of opposite sign to near-surface PV anomalies. Hence, there is some cancellation between the contributions of LTPV and MTPV/UTPV. Overall, the LTPV provides the greatest contribution to the northerly 925 hPa winds over the eastern US while the UTPV induces robust northerlies farther to the west over the central US. The LTPV feature is tied to the transient surface high pressure system (identified in Chapter 4, see conclusions section for succinct summary) and the cold surface potential temperature anomaly associated with the cold air outbreak, itself. The latter observation brings up the interesting possibility that the CAO is initiated over the Midwest by the UTPV feature, but then extends eastward in association with the anti-cyclonic circulation induced by the surface potential temperature anomaly, itself.

The PV inversions for Case 2 (Figure 5.14, right column) are strikingly similar to the results of Case 1 and also indicate that the LTPV anomaly field seems to provide the greatest contribution to the northerly 925 hPa winds over the eastern part of the domain of interest. There are differences in the locations of the centers of rotation within each layer of the troposphere reflecting slightly different locations of the SAT anomalies in each case. However, the interpretation of Case 2 is altered from Case 1 due to the apparent role of the NAO. Starting in the upper troposphere (Figure 5.14, bottom right

panel), it appears that the circulation over the NE US and SE Canada that is tied to the NAO brings in warm air to these regions at the surface (as indicated by the easterly winds blowing from the northwestern Atlantic Ocean into NE North America). The hypothesized process through which this occurs is as follows. First, the negative UTPV anomaly associated with the NAO induces an anticyclonic circulation anomaly that extends down to the surface. This upper level circulation is consistent with the geopotential height plots in Figure 4.4A, and the downward extension of the circulation associated with this PV anomaly is evident in the bottom right panel of Figure 5.14 (which shows the 925 hPa inverted geostrophic winds when only the UTPV is inverted). Eventually, the resulting near-surface temperature advection leads to the creation of a local warm surface air temperature anomaly over eastern Canada, which in turn induces low pressure and a cyclonic circulation anomaly in the lower troposphere, helping to enhance the surface northwesterly wind anomalies found over the northeast US. The surface low is evident in the upper right panel of Figure 5.14, and is collocated with the warm SAT anomalies observed in Figure 4.3. Thus, the warm anomaly and its associated surface low provide northwesterly winds on their southern flank that likely helps push cold air from Canada into the SE US. Thus, the PV inversion results suggest the means by which the NAO likely affects this category of CAO events. However, an additional horizontal partitioning of the lower tropospheric PV field is necessary to discern whether the role of the NAO is direct or indirect.

For the horizontal partition, we want to isolate the positive SAT anomaly in the lower troposphere that is associated with the NAO. To identify the partition boundaries, I examined a distribution of the SAT anomalies for Case 2 (Figure 5.15A). The region I

want to isolate is outlined in green. After identifying the desired region, I isolated the corresponding region of QGPV for the lowest three layers of the atmosphere (included in our definition of the low-troposphere). The corresponding region of QGPV is shown in Figure 5.15B for the 925 hPa level, but is similar in structure at the other two levels directly above and below. Finally, I ran the PV inversion routine with this horizontal partition of PV.

The results of the PV inversion analysis for Case 2 with the horizontal partition applied are shown in Figure 5.16. The top panel isolates the net influence of the LTPV anomalies enclosed by the green contour in Fig. 5.15A. Given that there are relatively strong northwesterly winds in the top panel that overlap with the total LTPV circulation shown in the middle panel (925 hPa wind anomalies induced by the entire LTPV field), it appears that at least a portion of the northwesterly winds can be traced back to the NAO. The difference between these two figures is attributed to the circulation induced by the surface cold anomaly centered over the US, as confirmed by the difference plot (bottom panel). Thus, these results indicate that *the NAO provides a direct partial contribution to US CAO events*. Further, these results confirm a suggestion in Westby and Black (2015) that the NAO isn't sufficient by itself to initiate CAOs, but acts in concert with other transient synoptic features.

The PV inversions for Case 3 are shown in Figure 5.17 (left column). In this case, each of the three layers troposphere contributes substantively to the 925 hPa wind field. There is a counterclockwise circulation centered over Wisconsin induced by LTPV that contributes to westerly or southwesterly winds over the eastern half of the US. In contrast, the MTPV provides an opposite contribution (easterly or northeasterly) to the

LTPV contribution over the eastern US. The UTPV contributes in a similar fashion to the MTPV anomalies (countering the LTPV), but with a pattern that is shifted northward. This finding is consistent with our prior vertical profiles of PV, where we identified similar-signed PV anomalies in the mid- and upper-troposphere which are of opposite sign to the near-surface PV anomalies. Hence, there is some cancellation between the influence of the LTPV and that of the MTPV and UTPV. However, there are some inconsistencies in this case. First, the center of circulation in the top left panel of Figure 5.17 is located northeast of the positive PV anomaly at 925 hPa (Figure 5.11, top right panel). This dislocation can be attributed to the PV signature at 850 hPa (not shown). At 850 hPa, there is a much broader region of positive PV anomalies that extends from the Rocky Mountains up into Canada and over the Great Lakes. In addition, there is a juxtaposition of regions of positive PV and negative PV over the Southeastern/Mid-Atlantic states that would jointly produce a circulation as shown (Figure 5.17, top left panel). Further, the near-surface center of the circulation shown in the left column of Figure 5.17 is not collocated with the SAT anomaly (Figure 5.7, top right panel) as it is in other cases. Therefore, it isn't immediately clear in this case what the primary mechanism is for this category of events. In the previous chapter, we attributed this category of events as being initially (subsequently) associated with transient anomalous low (high) pressure near the Pacific Northwest (SE) coast. However, neither of these aspects is clearly indicated in Figure 5.17 (left column).

The PV inversions for Case 4 are clearly very different than the previous case. The LTPV enacts southerly or southeasterly winds over the eastern and southern US, in association with a counterclockwise circulation due to the warm SAT anomalies in that

region (Figure 5.8, top right panel). The mid- and upper-troposphere provide very similar contributions, unlike Case 3 where they were distinct, and provide westerly winds across much of the US with southwesterlies to the east of the Rockies. However, the interpretation of Case 4 is different than Case 3 and can be attributed to the role of the PNA. The upper-level PNA pattern (as observed in 4.4B, right column) helps induce a near-surface temperature advection pattern that creates a warm anomaly over the southwest/south-central US (Figure 5.17, bottom right panel). Then, upon creation of the warm anomaly (as a result of the aforementioned warm advection), the warm anomaly creates its own counterclockwise circulation in the lower troposphere as indicated in the top right panel of Figure 5.17. This circulation around the warm anomaly then leads to warm advection further to the east in the US (along the SE coast) and hence leads to its progression to the SE US. Thus, in this case, the warm anomaly is initiated *due to a direct contribution from the PNA teleconnection pattern* with a subsequent self-progression of the warm anomaly to the east coast region.

5.4 Summary & Conclusions

This research provides important information on the thermodynamic and dynamic processes and physical mechanisms leading to ETR development. It also dynamically clarifies the role of low frequency modes in ETR development. Diagnostic analyses, including heat budget and piecewise PV inversion analyses, are used extensively in this study and provide a strong foundation for identifying the primary mechanism(s) responsible for ETR development because they are based upon fundamental dynamical and thermodynamical principles.

First, the thermodynamic contributions to ETR formation have been quantified and helps improve the scientific understanding of the scenarios in which ETRs form. Specifically, warm (cold) advection is the largest contributor to the observed temperature tendencies in WW (CAO) cases. The linear advection of the climatological-mean temperatures by composite wind anomalies plays the primary role, while the nonlinear advection plays a smaller role (especially in the WW cases). Both the linear and nonlinear terms contribute positively to the temperature tendencies of interest. In contrast, both the adiabatic and diabatic terms generally oppose the local temperature tendencies, effectively offsetting a portion of the advection contributions. In addition, the two linear advection terms were decomposed into their separate field components to clarify the physical nature of the two linear advection terms. It was found that the advection of the composite temperature anomalies by the climatological-mean winds is *weaker* in the composite for which low frequency modes are implicated. This difference can be accounted for by the relative magnitude of the composite temperature anomalies and associated temperature anomaly gradient. Further, the linear decomposition analyses indicate that the temperature gradients are typically weaker where low frequency modes are implicated, and hence lead to a weaker advection of the composite temperature anomalies by the climatological-mean winds. However, even though the ETR cases associated with low frequency modes are slightly weaker in terms of temperature anomalies, they may make up for this by an increased duration (Table 1 from Chapter 4).

Given the primary importance of the linear advection of climatological-mean 925 hPa temperature by the composite 925 hPa wind anomaly field, it is of direct scientific interest to assess which atmospheric dynamical features are responsible for inducing the

925 hPa wind anomaly field using composite PV analyses and piecewise PV inversions. The composite PV anomaly analyses indicated distinct and potentially important PV anomaly features. Specifically, there are coherent PV anomaly features located in both the upper and lower atmosphere for each ETR category, with the upper level PV signatures more prominent (stronger and larger) than the ones at the surface.

Piecewise PV inversion analyses were then used to assess which of these regions of PV are most important in inducing the composite surface wind anomalies associated with ETR onset. In the both CAO cases, the LTPV provides the greatest contribution to the northerly 925 hPa winds over the eastern US. In Case 1, the LTPV feature is tied to the transient surface high pressure system as well as the cold surface potential temperature anomaly associated with the cold air outbreak, itself. In addition, CAOs of this category appear to extend eastward in association with the anti-cyclonic circulation induced by the surface potential temperature anomaly. Although the LTPV is also implicated as the primary contributor to the 925 hPa wind anomaly field in Case 2, the PV inversion results suggest the NAO likely affects this category of CAO events. First, the negative UTPV anomaly associated with the NAO induces an anticyclonic circulation anomaly that extends down to the surface. Eventually, the resulting near-surface temperature advection leads to the creation of a local warm surface air temperature anomaly which in turn induces low pressure and a cyclonic circulation anomaly in the lower troposphere, helping to enhance the initial near-surface temperature advection. Additional horizontal partitioning of the PV field indicate that the NAO provides a direct partial contribution to US CAO events. In contrast, for WW events, each of the three layers of the troposphere contributes substantially to the 925 hPa wind field. In Case 3,

however, it isn't immediately clear what the primary mechanism is for this category of events. However, in Case 4, the PV inversion results indicate that the PNA affects this category of WW events. The upper-level PNA pattern helps induce a near-surface temperature advection pattern that creates a warm anomaly. Then, upon creation of the warm anomaly as a result of the aforementioned warm advection, the warm anomaly creates its own counterclockwise circulation in the lower troposphere that then leads to warm advection further to the east in the US. Thus, in this case, the warm anomaly is initiated *due to a direct contribution from the PNA teleconnection pattern* with a subsequent self-progression of the warm anomaly to the east. Collectively, the piecewise PV inversions indicate a direct, but contributive role of low frequency modes in ETR events. The proposed pathway through which this occurs is summarized as follows: First, an upper tropospheric PV feature imparts a near-surface circulation that leads to temperature advection. Eventually, this temperature advection induces a near-surface temperature anomaly and a corresponding circulation that further enhances the initial temperature advection and leads to the ETR event. This pathway is summarized in Figure 5.18. Finally, one of the overarching conclusions is that the piecewise PV inversion analyses indicate (in nearly every case) that the SAT anomalies can act as effective PV anomalies and at least partially contribute to the near-surface wind anomalies, and often the resulting circulations lead to a subsequent eastward self-progression of the ETR events.

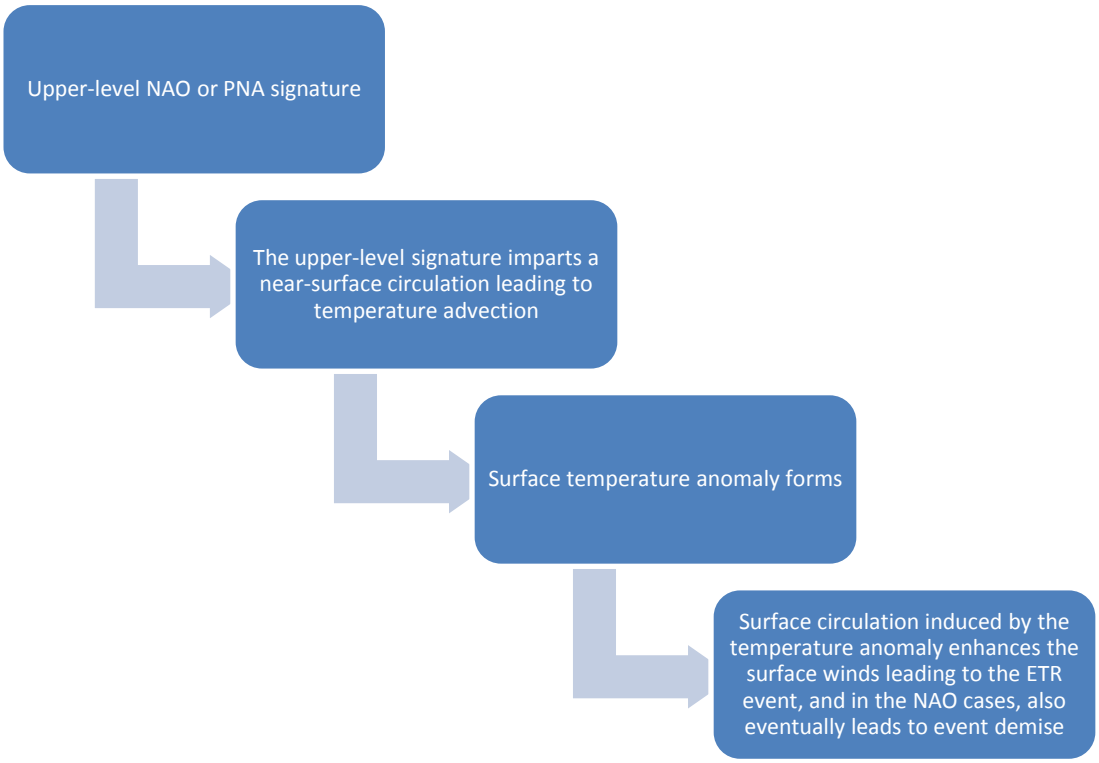

Figure 5.18: The proposed pathway through which low frequency modes modulate ETRs.

CHAPTER 6

CONCLUSIONS AND IMPLICATIONS

This dissertation aimed to improve the understanding of the trends and variability in ETRs, their physical connections to low frequency modes, and the dynamical mechanisms leading to ETR onset. Many of the earlier studies on ETR trends and variability did not consider the last decade, which is widely known to be a period of rapid warming on a global-scale. Further, there was relatively little known about the physical nature of ETR events, including how they are modulated by low frequency modes and the dynamical mechanisms that are responsible for ETR development. These unknowns provided the motivation for this dissertation and are of particular importance for WWs, as these events have rarely been studied.

The three original objectives presented in Section 1.6 were met through a series of statistical, synoptic and diagnostic dynamical analyses using reanalysis data. This dissertation provides new, important information on the updated trends in ETRs and their variability and presents a more complete understanding of the mechanisms leading to ETR onset. In addition, it also led to the discovery of the physical process through which low frequency modes modulate ETR events.

The study began by providing an updated baseline quantification of long-term ETR statistics (Chapter 3). This was pursued by applying a range of statistical analyses to observational reanalysis data, including trend, correlation and multiple linear regression analyses. Even with the inclusion of the last decade, analyses of long-term ETR variability reveal that there have not been any statistically significant trends in either

WWs or CAOs over most of the continental United States from 1949 to 2011 (Figure 3.4). Even so, strong interannual variability in ETRs is evident and can be linked to several prominent low-frequency modes. More specifically, a correlation analysis shows that regional ETR behavior is modulated by certain low-frequency modes with important regional asymmetries between the low frequency mode modulation of CAOs and WWs (Figure 3.6). For instance, the low-frequency modulation of WWs over the eastern United States is considerably more robust than the parallel modulation of CAOs given that four (one) low frequency modes are implicated in WW (CAO) events. Further, the influence of ENSO upon ETRs is found to be mainly limited to a modest modulation of WWs over the southern United States, which is a particularly interesting result since it counters prior studies of seasonal-mean temperature. Finally, the multiple linear regression analyses demonstrate that the collective influence of low-frequency modes can account for as much as 50% of the regional interannual variability in ETR behavior (Figure 3.7).

However, this analysis is statistical in nature, and therefore cannot establish the physical nature or mechanisms connecting ETRs to low frequency modes. Because the frequency and amplitude of ETRs in the United States has not changed, even with increasing background temperatures in the source regions, it is important to identify and understand the mechanisms responsible for such events in order to improve forecasts. These topics are pursued in the next two chapters (Chapters 4 and 5).

To establish the physical nature of ETRs, a synoptic-dynamic characterization of ETRs over the Southeast US from 1949-2011 is performed in Chapter 4 using composite time-evolution analyses of several different field variables. Discrete ETR events are first identified using magnitude, separation and duration criteria. Then they are categorized by

the sign and amplitude of relevant low-frequency modes into four categories (two each for CAOs and WWs) to help delineate the role of low frequency modes. The composite analyses reveal significant roles for both synoptic and large-scale disturbances in ETR development. Each category of events involves transient synoptic features, a low frequency mode influence or a juxtaposition of the two. Because extratropical cyclones are frequent in the midlatitudes during the winter season (Marciano et al. 2015), it should be no surprise that each of the four categories of ETR events involves a transient synoptic feature. Synoptically, these results generally confirm aspects of prior CAO studies (e.g. Konrad 1996, Konrad 1998, Konrad and Colucci 1989, Colle and Mass 1995) while providing distinctly new results on the behavior of WW development and establishing the synoptic role of low frequency modes in both CAO and WW onset. Further, these results provide a qualitative indication of the role of low frequency modes in ETR onset via their impact on regional circulation and temperature advection. Ultimately, it was found that synoptic-scale disturbances serve as dynamic triggers for ETR events, while the low-frequency modes provide a favorable environment for ETR onset. In addition, low frequency modes can also modulate the event duration (Case 2).

The accompanying composite PV anomaly analyses provide additional information regarding the dynamical features associated with ETR onset. The composite PV anomaly structure is generally characterized by prominent PV anomaly patterns in the mid to upper troposphere that are consistent with the coincident geopotential height anomaly patterns, with weaker anomalies in the lower atmosphere nearest the surface. These upper tropospheric PV anomaly patterns have horizontal structures that would be associated with southerly (northerly) winds over the central and eastern US during WW

(CAO) onset. In some cases, these induced flow patterns are supplemented with contributions from upstream PV anomaly features of opposite sign. This induction of near-surface winds by the upper-level PV anomaly patterns can be confirmed by calculating the Rossby penetration depth (Eq. 2.4), and is left for future work. It may be possible that the induced surface winds by the upper level PV anomaly are also modulated by changes in the near-surface boundary layer static stability once the ATR is developed.

Interestingly, the primary PV structures evolve similarly in the mode cases and neutral cases (for both WWs and CAOs), and is explained by similar responsible local circulation features for CAO and WW development. Comparatively, even though the PV anomaly amplitudes near the surface are smaller in magnitude and area than those in the upper troposphere, their closer proximity to the surface, where the key meridional air temperature transport occurs, gives them the potential to provide a fundamental contribution to ETR onset. In addition to the near-surface PV anomalies, these results indicate that a portion of the surface wind field likely arises from the SAT anomalies themselves acting as effective PV anomalies.

This set of analyses also provides some insight to the general behavior and development of CAOs and WWs. In particular, CAOs appear to be related to substantial air mass transport (normally from Canadian latitudes) while WW formation occurs more locally over the region of interest (with air mass emanating from the adjacent Gulf of Mexico or North Atlantic). Additionally, CAO cold air masses form in high latitudes and move southward at least 20° of latitude, while WW warm air masses form in more southerly latitudes but typically only traverse 5° latitude or less.

The last part of the dissertation (Chapter 5) explores a suite of diagnostic analyses to identify the primary thermodynamic processes and dynamical mechanisms responsible for ETR development over the Southeast US and to dynamically clarify the role of low frequency modes in ETR development. Diagnostic analyses, including heat budget and piecewise PV inversion analyses, are used extensively in this study and provide a strong foundation for identifying the primary mechanism(s) responsible for ETR development because they are based upon fundamental dynamical and thermodynamical principles.

Heat budget analyses indicate that linear temperature advection is the primary thermodynamic contributor to ETR development. The linear advection of the climatological-mean temperatures by composite wind anomalies plays the primary role, while the linear advection of the temperature anomalies by the climatological-mean winds plays a secondary role (especially over the east/northeast). In comparison to the total linear term, the nonlinear advection plays a smaller role (especially in the WW cases). Both the linear and nonlinear terms contribute positively to the temperature tendencies of interest, while the adiabatic and diabatic terms generally oppose the local temperature tendencies and effectively offset a portion of the advection contributions. However, one important caveat is that these heat budget analyses may be sensitive to the start and end points chosen for the composite partitions. For instance, it is possible that the diabatic term could be an important factor in establishing the cold air farther to north in earlier time steps. Further investigation on the sensitivity of the composite partitions is left for future work. In addition, the finding that the linear advection of the climatological-mean temperatures by the composite wind anomalies is principally responsible for ATRs could have important implications for climate change, specifically

changes associated with arctic amplification. Generally, arctic amplification leads to a reduced gradient in temperature. In principle, along with the assumption of unchanging anomalous winds, this could possibly lead to changes in the frequency and/or amplitude of ATRs. However, the specific impacts are difficult to identify because they will depend on how the changes are manifested at each latitude (i.e. how the gradient in temperature changes) in addition to possible changes in anomalous wind patterns and regional effects that may be associated with climate change.

In the present analysis, the two linear advection terms are also decomposed into their separate field components to clarify the physical nature of the two linear advection terms. The advection of the composite temperature anomalies by the climatological-mean winds is *weaker* in the composite for which low frequency modes are implicated, and can be accounted for by the relative magnitude of the composite temperature anomalies and associated temperature anomaly gradient. The linear decomposition analyses also indicate that the temperature gradients are typically weaker where low frequency modes are implicated, and hence lead to a weaker advection of the composite temperature anomalies by the climatological-mean winds.

Given the primary importance of the linear advection of climatological-mean 925 hPa temperature by the composite 925 hPa wind anomaly field, it is of direct scientific interest to assess which atmospheric dynamical features are responsible for inducing the 925 hPa wind anomaly field using composite PV analyses and piecewise PV inversions. The composite PV anomaly analyses indicated distinct and potentially important PV anomaly features. Similar to the findings in the synoptic analyses of PV in Chapter 4, there are coherent PV anomaly features located in both the upper and lower atmosphere

for each ETR category, with the upper level PV signatures more prominent (stronger and larger) than the ones at the surface.

Piecewise PV inversion analyses were then used to assess which of these regions of PV are most important in inducing the composite surface wind anomalies associated with ETR onset. In both CAO cases, the LTPV provides the greatest contribution to the northerly 925 hPa winds over the eastern US. In Case 1, the LTPV feature is tied to the transient surface high pressure system as well as the cold surface potential temperature anomaly associated with the cold air outbreak, itself. However, in Case 2, the PV inversion results suggest that the NAO also likely affects this category of CAO events. Additional horizontal partitioning of the PV anomaly field indicates that the NAO provides a direct partial contribution to US CAO events. In contrast, for WW events, each of the three layers of the troposphere contributes substantially to the 925 hPa wind field. In Case 3, it isn't immediately clear if there is a primary mechanism for this category of events, since there appear to be simultaneous contributions from multiple lower-level PV features (including 925 and 850 mb PV anomalies and SAT anomalies). In contrast, in Case 4, the PV inversion results indicate a direct contribution of the PNA pattern in this category of WW events.

Ultimately, the piecewise PV inversions indicate a direct, but contributive role of low frequency modes in ETR events. The proposed pathway through which this occurs is summarized as follows: First, the initial near-surface temperature advection is linked to an upper-tropospheric PV feature. Eventually, this near-surface temperature advection induces a near-surface temperature anomaly and a corresponding circulation that further enhances the initial temperature advection and leads to the ETR event. An exploration of

the time evolution of the piecewise PV inversions is left for future work to help confirm the causality in this proposed pathway through which ATR events are modulated by low frequency modes. These results confirm the role of low frequency modes in ETR onset, and verify that low frequency modes aren't sufficient by themselves to initiate ETRs but act in concert with other transient synoptic features. Finally, the piecewise PV inversion analyses indicate (in nearly every case) that the SAT anomalies act as an effective PV anomaly feature that partially contributes to the near-surface wind anomalies. These resulting circulations also often lead to the observed subsequent eastward self-progression of the ETR events.

Extreme temperature regimes will remain of interest to weather forecasters and climate scientists because of their socioeconomic impacts. Based on the results presented in Chapter 3, particularly the lack of trends in historical ETR variability, ETRs occur just as frequently and intensely now as they have during the past 60 years. Therefore, accurate prediction and forecasting of these events remains desirable to reduce their negative impacts on society and the economy. For improvements in prediction, a more complete physical understanding of ETR events is required. The investigations on the physical nature of ETRs and their dynamical mechanisms included within this dissertation (Chapters 4 and 5) make strides in achieving such an understanding. A particularly useful insight provided by this research is the confirmation of the role of low frequency modes in ETR events and the discovery of the dynamical pathway through which this modulation takes place. In principle, such links to low frequency modes suggest some potential for longer-term probabilistic predictability of ETR events. However, more research is necessary to fully understand the mechanics of this link and serves as a topic

for future work. An additional topic of future work is to further explore the asymmetry in low frequency mode modulation of ETRs that was identified in Chapter 3. Nonetheless, the results presented herein have relevant applications to forecasting ETRs by providing valuable scientific insight and understanding. This more complete physical understanding of ETRs is essential for optimizing the representation of ETR events in both numerical weather forecast and global climate models and assessing the likely future variability of ETRs in association with climate change.

References

Ambaum, M. H., B. J. Hoskins, and D. B. Stephenson, 2001: Arctic Oscillation or North Atlantic Oscillation? *J. Climate*, **14**, 3495-3507.

Ashcroft, L. C., A. B. Pezza, and I. Simmonds, 2009: Cold Events over Southern Australia: Synoptic Climatology and Hemispheric Structure. *J. Climate*, **22,** 6679-6698.

Augspurger, C. K., 2013: Reconstructing patterns of temperature, phenology, and frost damage over 124 years: Spring damage risk is increasing. *Ecology*, **94,** 41-50.

Barnes, E. A., and D. L. Hartmann, 2010: Dynamical Feedbacks and the Persistence of the NAO. *J. Atmos. Sci.*, **67**, 851-865.

Belsley, D. A., E. Kuh, and R. E. Welsch, 1980: *Regression diagnostics: Identifying Influential Data and Sources of Collinearity*. John Wiley & Sons, 292 pp.

Black, R. X., and R. M. Dole, 1993: The Dynamics of Large-Scale Cyclogenesis over the North Pacific Ocean, *J. Atmos. Sci,*. ***50***, 421-442.

Black, R. X., 2002: Stratospheric Forcing of Surface Climate in the Arctic Oscillation. *Journal of Climate*, **15,** 268-277.

Black, R. X., and B. A. McDaniel, 2004: Diagnostic Case Studies of the Northern Annular Mode, *J.Clim.*, ***17***, 3990-4004.

Blackmon, M. L., Y.-H. Lee, and J. M. Wallace, 1984a: Horizontal Structure of 500 mb Height Fluctuations with Long, Intermediate and Short Time Scales. *J. Atmos. Sci.*, **41**, 961-979.

Blackmon, M. L., Y.-H. Lee, J. M. Wallace, and H.-H. Hsu, 1984b: Time Variation of 500 mb Height Fluctuations with Long, Intermediate and Short Time Scales as Deduced from Lag-Correlation Statistics. *J. Atmos. Sci.*, **41**, 981-991.

Bosart, L. F., G. J. Hakim, K. R. Tyle, M. A. Bedrick, W. E. Bracken, M. J. Dickinson, and D. M. Schultz, 1996: Large-Scale Antecedent Conditions Associated with the 12-14 March 1993 Cyclone ("Superstorm '93") over Eastern North America. *Mon. Wea. Rev.*, **124,** 1865-1891.

Bretherton, F. P., 1966: Critical layer instability in baroclinic flows. *Quarterly Journal of the Royal Meteorological Society*, **92**, 325 – 334.

Cai, W., and Coauthors, 2015: Increased frequency of extreme La Nina events under greenhouse warming. *Nature Climate Change*, **5,** 132-137.

Campbell, J. L., M. J. Mitchell, P. M. Groffman, L. M. Christenson, and J. P. Hardy, 2005: Winter in northeastern North America: a critical period for ecological processes. *Frontiers in Ecology and the Environment*, **3**, 314 – 322.

Cellitti, M. P., J. E. Walsh, R. M. Rauber, and D. H. Portis, 2006: Extreme cold air outbreaks over the United States, the polar vortex, and the large-scale circulation. *J. Geophys. Res.*, **111,** D02114, doi:10.1029/2005jd006273.

Chen, Y., and P. Zhai, 2014: Precursor Circulation Features for Persistent Extreme Precipitation in Central-Eastern China. *Wea. Forecasting*, **29,** 226-240.

Christidis, N., and P. A. Stott, 2014: Change in the Odds of Warm Years and Seasons Due to Anthropogenic Influence on the Climate. *J. Climate*, **27,** 2607-2621.

Cochrane, D., and G.H. Orcutt, 1949: Application of Least Squares Regression to Relationships Containing Auto-Correlated Error Terms. *J. Amer. Stat. Assoc.*, **44**, 32-61.

Cohen, J., J. Foster, M. Barlow, K. Saito, and J. Jones, 2010: Winter 2009–2010: A case study of an extreme Arctic Oscillation event. *Geophys. Res. Lett.*, **37**, 161-168.

Cohen, J. L., J. C. Furtado, M. A. Barlow, V. A. Alexeev, and J. E. Cherry, 2012a: Arctic warming, increasing snow cover and widespread boreal winter cooling. *Environ. Res. Lett.*, **7**, 8p.

Cohen, J. L., J. C. Furtado, M. Barlow, V. A. Alexeev, and J. E. Cherry, 2012b: Asymmetric seasonal temperature trends. *Geophys. Res. Lett.*, **39**, 7p.

Colle, B. A., and C. F. Mass, 1995: The Structure and Evolution of Cold Surges East of the Rocky Mountains. *Mon. Wea. Rev.*, **123,** 2577-2610.

Colucci, S. J., D. P. Baumhefner, and C. E. Konrad, 1999: Numerical Prediction of a Cold-Air Outbreak: A Case Study with Ensemble Forecasts. *Mon. Wea. Rev.*, **127,** 1538-1550.

Curry, J., 1987: The Contribution of Radiative Cooling to the Formation of Cold-Core Anticyclones. *Journal of the Atmospheric Sciences*, **44**, 2575-2592.

Dallavalle, J. P., and L. F. Bosart, 1975: A Synoptic Investigation of Anticyclogenesis Accompanying North American Polar Air Outbreaks. *Mon. Wea. Rev.*, **103,** 941-957.

Davis, C.A., and K.A. Emanuel, 1991: Potential Vorticity Diagnostics of Cyclogenesis. *Mon. Wea. Rev.*, **119**, 1929-1953.

Davis, C. A., 1992: Piecewise Potential Vorticity Inversion. *Journal of the Atmospheric Sciences,* **49,** 1397-1411.

Dee, D. P., and Coauthors, 2011: The ERA-Interim reanalysis: configuration and performance of the data assimilation system. *Quarterly Journal of the Royal Meteorological Society*, **137**, 553 – 597.

Deser, C., 2000: On the teleconnectivity of the Arctic Oscillation, *Geophys. Res. Lett.*, **27**, 779-782.

Dole, R. M., and R. X. Black, 1990: Life Cycles of Persistent Anomalies. Part II: The Development of Persistent Negative Height Anomalies over the North Pacific Ocean. *Monthly Weather Review,* **118,** 824-846.

Dole, R. M., 2008: Linking Weather and Climate, in *Synoptic-Dynamic Meteorology and Weather Analysis and Forecasting: A Tribute to Fred Sanders*, edited by L. F. Bosart, and Bluestein, Howard B., pp. 297-348, American Meteorological Society, Boston.

Downton, M. W., and K. A. Miller, 1993: The Freeze Risk to Florida Citrus. Part II: Temperature Variability and Circulation Patterns. *J. Climate*, **6,** 364-372.

Evans, K. J., and R. X. Black, 2003: Piecewise Tendency Diagnosis of Weather Regime Transitions. *J. Atmos. Sci*., **60**, 1941-1959.

Feldstein, S. B., 2002: Fundamental mechanisms of the growth and decay of the PNA teleconnection pattern. *Quart. J. Roy. Meteor. Soc*.,**128**, 775-796.

Feldstein, S. B., 2003: The dynamics of NAO teleconnection pattern growth and decay. *Quart. J. Roy. Meteor. Soc.*,**129**, 901-924.

Francis, J. A., and S. J. Vavrus, 2012: Evidence linking Arctic amplification to extreme weather in mid-latitudes. *Geophys. Res. Lett.*, **39,** L06801, doi:10.1029/2012gl051000.

Grotjahn, R., and G. Faure, 2008: Composite Predictor Maps of Extraordinary Weather Events in the Sacramento, California, Region. *Wea. Forecasting,* **23,** 313-335.

Gu, L., and Coauthors, 2008: The 2007 Eastern US Spring Freeze: Increased Cold Damage in a Warming World. *BioScience*, **58,** 253-262.

Guirguis, K., A. Gershunov, R. Schwartz, and S. Bennett, 2011: Recent warm and cold daily winter temperature extremes in the Northern Hemisphere. *Geophys. Res. Lett.*, ***38,*** 6p.

Hankes, I. E., and J. E. Walsh, 2011: Characteristics of extreme cold air masses over the North American sub-Arctic. *J. Geophys. Res.*, **116**, 11p.

Hartjenstein, G., and R. Bleck, 1991: Factors Affecting Cold-Air Outbreaks East of the Rocky Mountains. *Mon. Wea. Rev.*, **119,** 2280-2292.

Hoskins, B. J., I. N. James, and G. H. White, 1983: The Shape, Propagation and Mean-Flow Interaction of Large-Scale Weather Systems. *J. Atmos. Sci.*, **40**, 1595-1612.

Hoskins, B. J., M. E. McIntyre, and A. W. Robertson, 1985: On the use and significance of isentropic potential vorticity maps, *Quarterly Journal of the Royal Meteorological Society*, *111*(470), 877-946.

Holton, J.R., 2004: *An Introduction to Dynamic Meterology*. 4th ed. Elsevier Academic Press, 535 pp.

Hurrell, J. W., 1995: Decadal Trends in the North Atlantic Oscillation: Regional Temperatures and Precipitation. *Science*, **269**, 676-679.

Hurrell, J. W., Y. Kushnir, M. Visbeck, and G. Ottersen, 2003: An Overview of the North Atlantic Oscillation. *The North Atlantic Oscillation: Climatic Significance and Environmental Impact*, J. W. Hurrell, Y. Kushnir, G. Ottersen, and M. Visbeck, Eds. Geophysical Monograph Series, **134**, 1-35.

Kalnay, E., et al., 1996: The NCEP/NCAR 40-Year Reanalysis Project. *Bull. Amer. Meteor. Soc.*, **77,** 437-471.

Kharin, V.V., F.W. Zwiers, X. Zhang, and G.C. Hegerl, 2007: Changes in Temperature and Precipitation Extremes in the IPCC Ensemble of Global Coupled Model Simulations. *J. Climate*, **20**, 1419-1444.

Kodra, E., K. Steinhaeuser, and A. R. Ganguly, 2011: Persisting cold extremes under 21st-century warming scenarios. *Geophys. Res. Lett.*, **38,** L08705, doi:10.1029/2011GL047103.

Koldstad, E. W., T. Breiteig, and Scaife, A. A., 2010: The association between stratospheric weak polar vortex events and cold air outbreaks in the Northern Hemisphere. *Quarterly Journal of the Royal Meteorological Society,* **136**, 886 – 893.

Konrad, C. E., 1996: Relationships between the Intensity of Cold-Air Outbreaks and the Evolution of Synoptic and Planetary-Scale Features over North America. *Mon. Wea. Rev.*, **124,** 1067-1083.

Konrad, C. E., 1998: Persistent Planetary Scale Circulation Patterns and Their Relationship with Cold Air Outbreak Activity over the Eastern United States. *Intl. J. Climatol.*, **18,** 1209-1221.

Konrad, C. E., and S. J. Colucci, 1989: An Examination of Extreme Cold Air Outbreaks over Eastern North America. *Mon. Wea. Rev.*, **117,** 2687-2700.

Lim, Y.-K., and S. D. Schubert, 2011: The impact of ENSO and the Arctic Oscillation on winter temperature extremes in the southeast United States. *Geophys. Res. Lett.*, **38,** L15706, doi: 10.1029/2011gl048283.

Loikith, P. C., and A. J. Broccoli, 2012: Characteristics of Observed Atmospheric Circulation Patterns Associated with Temperature Extremes over North America. *J. Climate*, **25,** 7266-7281.

Loikith, P. C., and A. J. Broccoli, 2014: The Influence of Recurrent Modes of Climate Variability on the Occurrence of Winter and Summer Extreme Temperatures over North America. *J. Climate*, **27,** 1600-1618.

Lu, Q. Q., R. Lund, and L. Seymour, 2005: An Update of U.S. Temperature Trends. *J. Climate*, **18**, 4906-4914.

Makoto, K., T. Kajimoto, L. Koyama, G. Kudo, H. Shibata, Y. Yanai, and J. H. C. Cornelissen, 2014: Winter climate change in plant-soil systems: summary of recent findings and future perspectives. *Ecological Research*, **29**, 593-606.

Marciano, C. G., G. M. Lackmann, and W. A. Robinson, 2015: Changes in U.S. East Coast Cyclone Dynamics with Climate Change. *Journal of Climate*, **28,** 468-484.

Meehl, G. A., J. M. Arblaster, and G. Branstator, 2012: Mechanisms Contributing to the Warming Hole and the Consequent U.S. East–West Differential of Heat Extremes. *Journal of Climate*, **25,** 6394-6408.

Milrad, S. M., E. H. Atallah, and J. R. Gyakum, 2009: Synoptic-Scale Characteristics and Precursors of Cool-Season Precipitation Events at St. John's, Newfoundland, 1979–2005. *Wea. Forecasting*, **24,** 667-689.

Mori, A. S., S. Fujii, and H. Kurokawa, 2014: Ecological consequences through responses of plant and soil communitites to changing winter climate. *Ecological Research*, **29**, 547-559.

Pan, Z., R. W. Arritt, E. S. Takle, W. J. Gutowski Jr., C. J. Anderson, and M. Segal, 2004: Altered hydrologic feedback in a warming climate introduces a "warming hole". *Geophys. Res. Lett.*, **31**, 4p.

Papritz, L., S. Pfahl, H. Sodemann, and H. Wernli, 2015: A Climatology of Cold Air Outbreaks and Their Impact on Air–Sea Heat Fluxes in the High-Latitude South Pacific. *Journal of Climate,* **28,** 342-364.

Park, T.-W., J.-H. Jeong, C.-H. Ho, and S.-J. Kim 2008: Characteristics of atmospheric circulation associated with cold surge occurrences in East Asia: A case study during 2005/06 winter, *Advances in Atmospheric Sciences, 25*(5), 791-804.

Park, T.-W., C.-H. Ho, and S. Yang, 2011: Relationship between the Arctic Oscillation and cold surges over East Asia. *J. Climate*, **24,** 68-83.

Park, T.-W., C.-H. Ho, S.-J. Jeong, Y.-S. Choi, S. K. Park, and C.-K. Song, 2011: Different characteristics of cold day and cold surge frequency over East Asia in a global warming situation. *J. Geophys. Res.*, **116,** D12118, doi: 10.1029/2010jd015369.

Peterson, T. C., and Coauthors, 2013: Monitoring and Understanding Changes in Heat Waves, Cold Waves, Floods, and Droughts in the United States: State of Knowledge. *Bulletin of the American Meteorological Society,* **94,** 821-834.

Peterson, A. G., and J. T. Abatzoglou, 2014: Observed changes in false springs over the contiguous United States. *Geophys. Res. Lett.*, **41,** 2156-2162, doi:10.1002/2014gl059266.

Portis, D. H., M. P. Cellitti, W. L. Chapman, and J. E. Walsh, 2006: Low-Frequency Variability and Evolution of North American Cold Air Outbreaks. *Mon. Wea. Rev.*, **134,** 579-597.

Portmann, R. W., S. Solomon, and G. C. Hegerl, 2009: Spatial and seasonal patterns in climate change, temperatures, and precipitation across the United States. *Proc. Natl. Acad. Sci. U.S.A.*, **106**, 7324-7329.

Rogers, J. C., and R. V. Rohli, 1991: Florida Citrus Freezes and Polar Anticyclones in the Great Plains. *J. Climate*, **4,** 1103-1113.

Ruff, T. W., and J. D. Neelin, 2012: Long tails in regional surface temperature probability distributions with implications for extremes under global warming, *Geophysical Research Letters*, *39*(4), 6.

Scaife, A. A., and Coauthors, 2014: Skillful long-range prediction of European and North American winters. *Geophys. Res. Lett.*, **41,** 2514-2519, doi: 10.1002/2014gl059637.

Scherer, M., and N. S. Diffenbaugh, 2014: Transient twenty-first century changes in daily-scale temperature extremes in the United States. *Climate Dyn.*, **42,** 1383-1404.

Schubert, S., H. Wang, and M. Suarez, 2011: Warm Season Subseasonal Variability and Climate Extremes in the Northern Hemisphere: The Role of Stationary Rossby Waves. *Journal of Climate*, **24**, 4773 – 4792.

Schultz, D. M., W. E. Bracken, L. F. Bosart, G. J. Hakim, M. A. Bedrick, M. J. Dickinson, and K. R. Tyle, 1997: The 1993 Superstorm Cold Surge: Frontal Structure, Gap Flow, and Tropical Impact. *Mon. Wea. Rev.*, **125,** 5-39.

Schultz, D. M., W. E. Bracken, and L. F. Bosart, 1998: Planetary- and Synoptic-Scale Signatures Associated with Central American Cold Surges. *Mon. Wea. Rev.*, **126,** 5-27.

Sisson, P. A., J. R. Gyakum, 2004: Synoptic-Scale Precursors to Significant Cold-Season Precipitation Events in Burlington, Vermont. *Wea. Forecasting*, **19,** 841-854.

Tan, Y.-C., and J. A. Curry, 1993: A Diagnostic Study of the Evolution of an Intense North American Anticyclone during Winter 1989. *Monthly Weather Review*, **121**, 961 – 975.

Tanaka, H. L., and M. F. Milkovich, 1990: A Heat Budget Analysis of the Polar Troposphere in and around Alaska during the Abnormal Winter of 1988/89. *Monthly Weather Review*, **118,** 1628-1639.

Teng, H., G. Branstator, H. Wang, G. A. Meehl, and W. A. Washington, 2013: Probability of US Heat Waves Affected by a Subseasonal Planetary Wave Pattern. *Nat. Geosci*., **6,** 1056-1061.

Thompson, D. W., and J. M. Wallace, 2001: Regional climate impacts of the Northern Hemisphere annular mode. *Science*, **293**, 85-89.

Turner, J. K., and J. R. Gyakum, 2011: The Development of Arctic Air Masses in Northwest Canada and Their Behavior in a Warming Climate, *Journal of Climate*, *24*(17), 4618-4633.

Uppala, S. M., and Coauthors, 2005: The ERA-40 re-analysis. *Quarterly Journal of the Royal Meteorological Society*, **131**, 2961 – 3012.

Vavrus, S., J. E. Walsh, W. L. Chapman, and D. Portis, 2006: The behavior of extreme cold air outbreaks under greenhouse warming. *Intl. J. Climatol.*, **26,** 1133-1147.

Wallace, J. M., and D. S. Gutzler, 1981: Teleconnections in the Geopotential Height Field during the Northern Hemisphere Winter. *Monthly Weather Review*, **109**, 784-812.

Wallace, J. M., 2000: North Atlantic Oscillation/annular mode: Two paradigms – one phenomenon. *Quar. J. Meteorol. Soc.*, **126**, 791 – 805.

Walsh, J. E., A. S. Phillips, D. H. Portis, and W. L. Chapman, 2001: Extreme Cold Outbreaks in the United States and Europe, 1948-99. *J. Climate*, **14,** 2642-2658.

Walther, G.-R., E. Post, P. Convey, A. Menzel, C. Parmesan, T. J. C. Beebee, J.-M. Fromentin, O. Hoegh-Guldberg, and F. Bairlein, 2002: Ecological responses to recent climate change. *Nature*, **416**, 389 – 395.

Wang, H., S. Schubert, M. Suarez, J. Chen, M. Hoerling, A. Kumar, and P. Pegion, 2009: Attribution of the Seasonality and Regionality in Climate Trends over the United States during 1950–2000. *J. Climate*, **22**, 2571-2590.

Wang, C., H. Liu, and S.-K. Lee, 2010: The record-breaking cold temperatures during the winter of 2009/2010 in the Northern Hemisphere. *Atmos. Sci. Lett.*, **11**, 161-168.

Westby, R. M., Y.-Y. Lee, and R. X. Black, 2013: Anomalous Temperature Regimes during the Cool Season: Long-Term Trends, Low-Frequency Mode Modulation, and Representation in CMIP5 Simulations. *J. Climate*, **26,** 9061-9076.

Westby, R. M. and R. X. Black, 2015: Development of Anomalous Temperature Regimes over the Southeastern United States: Synoptic Behavior and Role of Low-Frequency Modes. *Weather and Forecasting* (in press).

Wilks, D.S., 2011: *Statistical Methods in the Atmospheric Sciences*. Third ed. Academic Press, 676 pp.

Wu, A., W. W. Hsieh, and A. Shabbar, 2005: The Nonlinear Patterns of North American Winter Temperature and Precipitation Associated with ENSO. *Journal of Climate*, *18*, 1736-1752.

Wu, A., W. W. Hsieh, A. Shabbar, G. J. Boer, and F. W. Zwiers, 2006: The nonlinear association between the Arctic Oscillation and North American winter climate. *Climate Dynamics*, *26*(7-8), 865-879.

Yu, Y., M. Cai, R. Ren, and H. M. van den Dool, 2015: Relationship between Warm Airmass Transport into the Upper Polar Atmosphere and Cold Air Outbreaks in Winter. *Journal of the Atmospheric Sciences*, **72,** 349-368.

Zishka, K. M. and P. J. Smith, 1980: The Climatology of Cyclones and Anticyclones over North America and Surrounding Ocean Environs for January and July, 1950 – 77. *Monthly Weather Review*, **108**, 387 – 401.